2009-12-10

Modeling Molecular Transport and Binding Interactions in Intervertebral Disc

Francesco Travascio
University of Miami, f.travascio@umiami.edu

Recommended Citation

Travascio, Francesco, "Modeling Molecular Transport and Binding Interactions in Intervertebral Disc" (2009). *Open Access Dissertations*. 322.
https://scholarlyrepository.miami.edu/oa_dissertations/322

UNIVERSITY OF MIAMI

MODELING MOLECULAR TRANSPORT AND BINDING INTERACTIONS IN INTERVERTEBRAL DISC

By

Francesco Travascio

A DISSERTATION

Submitted to the Faculty
of the University of Miami
in partial fulfillment of the requirements for
the degree of Doctor of Philosophy

Coral Gables, Florida

December 2009

UNIVERSITY OF MIAMI

A dissertation submitted in partial fulfillment of
the requirements for the degree of
Doctor of Philosophy

MODELING MOLECULAR TRANSPORT AND BINDING INTERACTIONS IN INTERVERTEBRAL DISC

Francesco Travascio

Approved:

Weiyong Gu, Ph.D. Associate Professor of Biomedical Engineering	Terri A. Scandura, Ph.D. Dean of the Graduate School
Chun Yuh Huang, Ph.D. Assistant Professor of Biomedical Engineering	Weizhao Zhao, Ph.D. Associate Professor of Biomedical Engineering
Peter Tarjan, Ph.D. Professor Emeritus of Biomedical Engineering	Zhongmin Lu, Ph.D. Associate Professor of Biology

TRAVASCIO, FRANCESCO (Ph.D., Biomedical Engineering)
(December 2009)

Modeling Molecular Transport
and Binding Interactions in
Intervertebral Disc

Abstract of a dissertation at the University of Miami.

Dissertation supervised by Professor Wei Yong Gu.
No. of pages in text. (184)

Low back pain represents a significant concern in the United States, with 70% of individuals experiencing symptoms at some point in their lifetime. Although the specific cause of low back pain remains unclear, symptoms have been strongly associated with degeneration of the intervertebral disc. Insufficient nutritional supply to the disc is believed to be a major mechanism for tissue degeneration. Understanding nutrients' transport in intervertebral disc is crucial to elucidate the mechanisms of disc degeneration, and to develop strategies for tissue repair (*in vivo*), and tissue engineering (*in vitro*).

Transport in intervertebral disc is complex and involves a series of electromechanical, chemical and biological coupled events. Despite of the large amount of studies performed in the past, transport phenomena in the disc are still poorly understood. This is partly due to the limited number of available experimental techniques for investigating transport properties, and the paucity of theoretical or numerical methods for systematically predicting the mechanisms of solute transport in intervertebral disc.

In this dissertation, a theoretical and experimental approach was taken in order to investigate the mechanisms of solute transport and binding interactions in intervertebral disc.

New imaging techniques were developed for the experimental determination of diffusive and binding parameters in biological tissues. The techniques are based on the principle of fluorescence recovery after photobleaching, and allow the determination of the anisotropic diffusion tensor, and the rates of binding and unbinding of a solute to the extracellular matrix of a biological tissue. When applied to the characterization of transport properties of intervertebral disc, these methods allowed the establishment of a relationship between solute anisotropic and inhomogeneous diffusivity and the unique morphology of human lumbar annulus fibrosus.

A mixture theory for charged hydrated soft tissues was presented as a framework for theoretical investigations on solute transport and binding interactions in cartilaginous tissues. Based on this theoretical framework and on experimental observations, a finite element model was developed to predict solute diffusive-convective-reactive transport in cartilaginous tissues. The numerical model was applied to simulate the effect of mechanical loading on solute transport and binding interactions in cartilage explants and intervertebral disc.

ACKNOWLEDGMENTS

This research project would not have been possible without the support of many people. My heartfelt gratitude goes to all those people who, throughout the last four years, have helped and supported me in many ways.

I am deeply grateful to my supervisor, Dr. Weiyong Gu, for his guidance during my dissertation. His patience, wisdom, insightful comments, and constant encouragement made me improve not only as a researcher but also as a person.

I would like to thank Drs. Chun Yuh Huang, Weizhao Zhao, Zhongmin Lu, and Peter Tarjan for kindly serving on my dissertation committee.

Special thanks also to all the members of the Tissue Biomechanics Laboratory for their help, the encouragement given, and their friendship.

I wish to express my love and gratitude to my family and my wife Pamela, who constantly supported me, and always approved my decisions.

Funding for this research project was provided by NIH/NIAMS (AR050609).

TABLE OF CONTENTS

Page

CHAPTER 4: RELATIONSHIP AMONG SOLUTE TRANSPORT PROPERTIES, STRUCTURE AND COMPOSITION OF IVD

CHAPTER 5: DEVELOPMENT OF NEW TECHNIQUE FOR THE SIMULTANEOUS DETERMINATION OF SOLUTE DIFFUSIVITY AND BINDING INTERACTIONS WITH ECM OF BIOLOGICAL TISSUES

CHAPTER 6: FINITE ELEMENT ANALYSIS OF SOLUTE TRANSPORT IN CARTILAGINOUS TISSUES: EFFECT OF MECHANICAL LOADING ON DIFFUSION, CONVECTION, AND BINDING REACTIONS

CHAPTER 7: GENERAL CONCLUSIONS AND RECOMMENDATIONS

LIST OF TABLES

LIST OF FIGURES

Chapter 1: GENERAL INTRODUCTION

1.1 Aims of the study

Low back pain is a major socioeconomic concern in this country, affecting 15%-45% of the population.[151] This disease has been associated with disc degeneration.[25;48;107;211] Although several studies have been performed to elucidate the etiology of disc degeneration, its mechanisms have not been fully delineated. It is believed that poor nutritional supply has implications on disc degeneration.[13;25;48;75;148;198;203]. Therefore, in the past years, the pathways and the mechanisms of nutrient transport in the disc have been the object of intense investigation.[203]

The intervertebral disc is the largest avascular structure in the human body, receiving nourishment from the vascular network surrounding the tissue. Transport of solutes within the disc is complex, involving a series of mechanical, electrical, chemical and biological coupled events. Numerous studies focused on the characterization of transport properties of the disc, such as solutes' diffusivities and hydraulic permeability.[94] However, there is still a lack of knowledge on the relationship between transport properties and the morphology and composition of the intervertebral disc. Nevertheless, transport of some molecules (e.g., growth factors, extracellular matrix components, etc.) can involve binding interactions with the extracellular matrix of cartilaginous tissues.[3;12;55;93;163] Currently, it is still not clear how binding interactions between solutes and extracellular matrix affect transport in cartilaginous tissues. Besides, no experimental study has ever been performed to determine the physical parameters that govern binding interactions in intervertebral disc. This is partly due to the fact that, to date, the number of available experimental techniques for investigating binding phenomena is limited.

The broad objective of this thesis is to investigate molecular transport within the intervertebral disc in the presence of binding interactions. In order to achieve this goal, a theoretical and experimental approach is taken. The specific aims of this thesis are:

Specific Aim #1: Development of new imaging techniques for measuring diffusivities and binding reaction rates in biological tissues. Experimental techniques able to investigate diffusivity and binding in biological tissues are limited. In this study, new imaging techniques, based on fluorescence recovery after photobleaching (FRAP), will be developed in order to determine solute anisotropic diffusivity and binding reaction rates in biological tissues. The techniques will be applied to the characterization of the transport properties of the intervertebral disc.

Specific Aim #2: Investigation of the relationship between transport properties and morphology of intervertebral disc. It is hypothesized that the unique morphology of the intervertebral disc is responsible for anisotropic and inhomogeneous solute diffusivity in the tissue. To test these hypotheses, FRAP tests will be conducted to characterize the solute anisotropic diffusion tensor in the tissue. In addition, Scanning Electron Microscopy (SEM) imaging will be performed to investigate tissue morphology. Solute diffusivity will be related to the unique structural arrangement of collagen fibers of the disc.

Specific Aim #3: Development of a new numerical model for predicting solute binding and transport in intervertebral disc. Guided by the experimental results produced in the previous studies (Specific Aims #1 and #2), a new finite element model will be developed. This model will be able to describe the mechano-electrochemical behavior of the intervertebral disc, the convective-diffusive transport of solutes, and the kinetics of solute binding with the extracellular matrix of the tissue. The new model will provide a more realistic description of the transport phenomena occurring in the intervertebral disc.

1.2 Background and significance

The unique morphology and composition of intervertebral disc is such that solute transport is inhomogeneous, anisotropic, and, in some cases, affected by binding reactions with the structure of the disc. In this section, an overview of the structure, the composition, and the transport properties of the intervertebral disc will be provided. Also, a brief description of the principles and applications of FRAP will be introduced. Additionally, a review of current advances in theoretical modeling of the mechano-electrochemical behavior of soft hydrated tissues will be provided. Finally, the significance and the clinical relevance of this study will be assessed.

1.2.1 Structure and composition of IVD

Intervertebral disc (IVD) is a complex and heterogeneous structure constituted by the nucleus pulposus (NP) in the center, surrounded by the annulus fibrosus (AF). In non-pathologic discs, NP and the inner part of AF are superiorly and inferiorly covered by cartilage end-plate (CEP), a layer of hyaline cartilage that interfaces IVD and the vertebral body.[206] Nucleus pulposus is composed by a randomly oriented network of collagen fibers embedding highly hydrated proteoglycans.[92] In contrast, AF is composed by 15-25 concentric layers of collagen fibers termed lamellae.[73;130] Within each lamella, bundles of collagen fibers are inclined, with respect to the axial direction of the spine, with angles varying from ±62 to ±45 degrees,[30] see Figure 1.1. Recent investigations on animal disc morphology indicated the presence of cavities extending in the direction of the collagen fibers within the lamella. This unique arrangement of collagen fibers was formerly observed in murine coccygeal AF, and named ‘micortubules’.[90] The presence of such a microstructure was also confirmed by the observation of the morphology of bovine coccygeal AF, and termed ‘microtubes’,[96;192] see Figure 1.2. To date, the specific physiological function of microtubes is unknown. However, it has been speculated that microtubes can have implications on solute anisotropic and inhomogeneous transport through the AF of the disc.[96;192]

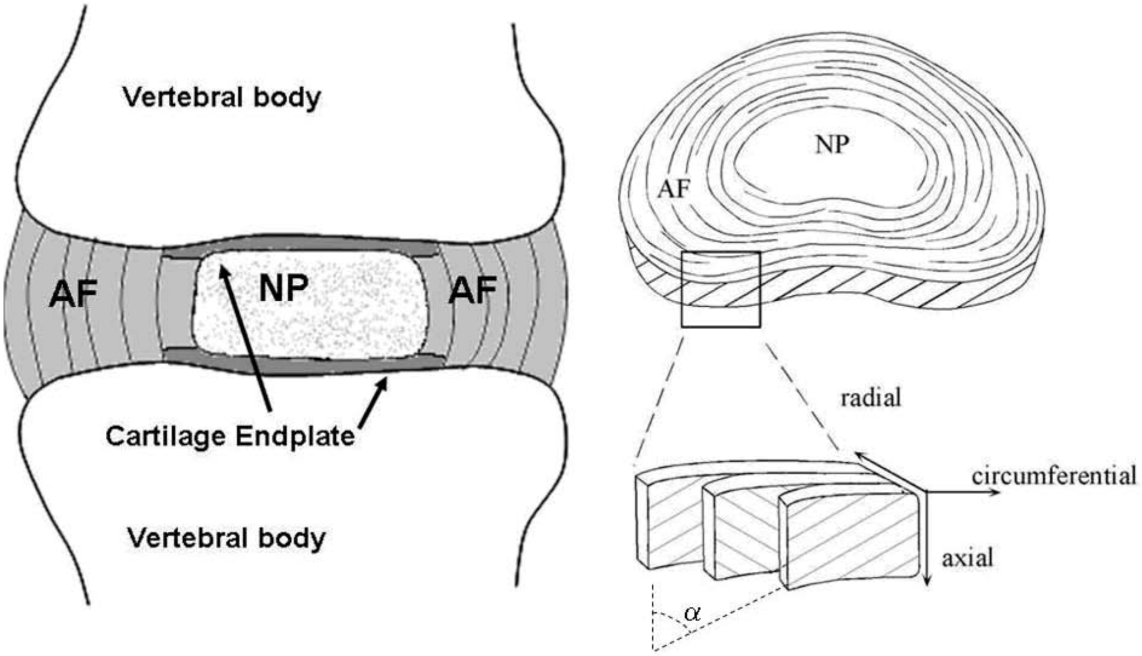

Figure 1.1 Structure of IVD. The nucleus pulposus (NP), the annulus fibrosus (AF), the cartilage end-plates, and the orientation of collagen fibers (α) are shown.[212]

The composition of the IVD is characterized by a poor cellular density, increasing from the NP to the outer AF.[70] It is generally believed that cell population in IVD comprises two major phenotypes: fibrocyte-like cells and chondrocyte-like cells.[210] Fibrocyte-like cells are primary located in the outer region of the AF, while chondrocyte-like cells are found in the inner AF and in the NP[32;167]. An additional type of cells, located in the central portion of the disc, is of notochord origin.[51] However, in humans, the presence of notochords is dramatically reduced by adolescence, leaving a group of chondrocytic cells that may have migrated in from the CEP.[138;210] The disappearance of notochordal cells has been associated with the onset of disc degeneration.[2]

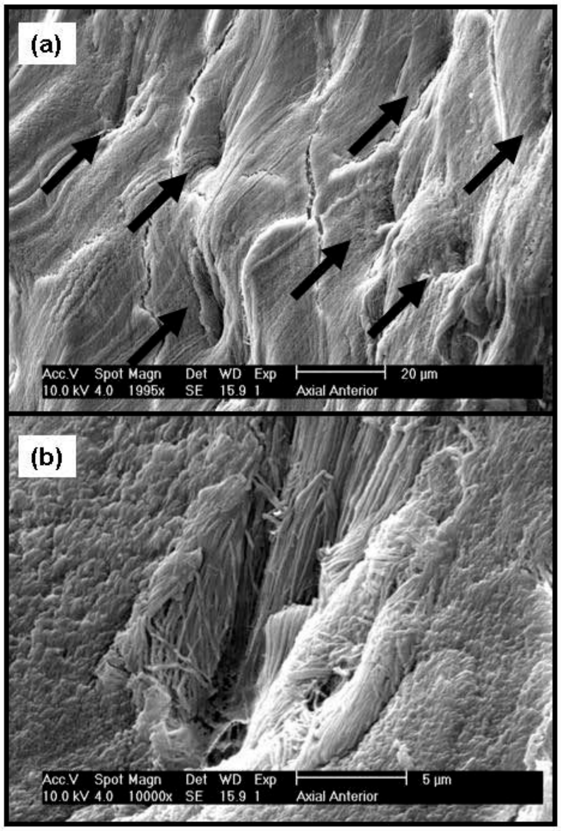

Figure 1.2. SEM image of axial section of bovine coccygeal AF. (a) Microtubes are shown by arrows. (b) Magnification of microtube present in figure (a).[192]

The major component of the disc structure is the extracellular matrix (ECM), constituted by a complex network of collagen embedded in a gel of interstitial fluid (i.e. water, ions, proteins, etc.) and proteoglycans,[48] see Figure 1.3. Collagen is more abundant in the outer AF (accounting for 70% of the dry weight of the tissue) than in the central part of the disc (constituting only 20% of the dry weight of NP).[48] In contrast, proteoglycans are more abundant in NP, where they comprise 50% of the dry weight of the tissue.[48] The IVD is predominantly composed by Type I and II collagen. However, small amounts of Type III, V, VI and IX collagen have also been found.[149] Type I collagen is most abundant in the outer AF, and its concentration decreases progressively from the periphery to the core of the disc. Type II collagen presents an opposite gradient of concentration within the disc, being more abundant in the NP and decreasing in the outer AF.[68] Proteoglycans are molecules constituted by a core protein to which a variable number of glycosaminoglycan units are covalently bonded, see Figure 1.4a. The monomeric units of proteoglycans can assemble on a central filament of hyaluronate to form large aggregates, see Figure 1.4b. In IVD, the most common glycosaminoglycans are chondroitin sulfate and keratane sulfate.[68] Both chondroitin sulfate and keratane sulfate present negatively charged carboxyl and sulfate groups. The negative charges of the glycosaminoglycans are considered as ‘fixed’ in the solid ECM of the tissue, since proteoglycans are entangled with the network of the collagen fibers of IVD. Studies on murine articular cartilage demonstrated the presence of binding interactions between glycosaminoglycans and positively charged solutes.[93] The electrostatic interaction between ‘fixed’ charges and ions in interstitial fluid also have implications on the electromechanical and transport properties of IVD, such as swelling behavior, streaming potential and current, electro-osmosis, fluid and solutes transport.[60;63;201;202] The unique structure and composition of IVD are such that the tissue can be schematized as an inhomogeneous, anisotropic, and multiphasic material. Therefore, the mixture theory represents a suitable theoretical framework to model the electromechanics and the transport phenomena in IVD.[85;174;175;218;219]

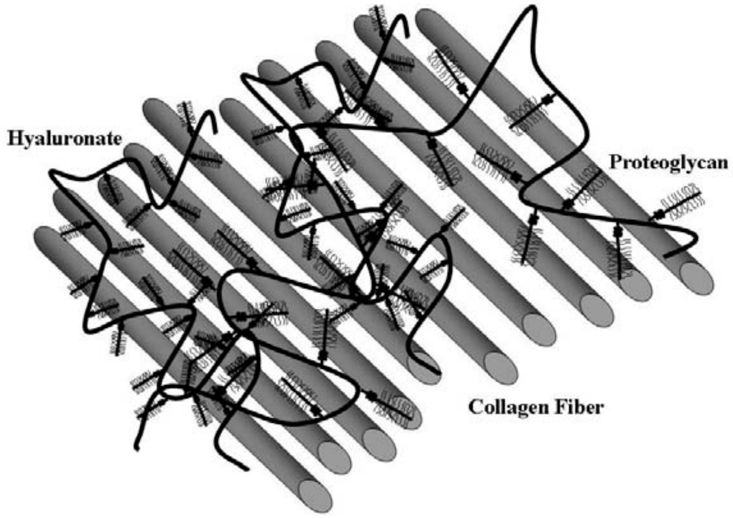

Figure 1.3. Schematic of the extracellular matrix of the disc. Long aggregates of proteoglycans are entangled within the collagen fibers.[142]

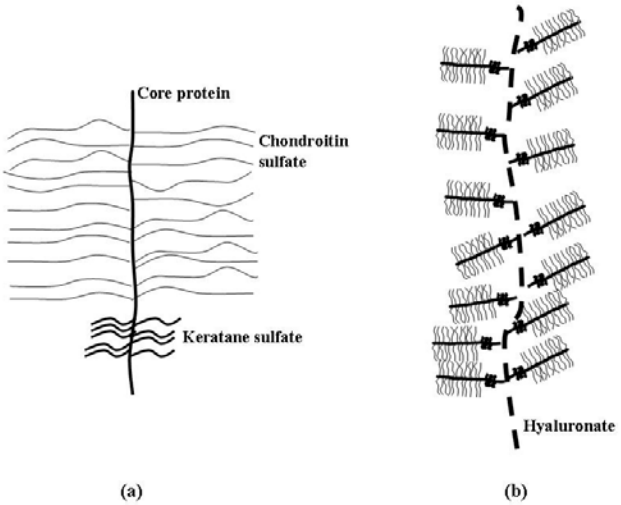

Figure 1.4. Structure of proteoglycans. (a) Monomeric unit. (b) Aggregate of proteoglycan units.[68]

1.2.2 Nutritional pathways in IVD

Poor nutritional supply is believed to be one of the major causes of disc degeneration.[13;25;48;75;80;148;198;203] Therefore, numerous studies investigated the mechanisms and the pathways of nutrition in the disc. The IVD is the largest avascular structure in the human body. Consequently, nourishment of disc cells is provided by the vascular network surrounding the disc. Previous studies indicated that nutrient delivery to the disc can occur through two possible pathways: axially from the CEPs separating the disc from the vertebrae, and radially from the vascular network surrounding AF,[24;74;80;133;148;153;168;205] see Figure1.5. Due to the avascular nature of the tissue, diffusion is the major transport mechanism for small solutes, such as most nutrients.[131;199;200] Therefore, in past years, a copious amount of studies have been conducted to determine diffusivities of solutes in both animal and human IVD (see Section 1.2.3).

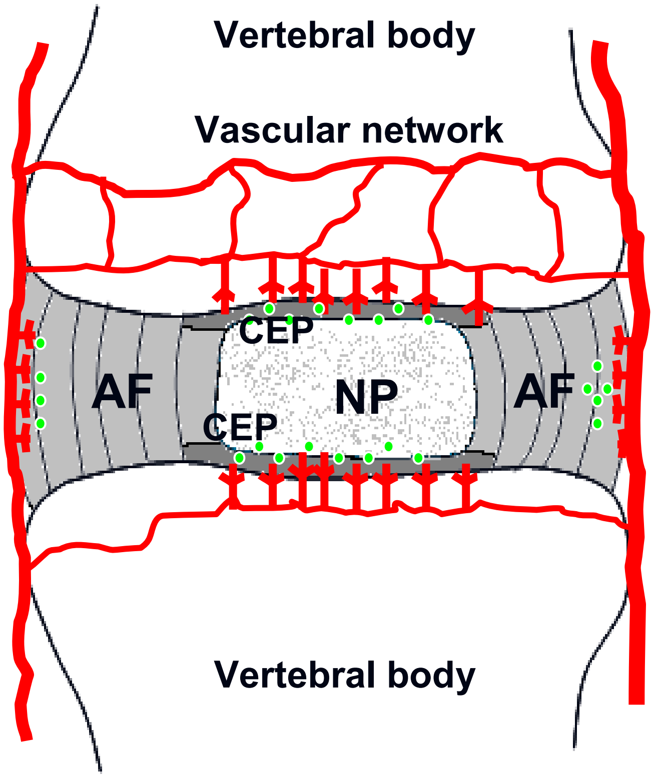

Figure 1.5 Schematic of nutritional supply pathways in IVD. Nutrient delivery is provided by the vascular network surrounding the disc. Nutrients can access the disc from the CEPs, or through the vascular network surrounding the AF.[134]

1.2.3 Transport properties of IVD

In soft hydrated tissues, the transport of water and solutes is regulated by transport properties such as hydraulic permeability, solute diffusivity, and convection coefficient.[61;217] In IVD, experimental and analytical studies suggested that the transport of small solutes (i.e. oxygen, glucose, lactate, etc.) is mainly due to diffusion.[74;104;131;199;200;203] In contrast, for large molecules, such as growth factors, proteases, and their inhibitors, which have a much lower diffusivity,[18] convection could significantly contribute to the movement of the solutes through the extracellular matrix.[203] Thus, in this case, solute transport is also regulated by the hydraulic permeability.[49;75;137;155;168;200;217]

A considerable amount of studies investigated has been conducted to investigate solute diffusivity in both animal and human IVDs.[1;7;17;33;43;74-78;84;95;96;133;152;153;168;173;186;192;199;200;204;205;207;221] In particular, experimental observations indicated that solute diffusion in IVD is anisotropic and heterogeneous.[33;84;95;96;155;192] A summary of experimental results for diffusivity in IVD from recent studies is reported in Table 1.1. The anisotropic solute diffusivity in IVD has been attributed to the unique structure of the ECM of the disc.[84;96;192] It has been suggested that microtubes present in AF have implications on the anisotropic solute diffusive transport through the disc.[96;192]

Several constitutive models for diffusivity in fibrous porous media have been developed, including models based on steric effects,[127;154] models based on hydrodynamic effects,[23;161] and models based on both steric and hydrodynamic effects.[19;97;98;158] However, these models are not able to satisfactorily describe solute diffusion in hydrogels or soft hydrated biological tissues.[135] Experimental studies showed that the major factors governing diffusivity in cartilaginous tissues are solute size and tissue porosity (or pore size),[27] which is related to the hydration and the structure of the tissue.[133] Gu et al. (2004) proposed an empirical constitutive model for diffusivity in porous fibrous media in which the diffusion coefficient of a solute was related to its hydrodynamic radius and to the hydraulic permeability of the porous medium. This model could satisfactorily predict diffusivities of large molecules in agarose gels and ion diffusivity in charged gels and cartilaginous tissues.[215]

Considerable research has been carried out in order to characterize the hydraulic permeability in human and animal IVD.[10;44;62;64;72;81;91;110;156;157;220] It was found that hydraulic permeability in IVD is anisotropic and depends upon the content of water and proteoglycans within the tissue.[62;72;91;156;220] Several theoretical models for hydraulic permeability of uncharged and charged fibrous porous media have been proposed.[45;69;113;144;170;183] In particular, Gu et al. (2003), proposed an empirical constitutive equation for hydraulic permeability in soft hydrated tissues and hydrogels. This model correlates the intrinsic hydraulic permeability to the water volume fraction of the medium, and, therefore, to its deformation (i.e., level of strain).[65]

In this thesis, solute transport in IVD is modeled using the empirical constitutive equations for hydraulic permeability and solute diffusivity proposed by Gu et al. (2003), and Gu et al. (2004), see Chapter 6.

Solute	Tissue	Method	D (x 10^{-10} m^2/s)	Ratio	Ref.
Na^+	Human lumbar IVD (T = 25°C)	Radiotracer	7.4	-	204
	Bovine coccyg. AF (T = 22°C)	Electrical conductivity	2.75 - 4.4	0.62†	95
Cl^-	Human lumbar IVD (T = 25°C)	Radiotracer	11.4	-	204
	Bovine coccyg. AF (T = 22°C)	Electrical conductivity	4.25 – 6.75	0.63†	95
Oxygen	Bovine lumbar AF (T = 22°C)	Steady-State Diffusion	14.3	-	221
	Porcine lumbar IVD (T = 22°C)	Electrochemical	25	-	152
Water	Porcine lumbar AF (T = 20°C)	MRI	10.6 – 13.6	0.75†	84
	Human lumbar AF (T ~ 0°C)	MRI	-	0.84†	33
	Ovine lumbar AF	MRI	10.3 - 11.4	0.9†	43
SO_4^-	Canine IVD	Radiotracer	2.78 - 3.89	-	199
Glucose	Bovine coccyg. AF (T = 22°C)	Steady-State Diffusion	0.917 - 1.38	0.66†	96
	Human lumbar AF (T = 37°C)	Radiotracer	2.5	-	133
Lactate	Human lumbar AF	Indirect measurement	4.86	-	173
	Bovine AF	Radiotracer	3.4	-	17
Fluorescein (332Da)	Bovine coccyg. AF (T = 22°C)	FRAP	0.814 – 1.26	0.64†	192
Dextran (70kDa)	Bovine AF	Radiotracer	0.14	-	17

Table 1.1 Summary of experimental results for diffusion coefficient, D, in IVD from recent studies. For studies investigating anisotropic diffusivity (†), the ratio of the smallest to the largest value of the diffusion coefficient is reported.[193]

1.2.4 Effect of binding reactions on molecular transport in cartilaginous tissues

Transport of some molecules (e.g., growth factors, proteins, cytokines, etc.) in cartilaginous tissues can involve binding reactions with the ECM of the tissue. It has been reported in the literature that several molecules bind to the ECM of articular cartilage.[3;12;55;93;163] The modalities of solute-matrix binding depend on the chemical nature of the solute. For instance, a study on solute transport in articular cartilage reported that rhodamine B base and tetramethylrhodamine (TMR), positively charged, bind to the negatively charged ECM.[3;163] Similarly, Inagawa et al. (2009) demonstrated that octaarginine (positively charged) specifically binds to the glycosaminoglycans of cartilage ECM.[93]. In addition, experimental studies on desorption and diffusion of growth factors in bovine articular cartilage showed that IGF specifically binds to IGF-binding proteins present in the ECM of the cartilage tissue.[12;55] Moreover, the effect of the binding interactions resulted in slower diffusive transport of IGF in cartilage.[55]

Knowledge of the kinetics of molecular binding is crucial to fully understand the mechanisms for molecular transport in tissues. Based on experimental data reported by Bhakta et al.[12] and Morales,[141] Zhang et al.[222] developed a numerical model to describe the effect of solute binding on solute transport in cartilage. The findings of this study highlighted the fundamental role played by the binding site and the rate of binding reaction in regulating solute transport in the tissue.

Currently, there are a limited number of techniques capable of experimentally investigating molecular binding in tissues. Bhakta et al. (2000) and Garcia et al. (2003) proposed an approach based on the use of radio isotope-labeled molecules to provide a quantitative estimation of the fraction of bounded solute in tissue.[12;55] However, this technique cannot provide a spatial distribution of the bounded molecules within the tissue. A fluorescence microscopy approach was used by Arkill and Winlove (2008) to detect binding of rhodamine B to cartilage.[3] This technique allows the visualization of the areas of the tissue in which binding occurs. However, this method does not provide quantitative information about the fraction of bound solute within the tissue. In 1999, Houtsmuller and co-workers developed a site-specific photobleaching method for the quantitative determination of the mobile and the immobile fractions of molecules in living cells at equilibrium.[82;83] Several other methods based on Fluorescence Recovery After Photobleaching (FRAP) and Fluorescence Correlation Spectroscopy (FCS) have also been proposed for the analysis of solute diffusion-reaction processes in cells.[22,26,28,29,35,42,46,102,108,120,185,197] To date, no studies have been performed on binding kinetics of solutes in IVD.

1.2.5 Fluorescence Recovery After Photobleaching (FRAP)

Fluorescence recovery after photobleaching (FRAP) is a technique that measures the mobility of fluorescently-labeled molecules in a medium. During a FRAP experiment, a region of the sample containing mobile fluorescent molecules is momentarily exposed to a high-intensity laser source, causing irreversible photochemical bleaching of the fluorescent dye in that region. After photobleaching, fluorescent molecules from unirradiated areas of the sample diffuse into the bleached spot. The solute mobility is determined by monitoring the rate of fluorescence recovery in the bleached area,[6] see Figure 1.6.

Depending on the chemical nature of the fluorescent probe, the recovery is determined by the solute diffusivity and by binding reactions with binding sites (e.g., receptors, binding proteins, electrically charged molecules, etc.) present in the medium.[125;184] Several approaches have been proposed to determine molecular diffusivity from fluorescence recovery data. All of them are based on the assumption that, within the sample, the fluorescence light intensity is proportional to the concentration of fluorescent solute.[6] For instance, Axelrod et al. (1976)

proposed a method in which the analytical solution of solute diffusion in a circle (the bleached spot) was used to curve-fit the rate of recovery of fluorescence intensity within the bleached area.[6] Following the same methodological approach, numerous variations and evolutions of this method have been proposed.[139;166] Several other methods are based on numerical approaches to analyze fluorescence recovery data. The advantage of using a numerical approach is that complicated cases of fluorescence recovery, for which no analytical solution is available, can be analyzed.[179] An alternative method for the analysis of fluorescence recovery data is based on the Fourier analysis of FRAP images.[8;9;162;178;192-195] With respect to the other methods, the advantage of using a Fourier transform approach is that the analysis is independent from the initial conditions of the bleached spot of the sample (see Chapter 3 and Chapter 5).

During the past decades, FRAP has been used extensively for characterizing molecular transport (i.e., diffusion and binding interactions) in living cells (see reviews by Meyvis et al.,[139] Reits and Neefjes,[166] Lippincott-Schwartz et al.,[125] Sprague and McNally,[184] etc.). Recently, fluorescence photobleaching techniques have also been applied for measuring isotropic and anisotropic molecular diffusivity in cartilaginous tissues and in tissue-engineered three-dimensional chondrocyte constructs.[39;116-119;192;194;194]. Compared to the traditional one-dimensional diffusion experiments, FRAP presents the advantages of higher spatial resolution (μm compared to mm),[194] shorter experimental time (few minutes compared to hours), and the ability to measure intact samples both *in vitro* and *in vivo*.[139] Therefore, in this study, FRAP is used to investigate the anisotropic diffusivity and the binding reaction of solutes in the extracellular matrix of the intervertebral disc (specific aims #1 and #2).

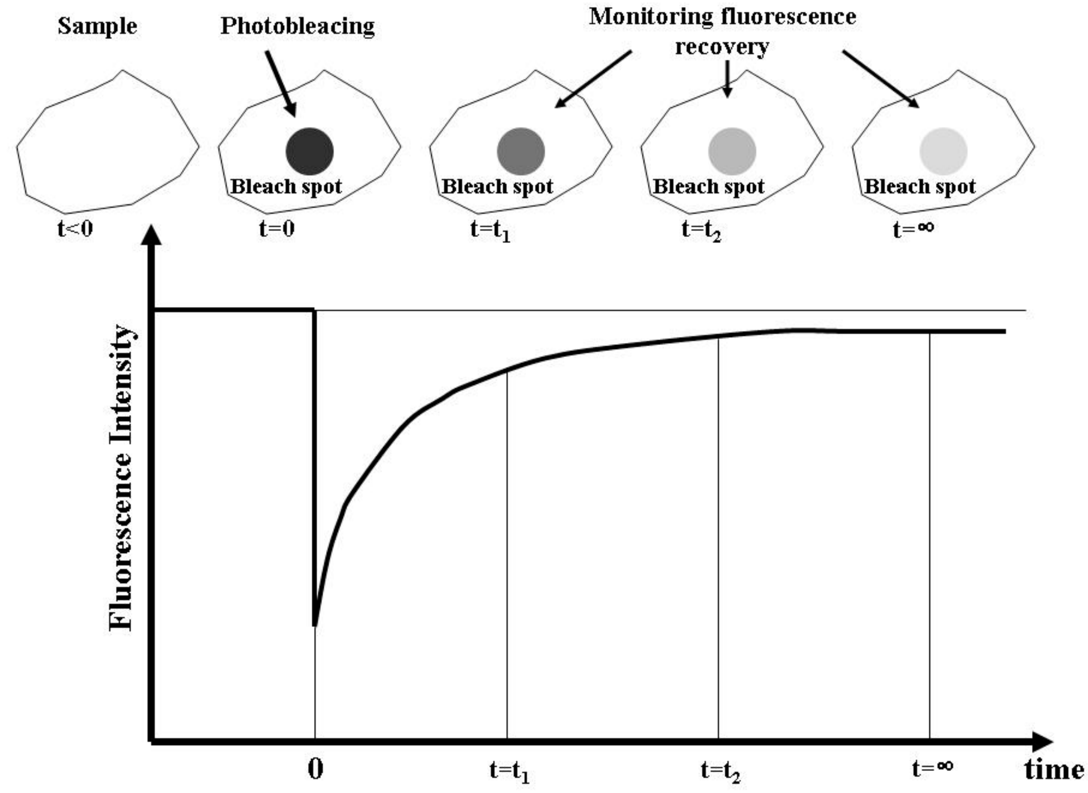

Figure 1.6. Schematic illustrating FRAP technique. After photobleaching (*t*=0), the mobility of the fluorescent solute is determined by monitoring the rate of recovery of the fluorescence intensity within the bleached spot.[184]

1.2.6 Modeling soft hydrated tissues mechanical behavior and transport phenomena

A considerable number of studies has been conducted on theoretical modeling of the transport properties and the mechanical behavior of porous media.[38] One of the most accredited theoretical frameworks was the biphasic theory, formerly introduced by Mow and co-workers to describe fluid transport and elastodynamics of articular cartilage.[144] According to the biphasic theory, the porous medium is modeled as a continuum, constituted by an elastic solid matrix embedded in a fluid phase. The mechanical properties of the whole system are averaged over the relative amounts (i.e., volumetric fraction) of the two constituents (i.e., solid and fluid phase) of the medium. During the past decades, the biphasic theory has been broadened in order to include viscoelastic and non-linear elastic behavior of the solid matrix.[79;129;145;176]

In 1991, Lai et al.[114] formulated a triphasic mechano-electrochemical theory for porous media, able to describe the mechanical behavior and transport phenomena of charged soft hydrated tissues. The triphasic theory models the tissue as a mixture of a charged solid matrix embedded in a solution of interstitial fluid and an electrolyte. This theoretical formulation is centered on the concept of the electrochemical potentials of the phases composing the mixture. According to the triphasic theory, the gradients of electrochemical potentials are the driving forces for the deformational behavior of the tissue and the solutes and fluid transport. A similar theoretical framework was also developed by Huyghe and Janssen.[88;89]

In 1998, Gu et al.[61] extended the triphasic model by proposing a more general mixture theory to account for the presence of multiple electrolytes in tissues. This more comprehensive theoretical approach has been successfully applied to the description of mechanical properties, swelling and passive transport of multi-electrolytes in cartilage and intervertebral disc (IVD).[60;61;64;65;216-219]

In 2007, Ateshian further extended the mixture theory to include chemical reactions among the phases composing the mixture.[4;5] In these theoretical frameworks it was demonstrated that the mixture theory can also be applied to the description of tissue growth and remodeling by cell division and alteration of the composition of the extracellular matrix.

In numerous studies, solute transport in charged hydrated soft tissues has been modeled by a mixture theory based approach.[49;85-87;122-124;136;215-219] In a similar fashion, in this study, the mixture theory is used as a theoretical framework for the investigation of transport phenomena (in the presence of binding interaction between solute and extracellular matrix) in the intervertebral disc (specific aim #3).

1.2.7 Significance and clinical relevance

In United States, more than 70% of all individuals experience symptoms of low back pain at some point in their lifetimes.[151] Therefore, low back pain represents a major health concern in the country.[107;151] Although the specific cause of low back pain remains unclear, symptoms have been associated with degeneration of IVD in the spine.[25;48;107;211] It is generally believed that poor nutritional supply is one of the mechanisms of disc degeneration.[13;75;80;148;198] Nutrient transport in IVD is complex and still poorly understood. The ultimate goal of this study is to provide a new realistic model for molecular transport in IVD which takes into account the inhomogeneous and anisotropic transport properties of the disc and the binding interactions of solutes with the ECM of the tissue.

This study will add new knowledge on transport mechanisms in IVD. The techniques developed in this study will also provide new tools for the experimental determination of transport properties in biological tissues and other areas of research, such as drug delivery. Moreover, the findings of this study will provide guidelines for the development of new methods and strategies for tissue engineering, since transport of molecules (e.g., nutrients, proteins, growth factors, etc.) is a major issue in engineering a healthy tissue.

1.3 Content of the thesis

The goal of this study is to investigate solute transport and binding reactions in intervertebral disc. In order to pursue this objective, new experimental techniques for investigating solute transport in biological tissues have been developed. Moreover, a theoretical framework based on the mixture theory has been elaborated for modeling solute transport and binding kinetics in charged hydrated soft tissues.

In Chapter 2, the mixture theory for charged hydrated soft tissues is extended to consider the case of a system composed by a solid matrix, embedded in a fluid phase containing one electrolyte and a non-charged solute able to reversibly bind to the solid matrix of the mixture. This new theoretical framework is used in Chapter 6 for the implementation of a finite element model for investigating solute transport and binding interactions in cartilaginous tissues.

In Chapter 3, a new imaging technique for the characterization of the anisotropic diffusion tensor by a single FRAP experiment is presented. The method is based on two independent analyses of the video-FRAP image series: the fast Fourier transform (FFT) and the Karhunen-Loève transform (KLT).[169] The principles of the method are presented. Computer simulated FRAP experiments are used for the optimization of experimental and data analysis parameters, such as the initial size of the bleach spot and the choice of frequencies used in FFT. The accuracy of the technique in the determination of the diffusion tensor has been estimated for several cases of anisotropic diffusion. The experimental validation of the new method is performed by measuring the fluorescein (332 Da) diffusion tensor in bovine coccygeal annulus fibrosus, and comparing the results with those reported in a previous study.[192] Finally, the method is applied for characterizing fluorescein diffusive properties in bovine meniscus.

In Chapter 4, the new FRAP technique, presented in Chapter 3, is applied for investigating the relationship between solute transport properties and morphology, and composition of the intervertebral disc. In this study, the anisotropic diffusive transport of a small solute (fluorescein, 332Da) has been characterized in three different regions of the human annulus fibrosus by FRAP. Additionally, imaging of different regions of annulus fibrosus have been performed by Scanning Electron Microscopy (SEM). The experimentally determined diffusive transport parameters are related to a morphologic parameter of the disc (i.e., density of microtubes), and the implications of tissue structure on solute transport are assessed.

In Chapter 5, a new method for the simultaneous determination of solute anisotropic diffusivity and binding reaction rates is presented. The new technique is based on Fourier analysis of video-FRAP images. The accuracy and the robustness of the technique are assessed by numerically simulated FRAP experiments. Finally, the method is applied to the experimental determination of diffusivity and binding parameters of a cationic solute, 5-dodecanoylaminofluorescein (DAF), in bovine coccygeal annulus fibrosus (AF). The results are compared to those reported in previous studies.

In Chapter 6, a numerical model for investigating the transport of solutes and binding interactions in cartilaginous tissues is presented. Based on the theoretical framework developed in Chapter 2, and on the findings reported in Chapters 3-5, a numerical analysis by a finite element model is performed. The results are discussed and compared to those reported in previous studies.

In Chapter 7, the most important findings of the study are discussed and summarized. Recommendations for future development of research in the field are also given.

Chapter 2: MIXTURE THEORY FOR CHARGED HYDRATED SOFT TISSUES

2.1 Introductory remarks

Soft hydrated tissues are multiphasic materials, constituted by a fibrous network of proteins, interstitial water, electrolytes (i.e., NaCl or $CaCl_2$), and other solutes. The fibrous matrix is often negatively charged. Many mechano-electrochemical coupling phenomena, such as ion-induced swelling, streaming potential and current, anomalous osmosis, and electro-osmosis observed in such charged tissues have been attributed to the electrostatic interactions among the fixed charges of the solid matrix and the electrolytes present in the interstitial water.[61] Additionally, some molecular solutes (e.g., growth factors, extracellular matrix components, etc.) can reversibly bind to binding sites present in the extracellular matrix of the tissue.[12;55] A theoretical model, able to describe the electro-mechanics and the transport phenomena within a charged hydrated soft tissue, is essential to elucidate mechanisms of nutrient transport,[85;86;215;222;223] and tissue growth and regeneration.[4;5;109;121]

Numerous theoretical models have been proposed to investigate the mechano-electrochemical behavior and transport in soft tissues, using several theoretical approaches, see review by de Boer (2000).[38] The theoretical approach followed in this thesis is based on the mixture theory, formerly formulated by Lai et al. (1991) for a system composed by a solid matrix embedded in a solution of one electrolyte,[114] and than extended by Gu et al. (1998) to consider multiple charged species.[61] Hereby, a theoretical framework, able to describe electro-mechanics and solute diffusive-convective-reactive transport in charged soft tissues, is presented.

2.2 Field equations

Consistent with the assumptions of the mechano-electrochemical theory,[61;114] hereby, a charged hydrated soft tissue is considered to be a mixture of: (1) an intrinsically incompressible, porous, permeable, negatively charged solid phase (hereby denoted with superscript *s*) characterized by the presence of binding sites (*S*); (2) an intrinsically incompressible interstitial fluid phase (superscript *w*); (3) an electrolyte phase constituted by two monovalent ion species (i.e., anion denoted with superscript –, and a cation denoted with superscript +); (4) a non-charged solute *F* (denoted with superscript *f*) able to reversibly bind to a binding site *S* of the solid phase of the mixture; and (5) a bound complex *B* (denoted with superscript *b*), product of the reaction between *F* and *S*. It is further assumed that: *B* is bound to the solid matrix and does not diffuse within the tissue; the binding reaction between *F* and *S* is reversible, so that *B* can also break into its original constituents (*F* and *S*).

2.2.1 Saturation condition

Following the same notation adopted by Gu et al. (1998),[61] , ϕ^α denotes the volume fraction of the component α (with $\alpha = s, w, +, -, f, b$), so that:

$$\phi^\alpha = \frac{dV^\alpha}{dV}, \qquad (2.1)$$

where V^{α} denotes the partial volume of the α-specie and V the volume of the whole mixture. In particular, ϕ^{s} is referred as the solidity, while ϕ^{w} represents the porosity of the tissue. The condition of the saturation of the mixture imposes that:

$$\sum_{\alpha} \phi^{\alpha} = 1 . \qquad (2.2)$$

It should be noted that ϕ^{+}, ϕ^{-}, ϕ^{f}, and ϕ^{b} are generally very small, so that they can be practically neglected. Therefore, Equation (2.2) can be reduced to:

$$\phi^{s} + \phi^{w} = 1 . \quad (2.3)$$

2.2.2 Continuity equations

The conservation of mass on each component of the mixture requires that:

$$\frac{\partial \alpha^{\alpha}}{\partial t} + \nabla \cdot (\alpha^{\alpha} \boldsymbol{v}^{\alpha}) = \hat{\rho}^{\alpha}, \quad (\alpha = s, w, +, -, f, b) \qquad (2.4)$$

where $\boldsymbol{v}^{\alpha}$ is the absolute velocity of the α-component of the mixture, ρ^{α} is its mass density, and $\hat{\rho}^{\alpha}$ is its rate of mass generation per unit of volume of the mixture. Note that, in this framework, it is assumed that mass generation is only due to reversible binding reaction between the solute F and the binding site S to generate the bound complex B (i.e., $\hat{\rho}^{\alpha} = 0$ for $\alpha = s, w, +, -$). Besides, since the sum of the rates of mass supply over all the constituents of the mixture must be zero ($\sum_{\alpha} \hat{\rho}^{\alpha} = 0$),[4] we have:

$$\hat{\rho}^f = -\hat{\rho}^b . \qquad (2.5)$$

The mass densities of the α-components are related to the true solid density ρ_T^{s}, true interstitial fluid density ρ_T^{w}, solute concentrations per unit of volume of interstitial fluid (i.e., c^+, c^-, c^f, c^b) and molecular weights (i.e., M^+, M^-, M^f, M^b), as it follows:

$$\alpha^s = \phi^s \alpha_T^s \qquad (2.6\text{ a})$$

$$\alpha^w = \phi^w \alpha_T^w \qquad (2.6\text{b})$$

$$\alpha^+ = \phi^w M^+ c^+ = \phi^+ \alpha_T^+ \qquad (2.6\text{c})$$

$$\alpha^- = \phi^w M^- c^- = \phi^- \alpha_T^- \qquad (2.6\text{d})$$

$$\alpha^f = \phi^w M^f c^f = \phi^f \alpha_T^f \qquad (2.6\text{e})$$

$$\alpha^b = \phi^w M^b c^b = \phi^b \alpha_T^b \qquad (2.6\text{f})$$

Assuming that each phase composing the mixture is intrinsically incompressible (i.e., for any α, the true density ρ_T^{α} is constant), and neglecting the volume fractions of ions, non-charged solute, and bound complex, the continuity equation of the mixture can be written as:

$$\nabla \cdot (\phi^s \boldsymbol{v}^s + \phi^w \boldsymbol{v}^w) = 0 . \qquad (2.7)$$

2.2.3 Electroneutrality condition

The solid phase is characterized by the presence of a negative fixed charge density (FCD). It will be assumed that, at any point of the mixture, the net electrical charge, due to the presence of both electrolytes and FCD, is zero. The condition of electroneutrality can then be written as:

$$c^F + c^- = c^+ , \qquad (2.8)$$

where c^F is the value of the negative FCD expressed in terms of equivalent moles per unit of interstitial fluid volume. Since it is assumed that the fixed charges on the solid matrix do not change with time, a continuity equation for FCD can be written as it follows:

$$\frac{\partial(\phi^w c^F)}{\partial t} + \nabla \cdot (\phi^w c^F \boldsymbol{v}^s) = 0 . \qquad (2.9)$$

Within the tissue, the electrical current density can be expressed as:

$$\boldsymbol{I}_e = F_c \phi^w (c^+ (\boldsymbol{v}^+ - \boldsymbol{v}^s) - c^- (\boldsymbol{v}^- - \boldsymbol{v}^s)), \qquad (2.10)$$

where F_c is the Faraday constant. From the combination of the electroneutrality condition and mass balances over FCD and the ions, the electrical current density must satisfy the following relationship:

$$\nabla \cdot \boldsymbol{I}_e = 0. \qquad (2.11)$$

2.2.4 Momentum equations

In this framework, body forces (e.g., gravitational, magnetic, etc.) and mass forces (i.e., inertia), will be neglected. Therefore, the momentum balance for the mixture reads:

$$\nabla \cdot \sigma = 0, \qquad (2.12)$$

where $\boldsymbol{\sigma}$ is the total stress of the mixture (tissue). Following the same approach as proposed by Lai et al. (1991),[114] and Gu et al. (1998),[61] the momentum equations for the interstitial fluid, the ions, and the non-charged solute are expressed through their electro-chemical potentials (μ^α):

$$-\alpha^\alpha \nabla \mu^\alpha + \sum_{\alpha} f_{\alpha\alpha}(\boldsymbol{v}^\alpha - \boldsymbol{v}^\alpha) = 0, \quad (\alpha \neq s; \beta = s, w, +, -, f) \qquad (2.13)$$

where $f_{\alpha\beta}$ is the frictional coefficient per unit of tissue volume between the inter-diffusing species α and β. Noted that the frictional coefficients are assumed to be symmetric (i.e., $f_{\alpha\beta} = f_{\beta\alpha}$) and, by definition, $f_{\alpha\beta} = 0$ when $\alpha = \beta$. Moreover, the frictional interactions between the bound complex B and the interstitial solution (i.e., fluid phase and solutes) have been included in the coefficients f_{ws}, f_{+s}, f_{-s}, and f_{fs}. Equation (2.13) indicates that, for interstitial fluid and solute phases, the only driving force for motion is the electrochemical potential, which is balanced by the frictional forces due to inter-diffusion between one phase and another. It should be noted that, in Equation (2.13), the contribution of $\hat{\rho}^f$ (i.e., mass generation due to binding reaction) to the balance of the momentum of the non-charged solute has been neglected. This assumption is valid for low concentrations of uncharged solute, since the body force imparted to F due to mass generation is proportional to its mass fraction ($\alpha^f / \sum_{\alpha} \alpha^{\alpha} \quad \alpha = s, w, +, -, f, b$).[4]

2.2.5 Force-flux relationships

The definitions of fluxes of interstitial fluid and solutes depend on the frame of reference. Consistently to previous formulations,[61;189;216;217] in this framework, the relative fluid and solutes fluxes (relative to the solid phase) will be chosen to describe the fluid and solutes transport in mixture. Therefore, the relative interstitial fluid flux ($\boldsymbol{J}^w$) is defined as:

$$\boldsymbol{J}^w = \phi^w (\boldsymbol{v}^w - \boldsymbol{v}^s). \qquad (2.14)$$

Similarly, the relative molar fluxes of solutes ($\boldsymbol{J}^{\alpha}$) are defined as:

$$\boldsymbol{J}^{\alpha} = \phi^w c^{\alpha} (\boldsymbol{v}^{\alpha} - \boldsymbol{v}^s) \quad (\alpha = +, -, f). \qquad (2.15)$$

Note that, since the bound complex is assumed to be attached to the solid phase, its relative molar flux is zero. Using Equations (2.13), (2.14), and (2.15), relative the molar fluxes of interstitial fluid phase, ions, and non-charged solute can be rewritten in terms of their electro-chemical potentials (see Appendix A.1 for details):[217]

$$\boldsymbol{J}^{w} = -\frac{K}{\phi^{w}}(\alpha^{w}\nabla\mu^{w} + \sum_{\alpha} H^{\alpha}\alpha^{\alpha}\nabla\mu^{\alpha}), \qquad (2.16)$$

and

$$\boldsymbol{J}^{\alpha} = H^{\alpha}c^{\alpha}\boldsymbol{J}^{w} - D^{\alpha}\alpha^{\alpha}\nabla\mu^{\alpha}/RT \quad (\alpha = +,-,f), \qquad (2.17)$$

where K is the intrinsic permeability of the solid phase, H^{α} is the hindrance factor (or convection coefficient) of the α-component, and D^{α} the intrinsic diffusion coefficient (see Appendix A.1 for details).

2.2.6 Constitutive equations

For an isotropic hydrated charged mixture with infinitesimal deformations, the constitutive equations for each of the phases are:[61;189]

Solid phase $$\sigma = -p\boldsymbol{I} + \alpha tr(\boldsymbol{E})\boldsymbol{I} + 2\mu\boldsymbol{E} + T_{c}\boldsymbol{I} \qquad (2.18)$$

Fluid phase $$\mu^{w} = \mu_{o}^{w} + [p - RT\Phi(c^{+} + c^{-} + c^{f}) + B_{w}e]/\alpha_{T}^{w} \qquad (2.19)$$

Cation $$\mu^{+} = \mu_{o}^{+} + \frac{RT}{M^{+}}\ln(\alpha^{+}c^{+}) + \frac{F_{c}\psi}{M^{+}} \qquad (2.20)$$

Anion $$\mu^{-} = \mu_{o}^{-} + \frac{RT}{M^{-}}\ln(\alpha^{-}c^{-}) - \frac{F_{c}\psi}{M^{-}} \qquad (2.21)$$

Free solute $$\mu^{f} = \mu_{o}^{f} + \frac{RT}{M^{f}}\ln(\alpha^{f}c^{f}) \qquad (2.22)$$

Bound solute $$\mu^{b} = \mu_{o}^{b} + \frac{RT}{M^{b}}\ln(\alpha^{b}c^{b}) \qquad (2.23)$$

In Equation (2.18), p is the interstitial fluid pressure, λ and μ are the elastic constants of the solid matrix (Lamé constants), and T_c, known as chemical stress, is in general a function of solute (charged and uncharged) concentrations. In Equation (2.19), Φ is the osmotic coefficient, B_w is the inter-phase coupling coefficient,[61;114] e is the trace of the strain tensor ($\boldsymbol{E}$) defined as:

$$\boldsymbol{E} = \frac{1}{2}(\nabla \boldsymbol{u} + \nabla \boldsymbol{u}^T), \qquad (2.24)$$

where $\boldsymbol{u}$ is the displacement of the solid matrix (note that $\partial \boldsymbol{u}/\partial t = \boldsymbol{v}^s$). In Equations (2.19-23), μ_o^α (with $\alpha = w, +, -, f, b$) indicate the reference chemical potential of the α-specie; the quantities γ^+, γ^-, γ^f, and γ^b, are the activity coefficients of the cation, anion, uncharged solute and bound complex, respectively; R is the universal gas constant; T is the absolute temperature; α is the electrical potential.

2.2.7 Reversible binding reaction

In previous studies, reversible binding reactions between a solute and the solid matrix of tissues and hydrogels have been described by the Langmuir binding model.[53;222] Consistent with these studies, it is assumed that the reversible chemical reaction between the non-charged solute F and the binding site S, generating the bound complex B, can be expressed as:

$$F + S \underset{K_{off}}{\overset{K_{on}}{\rightleftarrows}} B , \qquad (2.25)$$

where k_{on} and k_{off} are the rates of association (binding) and dissociation (unbinding) of the constituents. The relation presented in Equation (2.25) can be described using the law of mass action:[53;222] the rate of generation of the bound complex B is proportional to the product of the concentration of F and S; the rate of dissociation of B is proportional to its concentration. It follows that:

$$\frac{dc^b}{dt} = k_{on} c^f c^{bs} - k_{off} c^b , \qquad (2.26a)$$

$$\frac{dc^f}{dt} = -k_{on} c^f c^{bs} + k_{off} c^b , \qquad (2.26b)$$

$$\frac{dc^{bs}}{dt} = -k_{on} c^f c^{bs} + k_{off} c^b , \qquad (2.26c)$$

where c^{bs} is the concentration of binding sites per unit of volume of fluid phase. Summing Equations (2.26a) and (2.26c) yields:

$$\frac{dc^{bs}}{dt} + \frac{dc^b}{dt} = 0 . \qquad (2.27)$$

The above relation indicates that, at any time, the sum of the concentrations of the binding sites and the bound solute is constant. Integration of Equation (2.27) provides an expression for the concentration of the binding sites present in the extracellular matrix of the tissue:

$$c^{bs}(t) = c_o^{bs} + c_o^{b} - c^{b}(t), \qquad (2.28)$$

where c_o^{bs} and c_o^{b} are the initial concentrations of binding sites and bound solute (at $t = 0$). Equation (2.28) is used to eliminate c^{bs} in Equation (2.26a), yielding to:

$$\frac{dc^{b}}{dt} = k_{on}(c_o^{bs} + c_o^{b} - c^{b})c^{f} - k_{off}c^{b}. \qquad (2.29)$$

Equation (2.29) provides a relationship between the non-charged solute and the bound complex within the mixture.

2.2.8 Summary of governing equations

The balance of linear momentum for the mixture and the conservation of mass for each of phases lead to the following set of governing equations:[61;114;189;215;217]

Momentum balance for the mixture $\nabla \cdot \sigma = 0$, (2.12)

Mass balance for the mixture $\nabla \cdot (\boldsymbol{v}^{s} + \boldsymbol{J}^{w}) = 0$, (2.30)

Mass balance for cation $\partial(\phi^{w}c^{+})/\partial t + \nabla \cdot (\boldsymbol{J}^{+} + \phi^{w}c^{+}\boldsymbol{v}^{s}) = 0$, (2.31)

Mass balance for anion $\partial(\phi^{w}c^{-})/\partial t + \nabla \cdot (\boldsymbol{J}^{-} + \phi^{w}c^{-}\boldsymbol{v}^{s}) = 0$, (2.32)

Mass balance for F and B

$$\partial(\phi^w c^f + \phi^w c^b)/\partial t + \nabla \cdot (\boldsymbol{J}^f + \phi^w c^f \boldsymbol{v}^s + \phi^w c^b \boldsymbol{v}^s) = 0, \tag{2.33}$$

Law of mass action

$$\frac{dc^b}{dt} = k_{on}(c_o^{bs} + c_o^b - c^b)c^f - k_{off}c^b . \tag{2.29}$$

Using the electroneutrality condition formulated in Equation (2.8) and applied to the current density in Equation (2.11), one can get the following equivalent equations to substitute the mass balances on the ions expressed in Equations (2.33-34):[189]

Electrical current condition

$$\nabla \cdot \boldsymbol{J}^+ - \nabla \cdot \boldsymbol{J}^- = 0 , \tag{2.34}$$

Ion diffusion-convection equation

$$\partial(\alpha^w c^k)/\partial t + \nabla \cdot (\boldsymbol{J}^+ + \boldsymbol{J}^- + \alpha^w c^k \boldsymbol{v}^s) = 0 , \tag{2.35}$$

where $c^k = c^+ + c^-$.

Assigned the boundary conditions, the closed set of Equations (2.12), (2.29), (2.30), (2.31), (2.32), and (2.33) [or (2.12), (2.29), (2.30), (2.33), (2.34), and (2.35)] provide a unique solution to the problem of solute diffusive-convective-reactive transport in charged hydrated soft tissues. The definition of the boundary conditions is left to the next section.

2.2.9 Boundary conditions

In order to determine a unique solution of the governing equations, specific boundary conditions at the material surface are required. At the boundaries, it is required that the total stress and the electro-chemical potential of each phase are continuous, or the continuity of the solid displacement ($\boldsymbol{u}$) and the fluxes ($\boldsymbol{J}^{\alpha}$) of the α-species. These conditions can be expressed as it follows:

$$\boldsymbol{u} = \boldsymbol{u}^{*} \quad \mu^{\alpha} = \mu^{\alpha*}, \quad (\alpha = w,+,-,f) \tag{2.36}$$

or

$$\sigma \cdot \boldsymbol{n} = \boldsymbol{t} \quad \boldsymbol{J}^{\alpha} \cdot \boldsymbol{n} = \boldsymbol{J}^{\alpha*} \cdot \boldsymbol{n}, \quad (\alpha = w,+,-,f) \tag{2.37}$$

where $\boldsymbol{n}$ represents the normal to the boundary of the system, and $\boldsymbol{t}$ is the traction. The superscript (*) indicates quantities outside the boundary of the mixture. Note that, the boundary conditions for the bound complex are given by solving Equation (2.29) at the boundaries of the mixture.

2.3 Summary

The field equations of the mixture theory have been presented. Solute transport and binding interactions with the extracellular matrix of a charged hydrated soft tissue have been described in terms of solid displacement and electrochemical potentials of the components of the mixture. Based on this theoretical framework, in Chapter 6, a finite element model for solute diffusive-convective-reactive transport will be developed.

Chapter 3: DEVELOPMENT OF NEW TECHNIQUE FOR THE DETERMINATION OF ANISOTROPIC DIFFUSION IN BIOLOGICAL TISSUES

3.1 Introductory remarks

In avascular tissues (e.g., cartilage, ligaments, intervertebral disc, etc.), diffusion is a major transport mechanism for solutes.[150;177;203] Therefore, in order to elucidate the transport mechanisms of nutrients, oxygen, growth factors, or extracellular matrix components, the determination of solute diffusivity is crucial. Due to their unique and complex morphology, the diffusion of solutes in such tissue may be anisotropic.[50;84;96;119;192]

In the last two decades, due to the commercial availability of a growing number of fluorescently labeled molecular probes, fluorescence photobleaching techniques have been extensively used for the determination of solute diffusivity both in cells and biological tissues.[117;119;125;139;166;179;184;192] Moreover, several fluorescence photobleaching methods have been developed for investigating anisotropic diffusivity. For instance, Leddy et al. (2006) developed a continuous point photobleaching method to determine the ratio between the two principal components of the diffusion tensor of large molecules in porcine ligament.[119] Tsay and Jacobson (1991),[195] using spatial Fourier analysis of FRAP images, developed a method for the determination of the components of the two-dimensional (2D) diffusion tensor along the fixed reference coordinate system. In a previous study, Travascio and Gu (2007) reported an alternative method for determining the principal components of a three-dimensional (3D) anisotropic diffusion tensor using three independent FRAP tests in three orthogonal sections of bovine coccygeal disc tissue.[192] However, none of these studies provided a method which could completely determined the solute diffusion tensor in biological tissues in a single experiment.

In this Chapter, a new method for quantitatively characterizing the 2D anisotropic diffusion tensor by one FRAP test is presented. The theoretical approach for this new technique is shown. Moreover, the accuracy and robustness of the new method are investigated by numerical simulations of FRAP tests. Additionally, the experimental validation with real FRAP experiments is reported.

3.2 Theoretical background

Hereby, the theoretical approach for the new FRAP technique is reported. The method is based on two independent analyses of the video-FRAP image series: the fast Fourier transform (FFT) and the Karhunen-Loève transform (KLT). The principle of FFT analysis of FRAP data is first introduced for the ideal case of isotropic diffusion, and then applied to the more general case of anisotropic diffusion. A description of KLT analysis is also reported. Note that the theoretical formulation presented in this section is based on the assumption that diffusion is a two-dimensional (2D) process occurring in the optical plane of the microscope objective (*x*,*y*). This assumption is valid when the thickness of the sample used in the experiments is comparable with the optical slice of the microscope. For confocal laser scanning microscope (CLSM) the optical slice is ~5-8 μm. In general, in bulk samples (i.e., thickness of the sample >> optical slice of the microscope objective), fluorescence recovery is a three-dimensional (3D) process, with diffusion also occurring in the orthogonal direction to the focal plane of the microscope objective (*z*-direction). While several analytical and numerical models for 3D FRAP tests with Confocal Laser Scanning Microscope (CLSM) have been proposed for the case of isotropic diffusion,[14;20;21] an extension of the FFT approach to the 3D case has not been developed yet, due to the difficulty in collecting 3D images of fluorescence recovery in real time. However, by using the Multi-Layer Bleaching (MLB) technique developed by Travascio and Gu (2007),[192] it is possible to minimize the diffusive flux in the z-direction and recover a 2D diffusive transport in bulk samples. The details of MLB are presented and discussed in Section 3.3

3.2.1 Principles of FFT in FRAP data analysis

In the last two decades, the use of FFT for analysis of fluorescence recovery data, formerly introduced by Smith et al. (1979),[178] has become more and more popular.[8;9;162;192-195] With respect to other methods for isotropic[6] or anisotropic[119;188] 2D diffusion cases, the major advantage of using FFT approach is that the analysis is independent from the fluorescence intensity distribution within the bleached spot of the sample. Hereby, the principles of FFT in FRAP data analysis are first presented for the ideal case of isotropic diffusion and then extended to the more general case of anisotropic diffusion.

3.2.1.1 Isotropic diffusion

Under the assumptions that diffusion is 2D and isotropic, the field equation for solute concentration (c) within a medium can be obtained based on the conservation of mass and Fick's law:

$$\frac{\partial c(x,y,t)}{\partial t} = D\left(\frac{\partial^2 c(x,y,t)}{\partial x^2} + \frac{\partial^2 c(x,y,t)}{\partial y^2}\right), \qquad (3.1)$$

where (*x,y*) are the coordinates of the imaging system within the focal plane of the microscope objective, and *D* the diffusion coefficient (assumed to be constant with time and position within the focal plane). Let *C*(*u*,*v*,*t*) be the 2D Fourier transform of *c*(*x*,*y*,*t*), defined as:

$$C(u,v,t) = \int_{-\infty}^{\infty}\int_{-\infty}^{\infty} c(x,y,t)e^{-i2\pi(ux+vy)}dxdy\,, \qquad (3.2)$$

for an arbitrary initial condition, the solution of Equation (3.1) in the space of frequencies (*u*,*v*) is:[178;195]

$$C(u,v,t) = C(u,v,0)exp[-4\alpha^2(u^2+v^2)Dt]\,. \qquad (3.3)$$

In a video-FRAP image, the intensity of the fluorescence emission is assumed to be proportional to the concentration of the fluorescent probes present in the microscope objective field. This assumption is experimentally met when the concentration of the fluorescent probe is not so high as to cause self-quenching of fluorescence.[9] Therefore, solute diffusion can be related to the rate of recovery of fluorescence intensity according to the following relationship:

$$\frac{I(u,v,t)}{I(u,v,0)} = \frac{C(u,v,t)}{C(u,v,0)} = exp[-4\alpha^2(u^2+v^2)Dt]\,, \tag{3.4}$$

where I is the 2D FFT of the fluorescence intensity of a series of video-FRAP images, evaluated at the frequency couple (u,v). Curve-fitting the 2D FFT of fluorescence intensity of a time series of video-FRAP images with Equation (3.4), yields the diffusion coefficient D.

3.2.1.2 Anisotropic diffusion

Assuming that diffusion is 2D and orthotropic, the diffusion equation reads:

$$\frac{\partial c(x,y,t)}{\partial t} = D_{xx}\frac{\partial^2 c(x,y,t)}{\partial x^2} + D_{yy}\frac{\partial^2 c(x,y,t)}{\partial y^2} + 2D_{xy}\frac{\partial^2 c(x,y,t)}{\partial x \partial y}\,, \tag{3.5}$$

where D_{xx}, D_{xy} and D_{yy} are components of diffusion coefficient tensor (***D***) in the coordinate system fixed to the microscope objective (x,y). Applying the same approach used in the previous section, Equation (3.5) is transformed and solved in the 2D Fourier space of frequencies (u,v). Thus, the normalized fluorescence intensity of a time series of video-FRAP images can be expressed as:[192;195]

$$\frac{I}{I_o} = exp[-4\alpha^2(u^2+v^2)D(\xi)t]\,, \tag{3.6}$$

where ξ is the angle defined by the wave vector specified by u and v, and the positive u-axis (Figure 3.1):

$$\xi = \tan^{-1}\frac{v}{u}, \qquad (3.7)$$

and:

$$\begin{aligned} D(\xi) &= D_{xx}\frac{u^2}{u^2+v^2} + D_{yy}\frac{v^2}{u^2+v^2} + D_{xy}\frac{2uv}{u^2+v^2}\,. \\ &= D_{xx}cos^2\alpha + D_{yy}sin^2\alpha + 2D_{xy}sin\xi cos\xi \end{aligned} \qquad (3.8)$$

By curve-fitting the photobleaching recovery data with Equation (3.6), one can obtain $D(\xi)$ which depends on the choice of the frequencies u and v (or ξ), see Equation (3.8).

Tsay and Jacobson (1991) proposed a method for obtaining the values of D_{xx} or D_{yy} individually, by choosing special frequency couples along the axes of the Fourier space, namely $(u,0)$ and $(0,v)$,[195] see Equation (3.8). However, it should be noted that the values of D_{xx} and D_{yy} depend on the relative orientation of the principal directions of the diffusion tensor (x',y') with respect to the fixed coordinate system of the microscope objective (x,y).

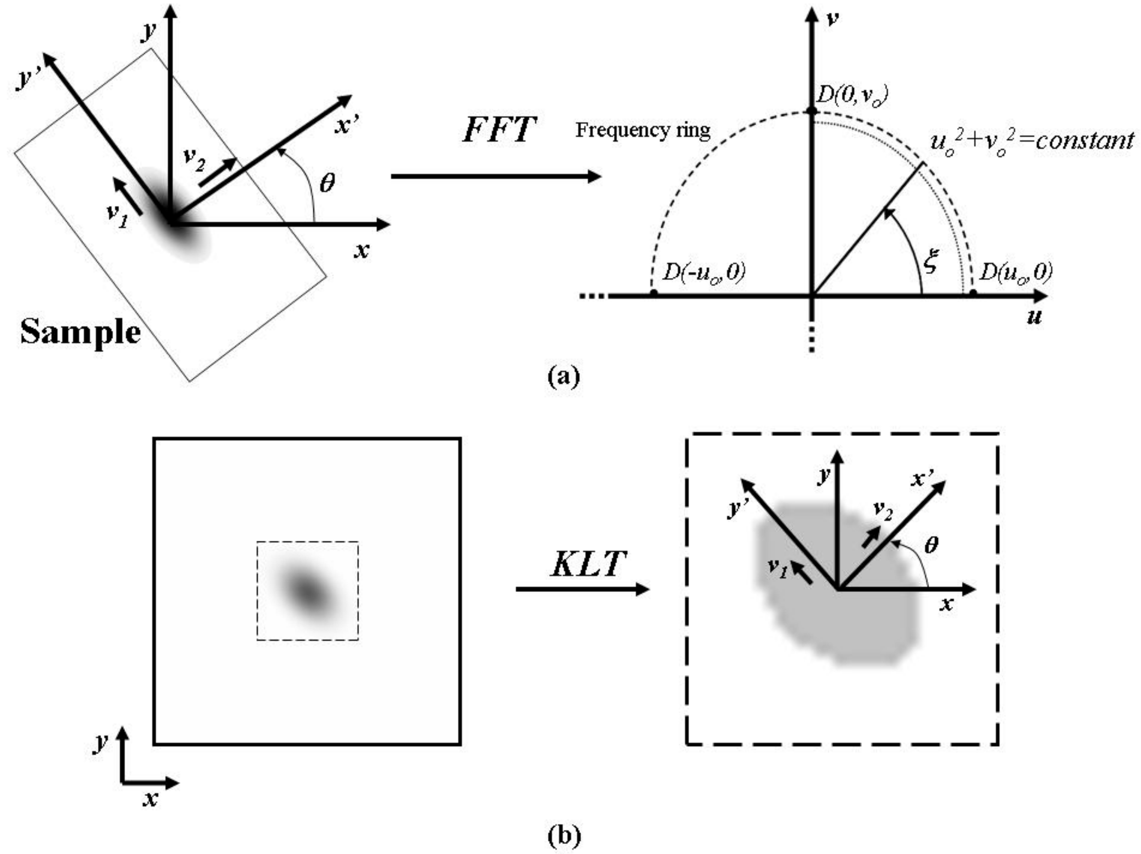

Figure 3.1 (a) Transformation of video-FRAP image into the Fourier space using FFT. The orientation of the principal directions of the sample with respect to the fixed coordinate system is θ. The eigenvectors ($\mathbf{v}_1$, $\mathbf{v}_2$) of the covariance matrix $\mathbf{C}$, and the frequency ring used for the determination of D_{av}(--) and D^{+}_{av} (…) are shown. (b) Determination of the orientation (θ) of $\mathbf{D}$ by KLT analysis of the bleached spot.[194]

Travascio and Gu (2007) proposed a FRAP method for the determination of the principal components of the 3D anisotropic diffusion tensor in bulk tissue.[192] The technique is based on three independent FRAP experiments, performed on three principal planes of the tissue, individualized by the coordinate systems (x,y), (y,z), and (x,z). It can be proven that, in the focal plane (x,y), the mean value of $D(\xi)$ [averaged over an arc of circumference with u^2+v^2 = constant in the (u,v) space, see Figure 3.1] is given as follows:[192]

$$D_{av}^{xy} = \alpha^{-1}\int_0^{\alpha} D(\xi)d\xi = \frac{tr^{xy}(\boldsymbol{D})}{2} = \frac{D'_{xx} + D'_{yy}}{2}. \qquad (3.9)$$

In the above equation, $\mathrm{tr}^{xy}(\boldsymbol{D})$ indicates the trace of the diffusion tensor $\boldsymbol{D}$ (summation of principal components of diffusion tensor D'_{xx} and D'_{yy}) in the plane (x,y). Note that, $\mathrm{tr}^{xy}(\boldsymbol{D})$ is an invariant in the plane (x,y). By measuring the average of $D(\xi)$ in the two other principal planes of the tissue (individualized by (y,z) and (x,z), respectively), one can determine the three principal components of $\boldsymbol{D}$ as it follows:[192]

$$\begin{aligned} D_{av}^{xy} &= D'_{xx} + D'_{yy} \\ D_{av}^{yz} &= D'_{yy} + D'_{zz} \qquad (3.10) \\ D_{av}^{xz} &= D'_{xx} + D'_{zz} \end{aligned}$$

3.2.2 Characterization of 2D anisotropic diffusion tensor in a single FRAP experiment

The components of diffusion tensor ($\boldsymbol{D}$) depend upon the choice of the coordinate system. Let (x,y) stand for a Cartesian coordinate system which is fixed with respect to a microscope imaging system (i.e., fixed coordinate system). The components of $\boldsymbol{D}$ in (x,y) are D_{xx}, D_{xy}, and D_{yy}. Let (x',y') stand for a Cartesian coordinate system in which the matrix of the diffusion tensor is diagonal with components D'_{xx} and D'_{yy}. Hereby, the (x',y') coordinate system will be denoted as "material coordinate system" as it is oriented in the principal directions of the diffusion tensor. Defining θ as the angle representing the orientation of the material coordinate system with respect to the fixed coordinate system, there always exists a rotation matrix, $\boldsymbol{R}$, defined as:

$$\boldsymbol{R} = \begin{bmatrix} \cos\theta & -\sin\theta \\ \sin\theta & \cos\theta \end{bmatrix}, \qquad (3.11)$$

such that:

$$\begin{bmatrix} D_{xx} & D_{xy} \\ D_{xy} & D_{yy} \end{bmatrix} = \begin{bmatrix} \cos\theta & -\sin\theta \\ \sin\theta & \cos\theta \end{bmatrix} \begin{bmatrix} D'_{xx} & 0 \\ 0 & D'_{yy} \end{bmatrix} \begin{bmatrix} \cos\theta & \sin\theta \\ -\sin\theta & \cos\theta \end{bmatrix}, \qquad (3.12)$$

see Figure 3.1. From the above equation it follows that:

$$D'_{xx} + D'_{yy} = D_{xx} + D_{yy} = tr(\boldsymbol{D}), \qquad (3.13)$$

$$D'_{xx} - D'_{yy} = \frac{D_{xy}}{\sin\theta\cos\theta}. \qquad (3.14)$$

In this method, the principal components of the 2D diffusion tensor (D'_{xx}, D'_{yy}) can be calculated by Equations (3.13) and (3.14) if the values of $tr(\boldsymbol{D})$, D_{xy}, and θ are known.

In the previous section, it has been shown that the value of tr($\boldsymbol{D}$) can be obtained via Equation (3.9) by averaging $D(\xi)$ over the arc of an circumference (with u^2+v^2 = *constant*) spanning from 0 to π. Using a similar approach, the value of D_{xy} can be found by limiting the average of $D(\xi)$ from 0 to $\pi/2$:[194]

$$D^{+}_{av} = (\frac{\alpha}{2})^{-1} \int_{0}^{\frac{\alpha}{2}} D(\xi) d\alpha = \frac{tr(\boldsymbol{D})}{2} + \frac{2D_{xy}}{\alpha}. \qquad (3.15)$$

The orientation of the diffusion tensor, θ, (i.e., the orientation of the material coordinate system) is related to the shape of the bleached spot during the recovery phase. The experimental determination of the value of θ is achieved by performing Karhunen-Loève Transform (KLT) analysis of the bleached spot of a video-FRAP image. The details of the technique are reported in the next Section.

3.2.3 Karhunen-Loève Transform (KLT)

During a FRAP experiment, for the case of isotropic diffusion, the initially circular bleached spot keeps a circular shape during recovery. On the other hand, if diffusion is anisotropic, the shape of the bleached spot will change, from a circle to an ellipse.[103] The orientation of the semiminor axis of the ellipse, with respect to (x,y), coincides with the orientation of the largest principal component of $\boldsymbol{D}$ (i.e., θ) with respect to (x,y), see Figure 3.1. Thus, the orientation of the tensor can be determined by Karhunen-Loève Transform (KLT) analysis of the bleached spot during the recovery phase. Karhunen-Loève Transform is an imaging technique for determining the orientation of the principal axes of an image (e.g., ellipse).[169] Briefly, let $\boldsymbol{P}_i$ stand for the position vector (x_i,y_i) of each pixel within the bleached spot. The covariance matrix ($\boldsymbol{C}$ of order 2x2) of the vector population $[\boldsymbol{P}_i,\ i=1,2,\ldots n]$ is symmetric. The eigenvectors of $\boldsymbol{C}$ are the principal directions of the image, i.e., the major axes of the (elliptical) bleached spot. Note that the second principal vector ($\boldsymbol{v}_2$) of $\boldsymbol{C}$ corresponds to the semiminor axis of the ellipse (denoted as x'-direction in Figure 3.1), which is the direction of the largest principal value of the diffusion tensor. Figure 3.2 shows a typical KLT on a video-FRAP image. Around the bleached area, any pixels with light intensity of 10% lower than the average intensity of image background were considered belonging to the bleached spot and chosen as data points $\boldsymbol{P_i}$ for the KLT analysis, see Section 3.4.5. After $tr(\boldsymbol{D})$, D_{xy} and θ are determined, the principal components of $\boldsymbol{D}$ (i.e., D'_{xx} and D'_{yy}) can be calculated by Equations (3.13) and (3.14).

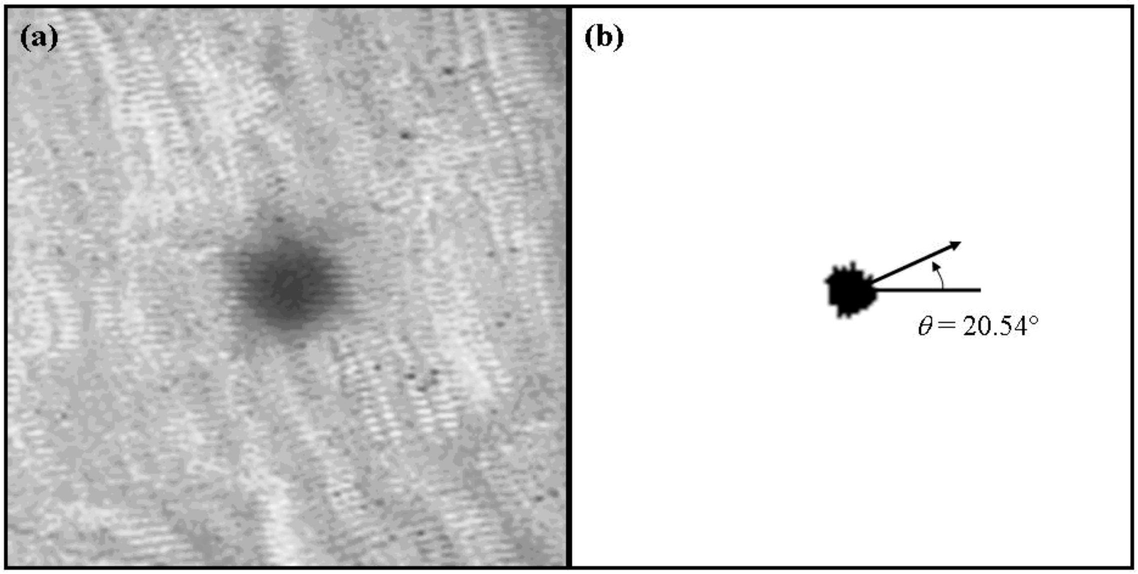

Figure 3.2 Selection of points $\boldsymbol{P_i}$ for the covariant matrix $\boldsymbol{C}$. (a) original video-FRAP image, the bleached spot is shown. (b) Around the bleached area, any pixels with light intensity of 10% lower than the average intensity of image background were considered belonging to the bleached spot and chosen as data points $\boldsymbol{P_i}$ for the KLT analysis.

3.3 Multi-Layer Bleaching (MLB)

In a FRAP experiment, when a tissue sample is bleached over its whole thickness, fluorescence recovery observed in the focal plane of the microscope objective is a 2D diffusive phenomenon. This condition is practically achievable when the thickness of the sample is comparable to the optical slice of the microscope objective (e.g., in membranes,[147] polymeric films,[196] etc.). In FRAP tests on bulk samples (thickness >>10 μm) performed by a CLSM, the bleached region only extends over the optical slice

(~5-8 μm) of the microscope objective, see Figure 3.3. Therefore, the presence of a gradient of concentration of fluorescent solute in the direction orthogonal to the focal plane (*z*-direction) causes fluorescence recovery to be a 3D diffusion phenomenon.[14;20;159] In the theoretical approach presented in the previous section, the contribution of the diffusive flux in the *z*-direction is neglected. Consequently, if applied to real FRAP experiments on bulk samples, this technique would overestimate the diffusion coefficient (*D*). The overestimation of *D* depends on two factors: (1) the ratio of the diameter of the bleach spot (*d*) in the focal plane of the microscope objective, to the thickness (*H*) of the bleached volume; and (2) the ratio of the diffusion coefficient in the *z*-direction to the averaged diffusion coefficient in the focal plane (D_α/D).[192]

By numerically simulated 3D FRAP experiments, Travascio and Gu (2007) quantified the overestimation of the trace of the diffusion tensor (tr(***D***)) by using a 2D FFT approach,[192] see Figure 3.4. It was found that the overestimation of tr(***D***) increases with the ratio D_α/D but decreases with H/d. By increasing the height of the bleached volume (cylinder), the relative error decreases (less than 7% for $D_\alpha/D=2$, when $H/d=2$) and, theoretically, it could be reduced to zero for sufficiently large values of H/d (or small values *of* D_α/D). This indicates that the diffusive flux in the z-direction could be negligible under certain conditions.

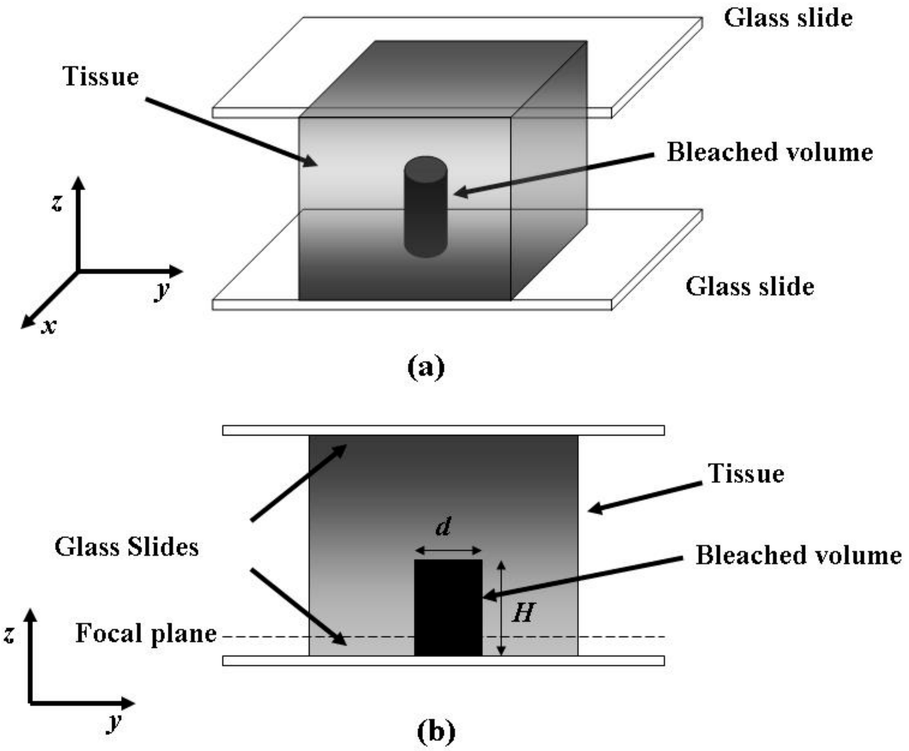

Figure 3.3 FRAP in bulk samples: (a) When a bulk sample is photobleached by a CLSM, the bleached volume does not extend over the entire thickness of the specimen (b) cross-sectional view of the sample.[192]

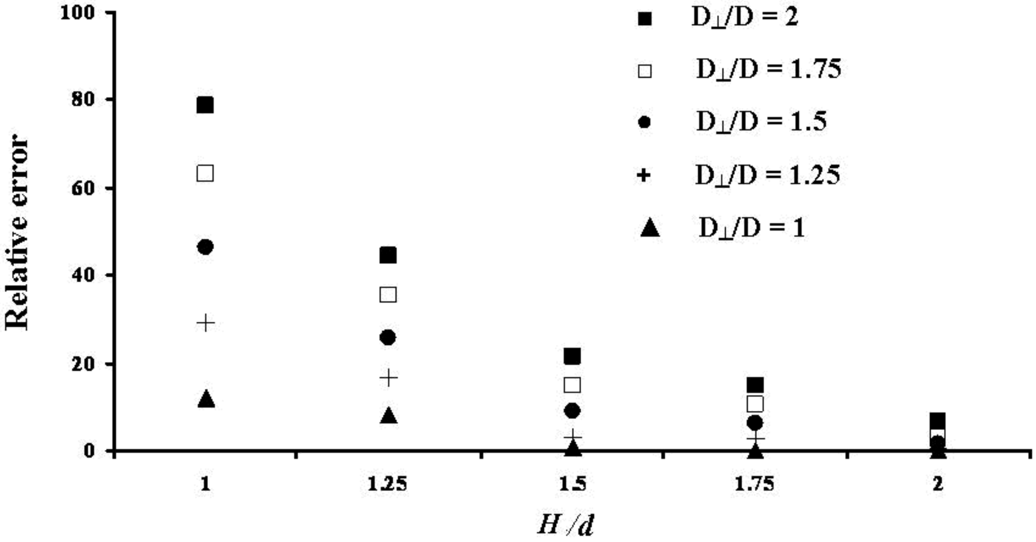

Figure 3.4 Relative error in the estimation of tr(***D***) vs. *H/d* parametric with the anisotropic ratio D_{α}/D.[192]

In order to increase the thickness of the bleached volume, a multi-layer bleaching (MLB) approach can be used. The principle of MLB is based on sequentially bleaching several layers within the bulk sample before acquiring the time series of fluorescence recovery images. In theory, by using MLB, the entire thickness of the sample could be bleached. In practice only a few layers can be sequentially bleached before fluorescence recovery occurs in the earlier bleached planes.

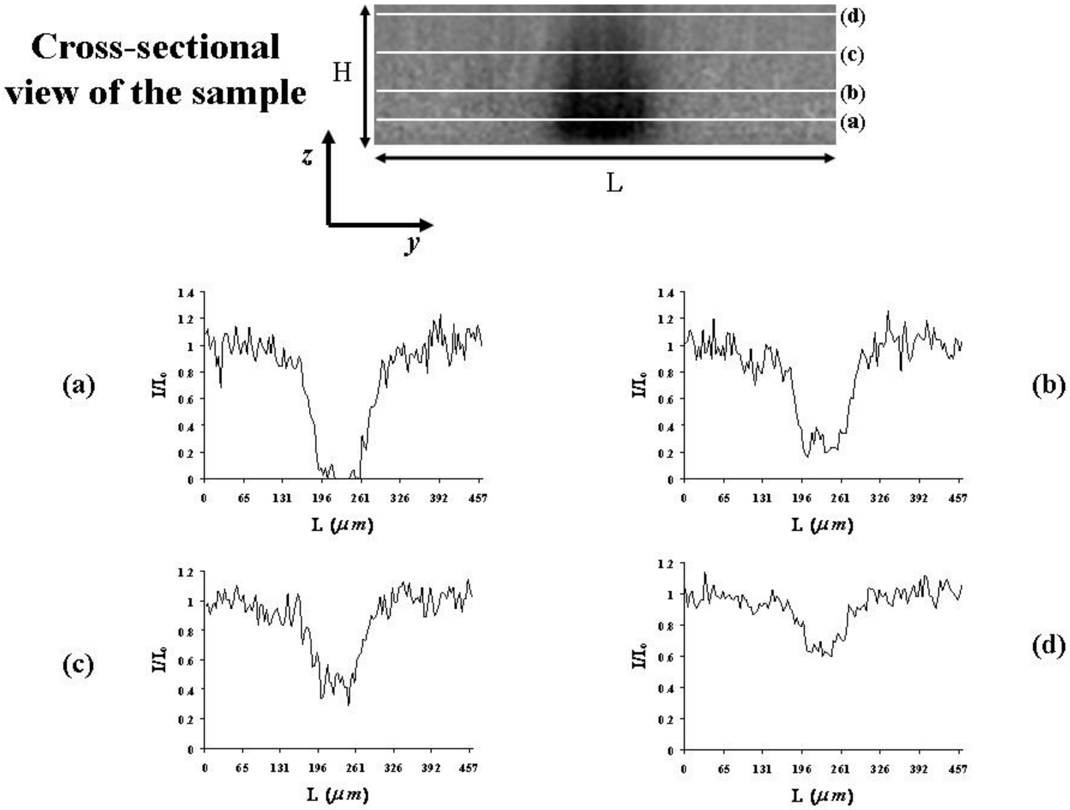

Figure 3.5 Cross-sectional view of meniscus sample after MLB. The distributions of the normalized light intensity (i.e., normalized fluorescent probe concentration) at several layers within the sample are shown (a-d).[194]

Figure 3.5 shows the bleached volume generated after sequentially bleaching two layers of bovine meniscus sample (30 μm thickness) loaded with fluorescein. The magnitude of the bleached volume was observed by acquiring a stack of images of the sample in the *z*-direction immediately after bleaching. The profiles of the normalized fluorescent light intensity at several layers of the sample are shown. From the fluorescence intensity distribution at each layer of the sample, the total bleached volume can be reconstructed and, by numerical simulations, the overestimation of tr(***D***) can be quantified.[192;194]

3.4 Methods

Numerically simulated FRAP experiments were used to validate the method proposed and to evaluate its sensitivity to experimental parameters, such as the initial size of the bleached spot, the choice of the set of the frequencies (*u,v*), the orientation of the tensor ***D,*** and experimental noise. The method was also experimentally validated by analyzing the images from the real FRAP experiments on bovine annulus fibrous (AF), and comparing the results obtained to those reported in the literature.[192] Finally, the approach was applied to the characterization of ***D*** of fluorescein in bovine meniscus.

3.4.1 Computer simulation of FRAP test

Computer simulations of 2D anisotropic diffusive recovery of a fluorescent probe after photobleaching were performed by a finite element method package (COMSOL® 3.2, COMSOL Inc., Burlington, MA). The computational domain used in the simulations comprised a mesh of approximately 13000 quadratic Lagrange triangular elements. The implicit solver of COMSOL® (based on the implicit Euler backward scheme) was used for the simulations, and the convergence criterion for the solution was the relative error tolerance of less than 0.001. In the simulations, it was assumed that the initial fluorescent probe concentration was uniform ($c=c^*$) within the sample and zero within the bleached spot. At the boundaries of the simulation domain (4x4 mm^2), the concentration of the fluorescent probe was assumed to be constant ($c=c^*$). In each simulated case, fluorescence recovery was almost complete (>95% of the initial concentration value in the sample c^*). For data analysis purposes, a time series of 200 images (8-bit grey scale) of 500x500 μm^2 (128x128 pixel) representing the fluorescence recovery on the focal plane of the microscope objective, was extracted from the whole simulation domain (4x4 mm^2), see Figure 3.6.

The accuracy of the new technique was evaluated with respect to several physical parameters, such as the ratio of the principal components of the diffusion tensor (anisotropic ratio), and the orientation of $\boldsymbol{D}$. In particular, 3 different anisotropic cases were studied (D'_{xx} = 1.5x, 2x and 3x of D'_{yy}). The values of D'_{xx} ranged from 10^{-8} to 10^{-6} cm^{2}s^{-1}. The orientation of the tensor (θ) also varied from $0°$ to $90°$ for each of the anisotropic cases studied.

The accuracy of the method was also tested with respect to several experimental parameters. The sensitivity of the method to the ratio of the frame size (L) to the initial diameter (d) of the bleached spot was investigated. For each anisotropic case studied, different values of d were investigated, so that the ratio L/d varied from 1 to 16. Additionally, the method was also tested when different sets of frequencies were used in the integrations present in Equations (3.9) and (3.15). Frequency rings,[195] ranging from 'Ring 2' to 'Ring 10', were used in the data analysis of fluorescence recovery images. It should be noted that "frequency ring" refers to a set of frequency couples (u,v) describing an arc in the Fourier space, see Figure 3.1 for an illustration. However, since in FFT analysis the data are discrete, the frequency ring is not a continuous arc. Table 3.1 lists the sets of frequency couples (u,v) composing the rings (up to 'Ring 6') in the first quadrant ($0 \leq \alpha \leq \pi/2$) of the Fourier space. The components of higher frequency rings can be easily derived.

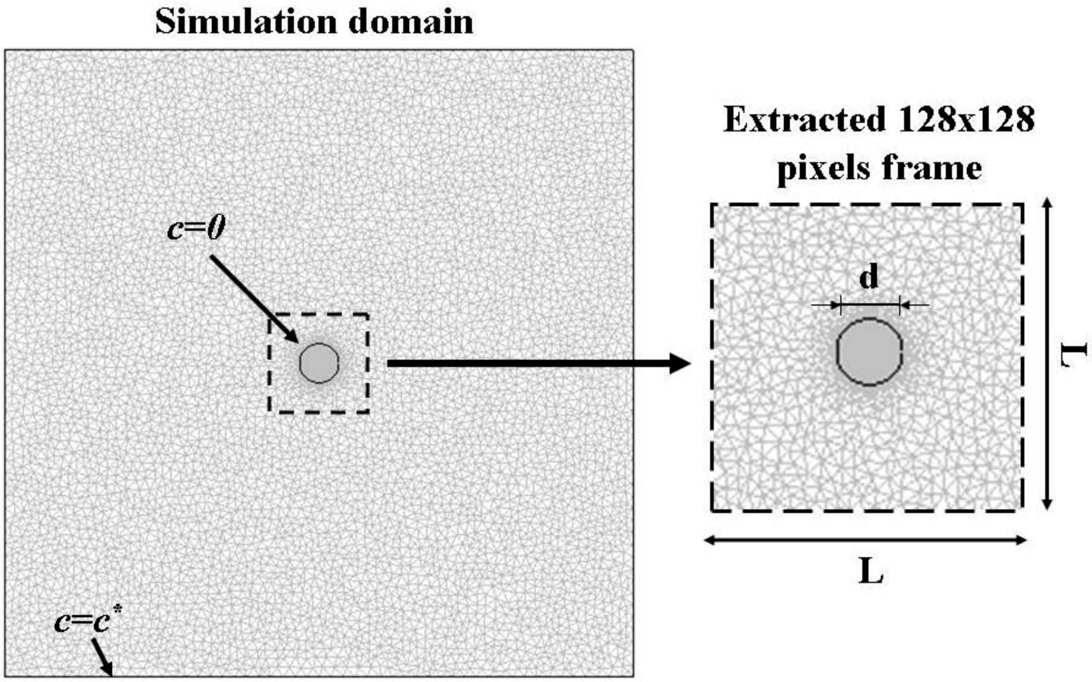

Figure 3.6 Mesh and size of the computational domain. The initial and boundary conditions are shown. For data analysis purposes, images of of 500x500 μm^2 (128x128 pixel) are extracted from the simulation domain (4x4 mm^2).[194]

Finally, the effect of the experimental noise on the accuracy of the data analysis was investigated by adding photon noise to the simulated FRAP images. Photon noise is characterized by a Poisson distribution. When photon emission is large (for instance, in a FRAP experiment) Gaussian noise can approximate Poisson noise.[11;195] Therefore, similarly to previous studies,[195;213] Gaussian noise was added to computer-generated FRAP images in order to simulate photon noise. The magnitude of the Gaussian noise was characterized by its standard deviation, σ. Two magnitudes of spatial Gaussian noise, generated by ImageJ software (Version 1.39f, by Wayne Rasband, National Institutes of Health, USA), were added to the simulated sequences of images, namely $\sigma = 5$ and 10. For each level of σ investigated, ten FRAP experiments (n=10) were simulated.

	Frequency couples (*u*,*v*)													
Ring 2	(2,0)	(2,1)	(1,2)	(0,2)										
Ring 3	(3,0)	(3,1)	(2,2)	(1,3)	(0,3)									
Ring 4	(4,0)	(4,1)	(4,2)	(3,2)	(3,3)	(2,3)	(2,4)	(1,4)	(0,4)					
Ring 5	(5,0)	(5,1)	(5,2)	(5,3)	(4,3)	(4,4)	(3,4)	(3,5)	(2,5)	(1,5)	(0,5)			
Ring 6	(6,0)	(6,1)	(6,2)	(6,3)	(6,4)	(5,4)	(5,5)	(4,5)	(4,6)	(3,6)	(2,6)	(2,6)	(1,6)	(0,6)

Table 3.1 List of the frequency couples (u,v) for different frequency rings ($0 \leq \alpha \leq \pi/2$).[194]

3.4.2 FRAP test on bovine AF

The experimental data on FRAP experiments on bovine coccygeal disc were obtained from a previous study.[192] Briefly, twelve AF specimens (5 mm diameter and 540 μm thickness) were harvested circumferentially from nine bovine discs (S2-3 and S3-4) belonging to 6-12 months old calves, see Figure 3.7a. During equilibration in a 0.1 mol/m^3 fluorescein (332 Da, $\leq_{ex}$ 490 nm; $\leq_{em}$ 514 nm, Fluka-Sigma-Aldrich®, St. Louis, Mo, USA) water solution, AF specimens were confined between two sintered stainless steel plates (20 μm porosity) and an impermeable spacer in order to prevent swelling. A total of 48 tests (n=48) were performed at room temperature (22°C) using a confocal laser scanning microscope (LSM 510 Zeiss, Jena, Germany). Since multiple testing was performed on each sample, in order to prevent tissue dehydration during experiments, specimens were moistened after each test. It should be pointed out that multiple tests were performed in different regions of the tissue, so that each FRAP experiment was not influenced by the fluorescence recovery of the previous test. Bovine specimens were photobleached using a 25mW argon laser (488nm wave length) at 70% laser power and 100% transmission. A Plan-Neofluar 20X/0.50 WD 2.0 objective (Zeiss, Jena, Germany) and 86 μm pinhole were used to generate images of 128x128 pixels (460.7x460.7 μm^2). For each test 200 frames, five of them before MLB the sample (see section 3.4.4 for details), were collected at 70% laser power and 2% transmission. The time delay between two consecutive frames was 0.1 seconds.

3.4.3 FRAP tests on bovine meniscus

Three bovine menisci, from 6-12 months old calves, were harvested. Cylindrical blocks, from all the regions of the tissue, were excised along the transverse direction of the tissue by a 5 mm diameter trephine. Menisci blocks were equilibrated in a fluorescein-water solution (0.1 mol/m^3) for 24 hours. From the central main layers [160] of each excised block, cylindrical specimens (5 mm diameter and 30 μm thickness) were prepared using a microtome (SM24000, Leica Microsystems GmbH, Wetzlar, Germany) with a freezing stage (Model BFS-30, Physitemp, Clifton, NJ), see Figure 3.7b. A total of 48 FRAP tests (*n=48*) were performed on twenty menisci specimens. The experimental protocol used in these tests was the same as that adopted for bovine disc. However, a different MLB protocol was performed (see section 3.4.4 for details).

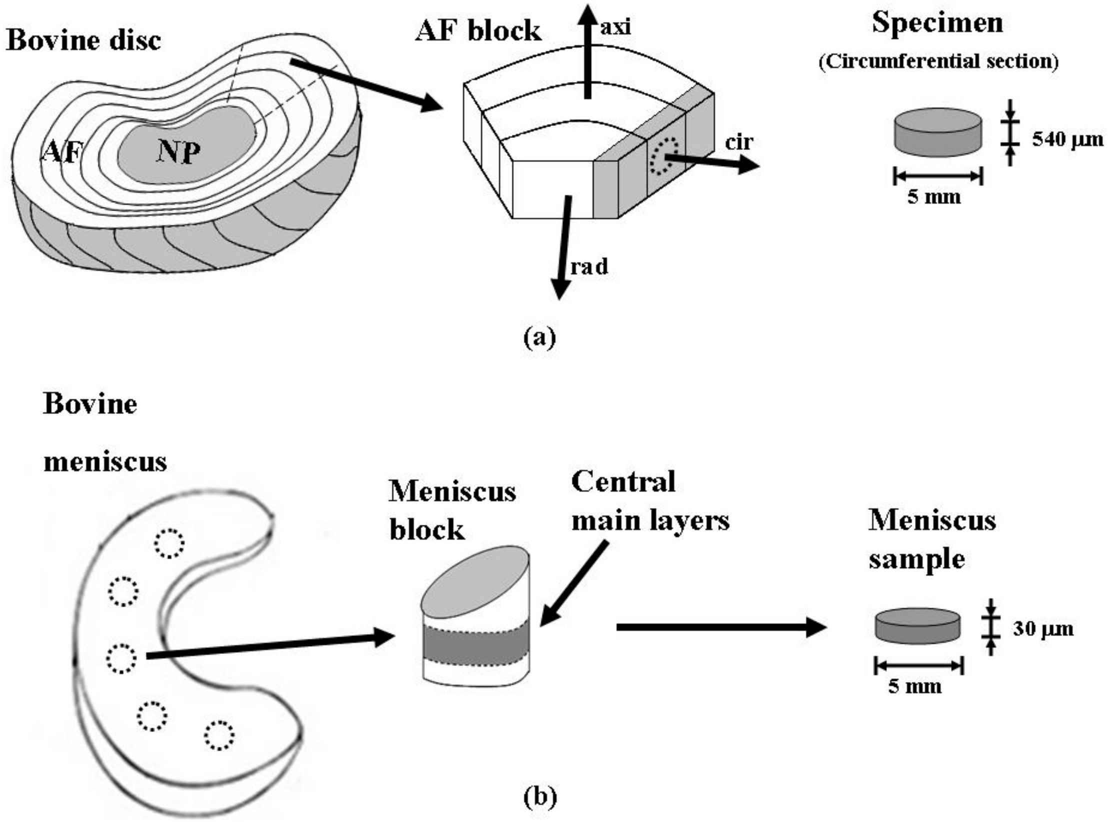

Figure 3.7 Schematic of specimen preparation for bovine AF (a), and bovine meniscus (b). The size and orientation of the specimens are shown.[194]

3.4.4 MLB protocols

Multi-layer bleaching was used in order to minimize the diffusive flux in the *z*-direction (orthogonal to the focal plane of the microscope objective). Depending on the nature of the sample (annulus fibrosus or meniscus), a different number of layers was sequentially bleached. The magnitude of the bleached volume generated after MLB was observed by acquiring a stack of images of the sample in the *z*-direction immediately after bleaching. Given the light intensity distribution, numerical simulations of three-dimensional (3D) fluorescent recovery were performed using COMSOL® software in order to determine the overestimation of the diffusion coefficients by using a 2D FFT approach. More in specific, numerical simulations were performed using ~35000 quadratic Lagrange tetrahedral elements. From each simulation a time series of 200 frames, representing the images on the focal plane of the microscope objective were extracted and analyzed by custom-made software performing FFT (see section 3.4.5).

For bovine AF specimens, four different layers of the sample were sequentially bleached. The distance between the bottom glass slide (see Figure 3.3) and the focal plane of the microscope objective, where fluorescence recovery was observed, was 7 μm and the diameter of the bleach spot was 28.75 μm. The other bleach spots were produced in layers at 17, 27 and 32 μm from the bottom of the sample and their diameters were 43.12, 50.31 and 71.88 μm, respectively. The bleached spots were produced from top to bottom. Measurements of fluorescence intensity within the sample indicated that, after bleaching the four layers in the sample, the final shape of the bleached region is a cylinder of approximately 28 μm diameter and 47 μm height. In particular, within the bleached volume, three regions were identified (measured from the bottom glass slide): (1) from 0 to 17 μm, the fluorescence was completely depleted; (2) from 17 to 27 μm, the fluorescence linearly increased (i.e., recovered) to 50% of the intensity of the surrounding unbleached tissue (I_o); (3) from 27 μm to 47 μm, the fluorescence intensity was approximately 50% of the value of I_o. Numerical simulations demonstrated that in these conditions the highest relative error (in the case $D_\alpha/D=2$) committed in the determination of tr($\boldsymbol{D}$) using a 2D FFT approach is estimated to be approximately 18%.

For tests on bovine meniscus, due to the thickness of the samples (30 μm), only two layers of the cylindrical specimens were sequentially bleached. More in specific, the radii of the circular bleached spots produced were 28.75 μm and their distances from the surface of the cover glass were 7μm and 17μm, respectively. Fluorescence recovery was observed on the focal plane of the lower bleached spot (at 7 μm). Some of the profiles of the normalized fluorescence intensity distribution at different layers of the tissue are shown in Figure 3.5 Given this light intensity distribution, numerical simulations indicated that the overestimation of $tr(\boldsymbol{D})$ was below 10%.

3.4.5 Data analysis

Both numerical and experimental fluorescence recovery data were analyzed by a custom-made, MATLAB-based algorithm (MATLAB® 6.5, The MathWorks Inc., Natick, MA) performing fast Fourier transform (FFT) and KLT to yield tr($\boldsymbol{D}$), D_{xy}, and θ used in Equations (3.13-14). The value of the angle θ was determined by KLT analysis of the bleached spot in the recovered images. For computer-simulated FRAP experiments (i.e., ideal cases), only one image showing a fully developed elliptical (bleached) spot was used for determining θ. Around the bleached spot, any pixels with light intensity of 10% lower than the average intensity of image background were considered belonging to the bleached spot and chosen as data points $\boldsymbol{P}_i$ for the KLT analysis, see Figure 3.2. For experimental images and for computer-generated images contaminated by noise, θ was determined by averaging its values determined by KLT over five post-bleaching images, namely the 10th, 20th, 30th, 40th, and 50th frames after bleaching.

3.4.6 Statistical analysis

A paired *t*-test was performed using Excel Spreadsheet software (Microsoft® Office Excel 2003, Microsoft Corp., Seattle, WA) in order to determine if a statistically significant difference existed between the two principal components of the diffusion tensors of fluorescein in both bovine AF and meniscus. For all tests, the significance level was set at $P<0.05$. All data are given in mean ± standard deviation.

3.5 Results

3.5.1 Numerical validation

FRAP experiments were numerically simulated by inputting the components of $\boldsymbol{D}$, and subsequently analyzed by FFT and KLT to output the values of the same quantities. The accuracy of the method was assessed by the relative error (ε), defined as:

$$\varepsilon = 100 \cdot \frac{|Input - Output|}{Input} \ (\%). \quad (3.16)$$

The ratio of the frame size (L) to the initial diameter (d) of the bleached spot significantly affected the accuracy in determining the value of $tr(\boldsymbol{D})$, see Figure 3.8. For all the cases investigated, it was found that the optimal ratio of the frame size to the size of the bleached spot was L/d=8. It should be noted that the data reported in Figure 3.8 were obtained integrating Equations (3.9) and (3.15) over only one set of frequencies, namely ‘Ring 4’. Similar results were also found when other frequency rings, ranging from ‘Ring 3’ to ‘Ring 10’, were used, see Figure 3.9. Therefore, for all the other numerical and experimental analyses carried out in the study, the ratio L/d=8 was used.

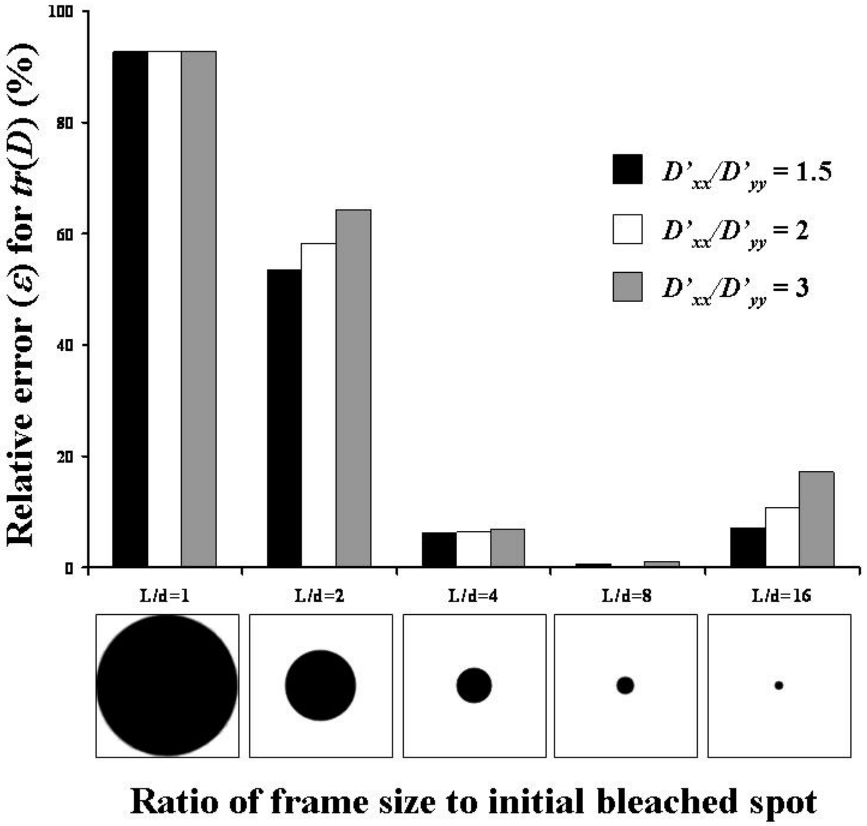

Figure 3.8 Effect of the ratio of frame size (L) to bleached spot diameter (d) on the relative error (ε) for the determination of $tr(\mathbf{D})$. Data were analyzed at frequency 'Ring 4'. For all the cases reported in this figure, $D'_{xx} = 10^{-7}$ cm^{2}s^{-1}, and $\theta = 45°$.[194]

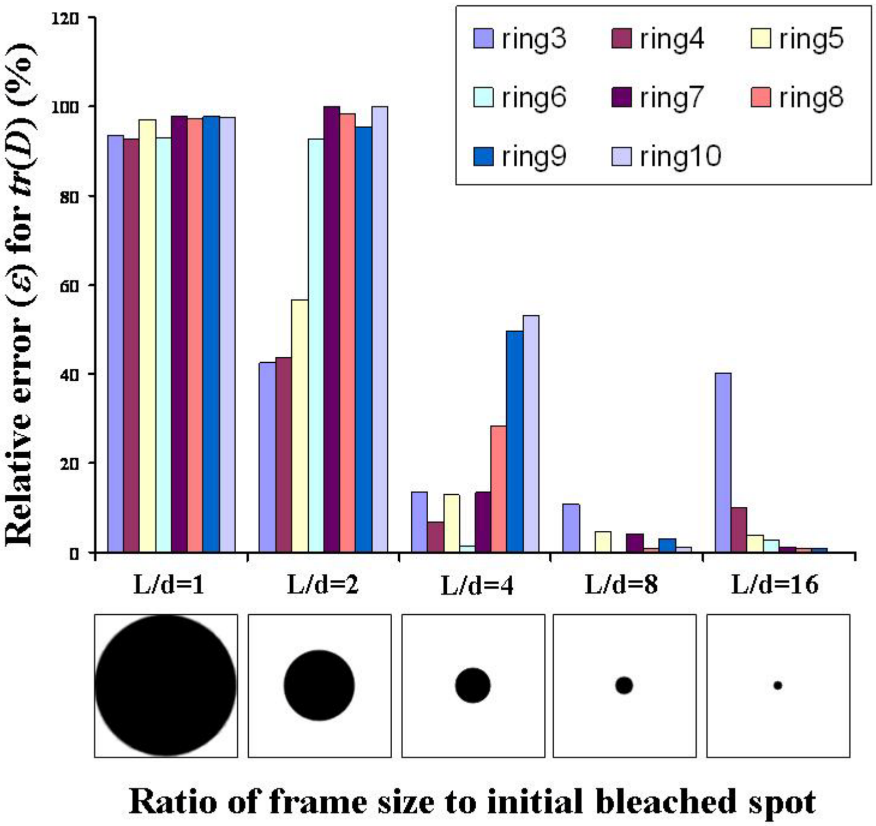

Figure 3.9 Effect of the ratio of frame size (L) to bleached spot diameter (d) on the relative error (ε) for the determination of $tr(\mathbf{D})$. Data were analyzed at frequency rings raging from ‘Ring 3’ to ‘Ring 10’. For all the cases reported in this figure, $D'_{xx} = 10^{-7}$ cm^{2}s^{-1}, $D'_{xx}/D'_{xx} = 2$, and $\theta = 45°$.

The accuracy for the calculation of ***D*** was also affected by the choice of the frequency ring used in integration of Equations (3.9) and (3.15). For the ideal cases investigated (i.e., noise free images), ‘Ring 6’ provided the smallest relative error in the determination of $tr(\mathbf{D})$, see Figure 3.10. However, ‘Ring 6’ might not be optimal for analyzing non-ideal images from real experiments (see below). It should be noted that ‘Ring 4’ was the second best choice, providing a relative error (ε) below 2% for all the cases investigated (see Figure 3.9). Therefore, ‘Ring 4’ was used in the all following analyses.

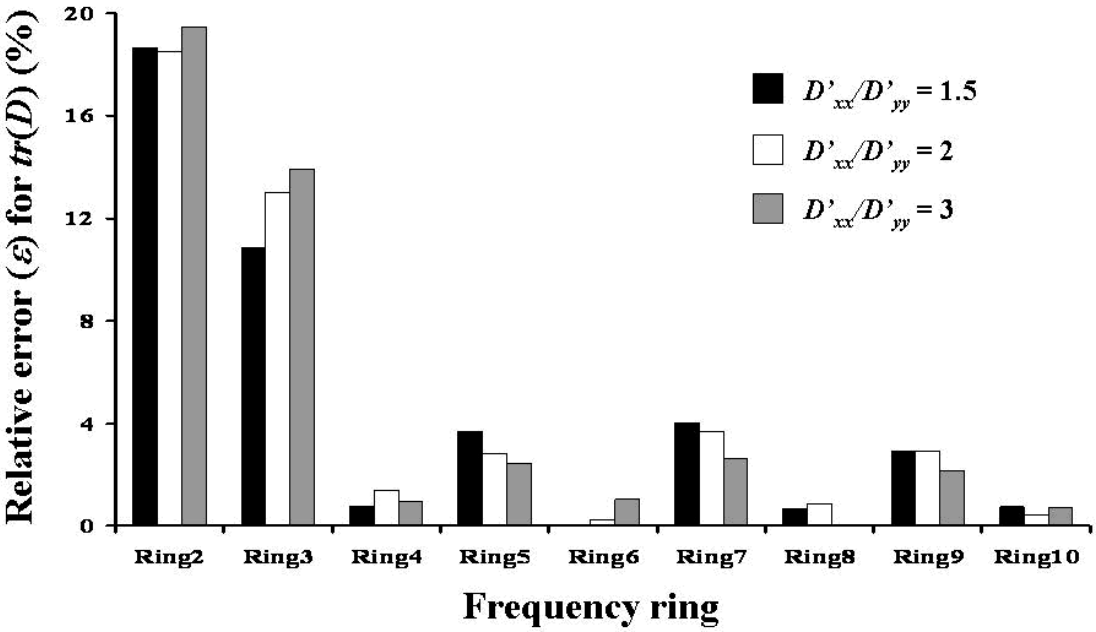

Figure 3.10 Effect of the frequency ring on the relative error (ε) for the determination of $tr(\mathbf{D})$. For all the cases reported in this figure, L/d=8, $D'_{xx} = 10^{-7}$ cm^{2}s^{-1}, and $\theta = 45°$.[194].

The accuracy in determining the components of $\boldsymbol{D}$ at different orientations (θ) was investigated. Figures 3.11 and 3.12 report ε for the determination of D'_{xx} and D'_{yy} for three different anisotropic ratios: D'_{xx}/D'_{yy} = 1.5, 2, and 3, respectively (with $D'_{xx} = 10^{-7}$ cm^{2}s^{-1}). The accuracy of the method was not sensitive to θ, and increased when the anisotropic ratio D'_{xx}/D'_{yy} reduces (for most θs investigated). However, when θ=0° or θ=90° Equation (3.14) is not applicable. For these two special cases the components D'_{xx} and D'_{yy} were extracted directly from Equation (3.6) by choosing special couples of frequencies at ($u=4$, $v=0$; i.e., $\xi=0$) and ($u=0$, $v=4$; i.e., $\xi=\pi/2$), respectively, as proposed by Tsay and Jacobson.[195]

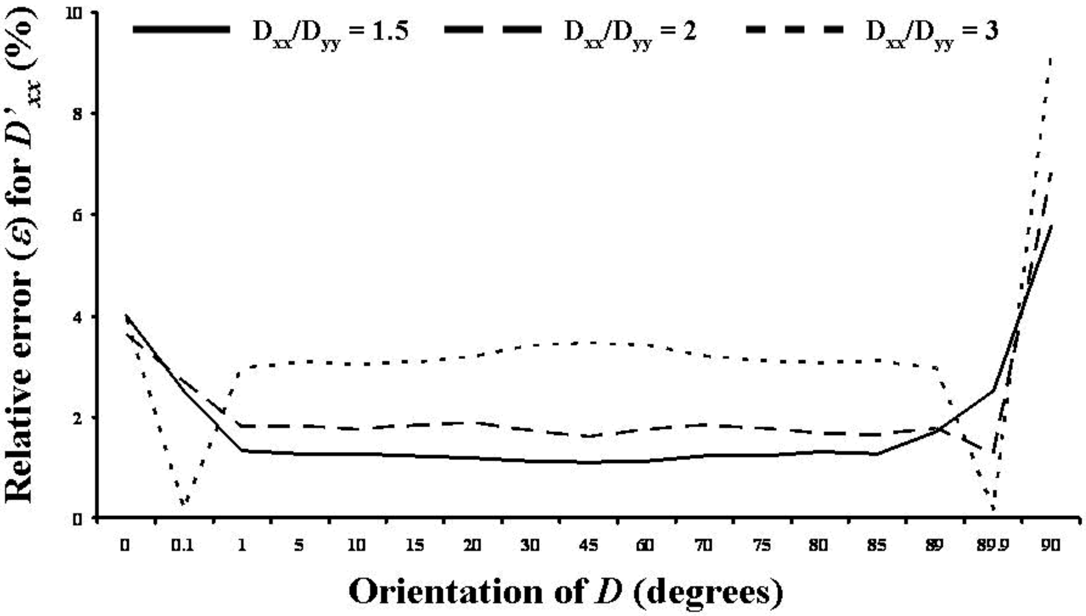

Figure 3.11 Effect of the orientation of the diffusion tensor on the relative error (ε) in the determination of D'_{xx}. In all the cases reported in this figure $D'_{xx} = 10^{-7}$ cm^{2}s^{-1}.[194]

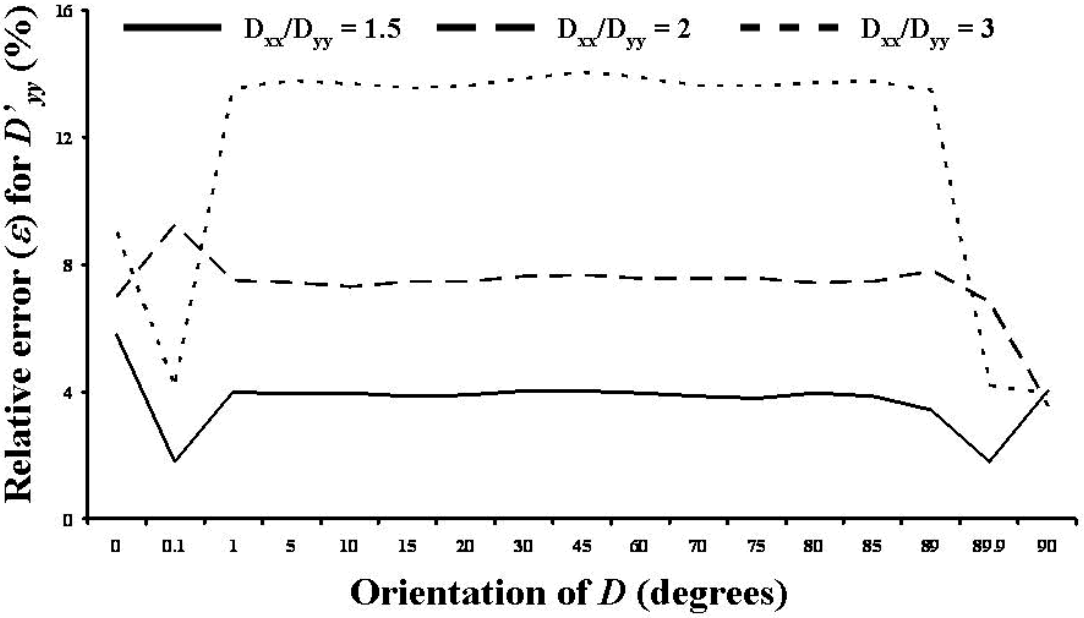

Figure 3.12 Effect of the orientation of the diffusion tensor on the relative error (ε) in the determination of D'_{yy}. In all the cases reported in this figure $D'_{xx} = 10^{-7}$ cm^{2}s^{-1}.[194]

In real video-RFAP images, the estimation of θ by KLT may be affected by the quality of the image obtained (see Section 3.6). The sensitivity of the precision of the method to the error in the determination of θ was numerically investigated for a representative case where $D'_{xx}/D'_{yy} = 1.5$ (with $D'_{xx} = 10^{-7}$ cm^{2}s^{-1}). Figure 3.13 reports ε in determining D'_{xx} if the estimation of θ by KLT is affected by an error of ±5°. The value of ε is less than 6% for the worst cases considered (for $\theta = 15°$ or 75°).

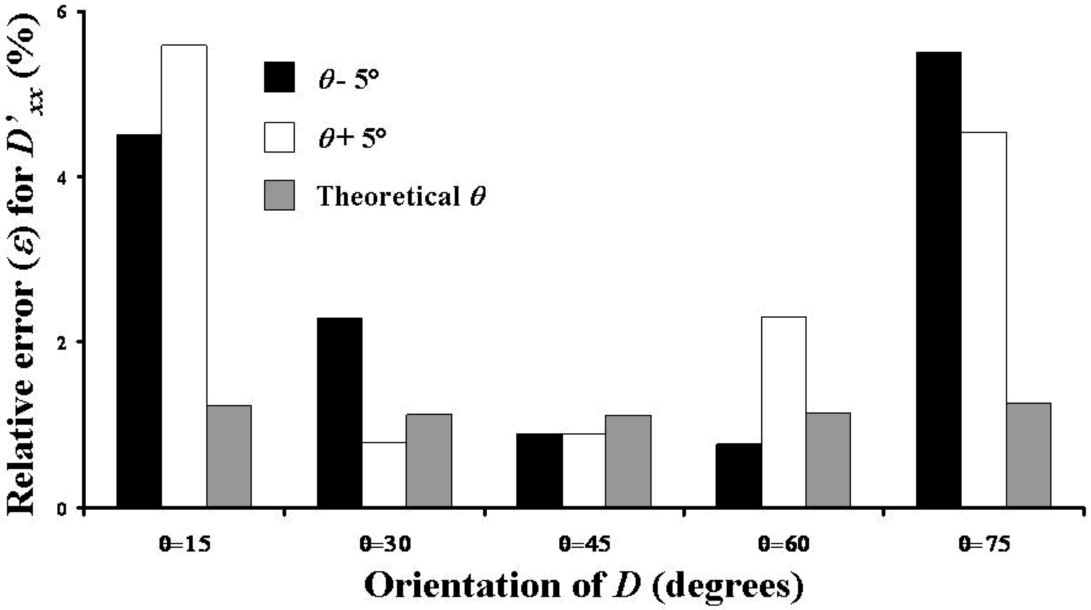

Figure 3.13 Effect of the precision (±5°) in determining the tensor orientation (θ) by KLT on the relative error (ε) for the determination of D'_{xx}. In this case, $D'_{xx}/D'_{yy} = 1.5$ with $D'_{xx} = 10^{-7}$ cm^{2}s^{-1}.[194]

The sensitivity of the method to noise contamination was studied. Gaussian noise was added to images produced at $D'_{xx}/D'_{yy} = 1.5$ and $\theta = 45°$, with D'_{xx} ranging from 10^{-8} to 10^{-6} cm^{2}s^{-1}. Figure 3.14 compares ε in the determination of D'_{xx} and D'_{yy} for an ideal case (σ = 0) and for the cases with noise (σ = 5 and 10). The value of ε increased with increasing σ. Additionally, the effect of noise was also investigated when different frequency rings are used in integration of Equations (3.9) and (3.14). As expected, the accuracy of the method decreases as the magnitude of the noise increases, see Figure 3.15. However, while for ideal case (noise free image) 'Ring 6' represents the best choice (see also Figure 3.10), as the noise increases, 'Ring 4' provides the most accurate results.

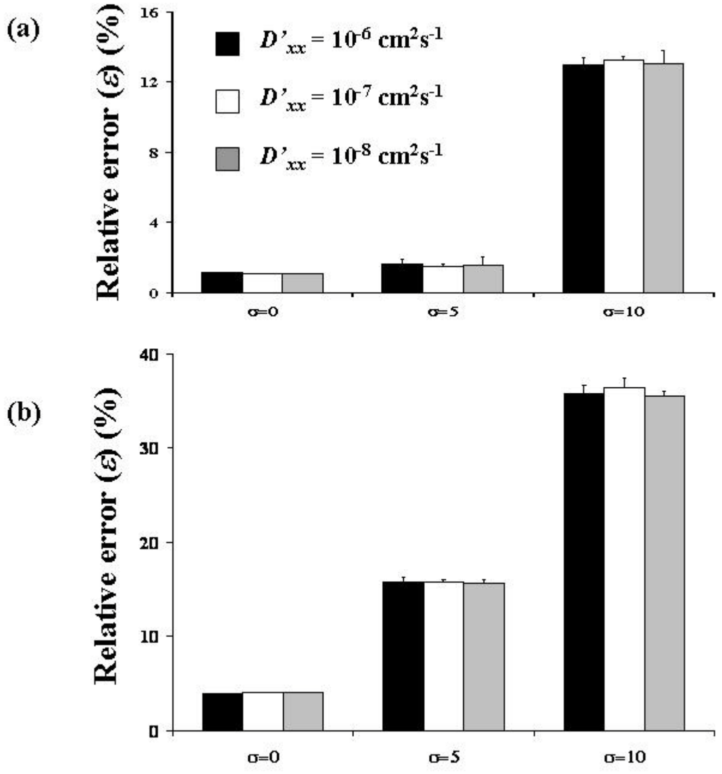

Figure 3.14 Sensitivity of the results to Gaussian noise magnitude (σ) at different magnitude of diffusivity. Data reported at $\sigma = 0$ refer to noise free simulated FRAP experiments. (a) relative error (ε) for D'_{xx} and (b) relative error for D'_{yy}. For all the cases reported in this figure, $D'_{xx}/D'_{yy} = 1.5$ and $\theta = 45°$.[194]

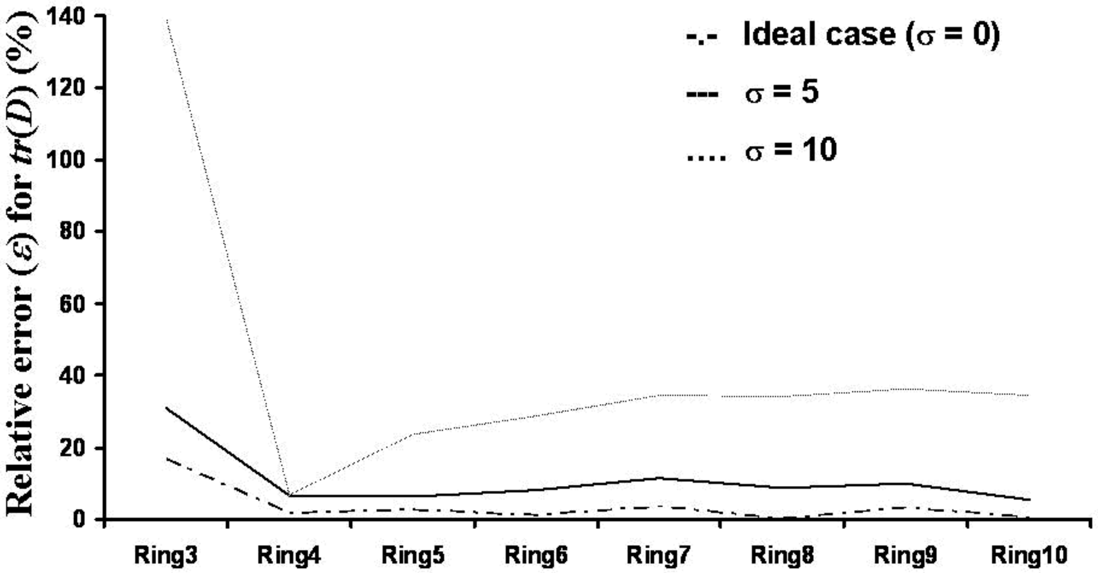

Figure 3.15 Effect of the frequency ring on the relative error (ε) for the determination of $tr(\mathbf{D})$, parametric with noise magnitude σ. Data reported at $\sigma = 0$ refer to noise free simulated FRAP experiments. For all the cases reported in this figure, $D'_{xx} = 10^{-7}$ cm^{2}s^{-1}, $D'_{xx} / D'_{yy} = 2$, and $\theta = 45°$.[191]

3.5.2 Experimental validation

The experimental validation of the new technique was carried out by analyzing FRAP experiments performed on bovine AF. The results were compared to those reported in a previous study.[192] Results indicated that the principal components of the diffusion tensor (D'_{xx} and D'_{yy}) were statistically different ($P<0.05$). In particular, the values of D'_{xx} and D'_{yy} were $1.24\pm0.383\text{x}10^{-6}$ cm^{2}s^{-1} and $0.964\pm0.283\text{x}10^{-6}$ cm^{2}s^{-1} (mean±SD, $n=48$), respectively. Additionally, analysis of video-FRAP images suggested that the directions of D'_{xx} and D'_{yy} coincide with the axial and radial directions of the disc, respectively (see section 3.6). Moreover, the values of D'_{xx} and D'_{yy} were consistent to those in the axial direction (D_{axi}=$1.26\text{x}10^{-6}$ cm^{2}s^{-1}) and in the radial direction

(D_{rad}=0.814x10^{-6} cm^{2}s^{-1}) determined by a different approach reported in a previous study.[192]

3.5.3 Measurements of diffusion coefficients in bovine meniscus

The difference between the two principal components of ***D*** was significant (t-test, $P<0.05$), indicating that fluorescein diffusion in bovine meniscus is anisotropic. In particular, the principal diffusion coefficients of fluorescein in the tissue were: D'_{xx} = 1.59±0.56x10^{-6} cm^{2}s^{-1} and D'_{yy} = 0.44±0.28 x10^{-6} cm^{2}s^{-1} (mean±SD, $n=48$). In addition, analysis of the orientation of the bleached spot in video-FRAP images suggested that the two principal directions of the diffusion tensor were parallel and orthogonal to the orientation of the collagen fibers in the tissue (see Section 3.6).

3.6 Discussion

The new technique hereby presented is based on two independent analyses of video-FRAP images: KLT analysis of the shape of the bleached sport to yield the orientation (θ) of ***D***, and Fourier analysis of light intensity decay of the images to yield $tr(\mathbf{D})$ and D_{xy}. The combination of the results produced by these two analyses provides the 2D diffusion tensor in a single FRAP experiment.

The new method presented in this study was validated by both computer simulated and experimental FRAP tests. The experimental validation of the technique was performed by determining the principal components of ***D*** of fluorescein in bovine AF. The results were compared with those reported in a previous study.[192] The values of diffusion coefficients estimated in this study were consistent with those determined by

Travascio and Gu (2007),[192] see Section 3.5.2. Note that, in the approach presented by Travascio and Gu (2007), the principal components of ***D*** were determined by the Fourier analysis of the FRAP images from each of the orthogonal sections of a tissue sample,[192] see Section 3.2.1.2 for details. In the current method, however, the orientation of bleached spot was also analyzed to yield the orientation of a diffusion tensor. This allowed to completely determine an anisotropic (2D) tensor using a single FRAP test. Additionally, the new technique was applied to the characterization of the diffusion tensor of fluorescein in bovine meniscus. Results indicate that fluorescein diffusion in bovine meniscus is anisotropic, with D'_{xx} being 3x of D'_{yy}. These results are consistent with similar findings reported for anisotropic diffusion in ligaments.[119]

The use of an imaging technique such as KLT allowed to associate solute diffusivities to the structure of the tissue. Results from KLT analysis on both AF and meniscus samples suggested that the orientation (θ) of the largest principal component of ***D*** is parallel to the direction of the bundles of collagen fibers within the tissues, see Figure 3.16a-b. Since in the circumferential section of bovine AF sample the collagen fibers are oriented in the axial direction, these findings indicate that the directions of D'_{xx} and D'_{yy} coincide with the axial and radial directions of the disc, respectively. Similarly, in bovine meniscus, the orientations of D'_{xx} and D'_{yy} are parallel and perpendicular to the collagen fibers in the tissue, respectively.

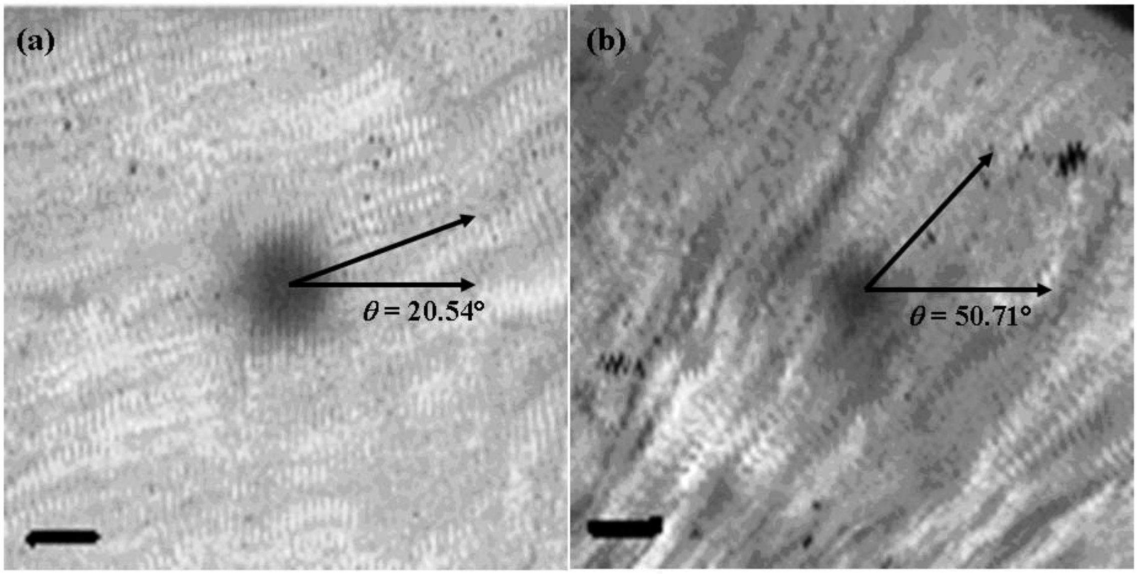

Figure 3.16 Confocal laser scanning recovery images (128x128 pixel, 460.7x460.7 μm^2) of FRAP experiments on bovine AF (a) and bovine meniscus (b). The orientations of the bleached spots estimated by KLT are shown.[194]

Numerical simulation of FRAP experiments were used to assess the accuracy and the robustness of the technique. The results showed that, for all the anisotropic cases reported, the accuracy of the new method was not sensitive to the orientation of $\boldsymbol{D}$, see Figures 3.11 and 3.12. However, it should be noted that this technique is not applicable when the orientation of $\boldsymbol{D}$ coincides with the fixed coordinate system (for $\theta = 0°$ or $90°$). For these two special cases, the method proposed by Tsay and Jacobson[195] can be used, see Section 3.2.1.2. Alternatively, one could rotate the specimen and repeat the FRAP experiment in order to avoid these special cases.

Numerical simulations also provided guidelines for optimizing the choice of parameters in performing experiments and data analysis. The results showed that the relative size of the bleached spot (*L/d*) as well as the 'frequency ring' significantly affected the accuracy of the method for the determination of $\boldsymbol{D}$. For the set of diffusion coefficients explored in the numerical analysis carried out in this study, there existed an optimal size for the initially bleached spot relative to the size of the image frame (i.e., at $L/d = 8$), see Figures 3.8 and 3.9. For the choice of frequency rings in the FFT analysis, although 'Ring 6' provided the most accurate results for ideal (noise free) FRAP images (see Figure 3.10), 'Ring 4' proved to be the best when images contaminated by noise were analyzed, see Figure 3.15. Therefore, in the analyses of simulated and real FRAP experiments, 'Ring 4' was used. In general, the higher the frequency ring, the more data points of $D(\xi)$ could be used to evaluate D_{av} and D^{+}_{av} in Equations 3.9 and 3.15, see Table 3.1. However, the use of higher frequency rings would increase the cost of data analysis and may not necessarily improve the accuracy of the results for ideal images (see Figure 3.10) or images contaminated by noise (see Figure 3.15). This could be attributed to the fact that the determination of $D(\xi)$ occurs via curve-fitting of light intensity decay in the Fourier space (see Equation 3.6). Theoretically, the determination of $D(\xi)$ should not depend on the frequency ring. However, in reality, when high frequency rings are used, the curve-fitted values of $D(\xi)$ may not be accurate since the light intensity decays much faster at higher frequencies due to the exponential term in Equation 3.6. A similar observation was also reported by Jönsson et al. (2008).[101] It should be noted that, in a previous study, Tsay and Jacobson (1991) also investigated the coupled effect of spot size and frequency rings (up to 'Ring 3') on the accuracy of FFT analysis of numerically simulated FRAP images (64x64 pixel). It was found that the 'Ring 2' was the optimal frequency ring for the images with spot size of L/d=4.[195] In Figure 3.17 the effect of spot size (L/d= 4 vs. L/d=8) on the accuracy in determining $tr(\boldsymbol{D})$ were compared at different frequency rings. Consistently with the findings reported by Tsay and Jacobson (1991), the ratio *L/d*=8 provided the highest accuracy for all cases investigated, except at 'Ring 2'. In contrast, when *L/d*=4 was used, frequency 'Ring 2' provided higher accuracy than 'Ring 3' or 'Ring 4'.

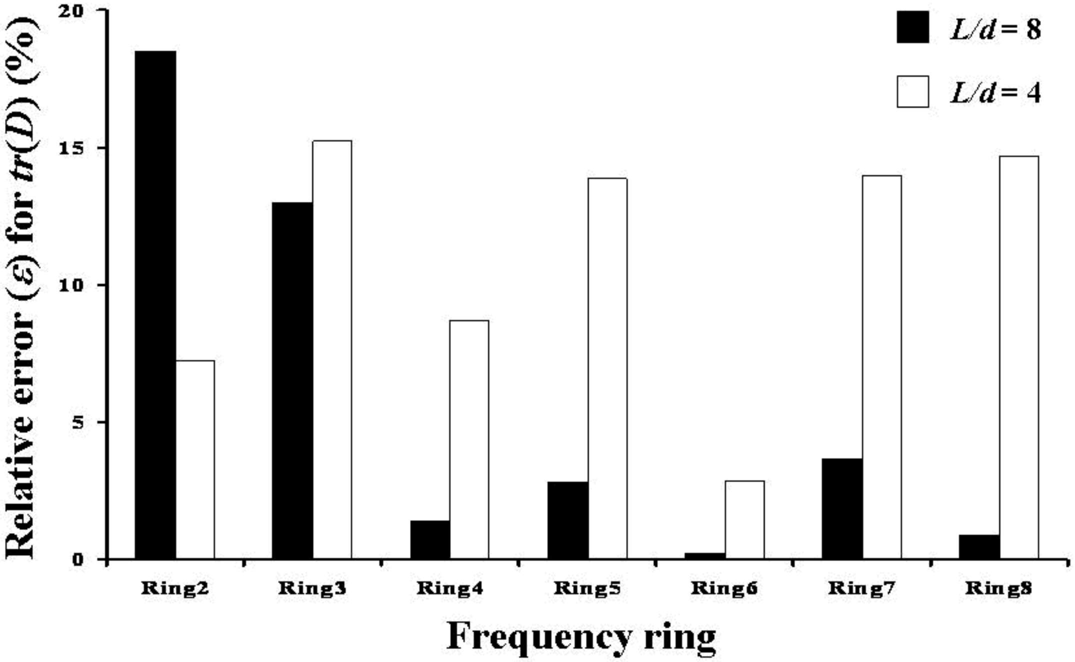

Figure 3.17 Comparison of the relative error (ε) in determining $tr(\mathbf{D})$ using different frequency rings for two different spot sizes: *L/d*=8 (black) and *L/d*=4 (white). For all the cases reported in this figure $D'_{xx}/D'_{yy} = 2$ (with $D'_{xx} = 10^{-7}$ cm^{2}s^{-1}), and $\theta = 45°$.[194]

The determination of θ is based on the analysis of the shape of the fully developed elliptical bleached spot during the recovery phase. In a real FRAP experiment, the presence of noise or artifacts can affect the definition of the contour of the bleached spot. Thus, in the same FRAP experiment, the calculated orientation of the spot may vary from one image frame to another, see Figure 3.17.

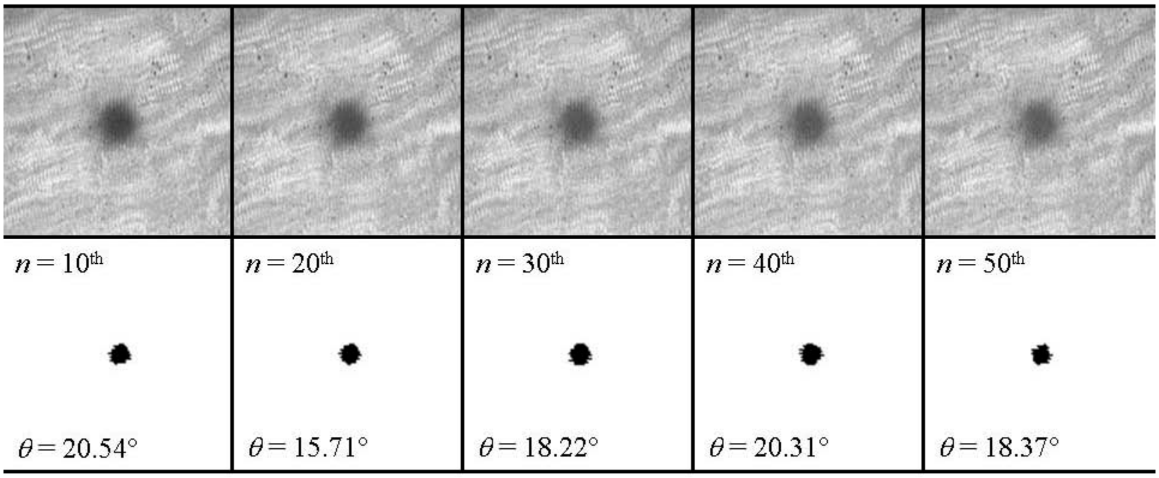

Figure 3.18 Determination of θ by KLT. During each FRAP experiment, the 10th, the 20th, the 30th, the 40th, and the 50th video-FRAP images are analyzed to determine the orientation of the bleached spot. The average of the five measurements provides the final value of θ.

In this study, the determination of θ was performed by averaging five values of the orientation of the bleached spot, determined in different video-FRAP images, see Section 3.4.5. Table 3.2 reports some of the measurements of θ performed on bovine meniscus samples. It can be observed that the range of variation of θ from one image to the other is never larger than 5%. Numerical simulations performed in this study showed that, when the estimation of θ by KLT is affected by an error of ±5°, the relative error for the determination of D'_{xx} is less than 6%, see Figure 3.13. In order to reduce the artifacts produced by noise, the image series could be post-processed by using a multi-scale active shape model for the contour detection of the bleached spot.[128]

Some limitations of the new method deserve to be discussed. The light intensity of images acquired by a laser scanning microscope tends to decrease with time, due to photobleaching of the background fluorescence. In addition, because of the presence of noise, temporal fluctuations of light intensity can occur. The method presented in this study does not include compensations for these two sources of error. Techniques of image post processing could be used in order to compensate the background decay and the temporal fluctuation of the light intensity.[57;101] In order to reduce the sources of experimental error for improving the accuracy of the results, the application of image post processing techniques should be considered.

	Frame 10	Frame 20	Frame 30	Frame 40	Frame 50	Average±SD
Sample 1	80.7°	80.44°	79.95°	82.24°	87.63°	82.19°±3.16°
Sample 2	74.71°	74.64°	72.03°	70.06°	72.09°	72.71°±1.97°
Sample 3	82.64°	85.62°	87.02°	87.88°	83.54°	85.34°±2.23°
Sample 4	55.79°	52.53°	51.41°	50.91°	52.96°	52.72°±1.9°
Sample 5	18.75°	14.24°	15.55°	18.24°	19.94°	17.34°±2.37°

Table 3.2. Determination of θ at different time points for fluorescein diffusion in bovine meniscus. Five randomly chosen samples were analyzed and reported.[194]

The sensitivity of the new method to the level of Gaussian noise was investigated, see Figure 3.14. The results indicate that the accuracy of the method is reduced when the noise level is increased. It would be desirable to determine the actual noise level in real FRAP experiments in order to provide a precise estimate of the accuracy in the determination of the diffusion coefficients. This aspect should be investigated.

3.7 Summary

In summary, a new FRAP technique for the determination of solute diffusivity in structurally anisotropic biological tissues has been presented. Using numerically simulated FRAP images, the accuracy of the method was investigated for different sizes of bleached spots and for different frequency rings. The effect of noise level on the data analysis was also investigated. The new method was validated using real FRAP experiments on bovine AF. Finally, the new technique was applied to the characterization of fluorescein diffusivity in bovine meniscus. Through image analysis, the orientation of the principal directions of the diffusion tensor (given by the shape and orientation of the bleached spot) was related to the structure of the tissue. Therefore, this technique can characterize the solute diffusion tensor in a single FRAP experiment and relate tissue morphology to its transport properties.

In Chapter 4, the present method is applied to the characterization of the diffusive properties of human lumbar annulus fibrosus, and the results produced will provide suggestions on the experimental parameters to be used in the finite element model for solute transport in cartilaginous tissues presented in Chapter 6.

Chapter 4: RELATIONSHIP AMONG SOLUTE TRANSPORT PROPERTIES, STRUCTURE AND COMPOSITION OF IVD

4.1 Introductory remarks

Insufficient nutritional supply has been associated with the degeneration of the intervertebral disc (IVD).[13;25;48;75;80;148;198;203] Being the largest avascular structure in human body, IVD receives nourishment from the surrounding vascular network,[24;74;80;133;148;153;168;205] see Figure 1.5. Diffusion is a major mechanism for nutrient transport within the disc.[131;199;200] From studies on both animal and human IVDs, it emerged that solute diffusion is anisotropic and inhomogeneous.[33;84;95;96;155;192] These two features of diffusive transport have been associated to the complex and unique structural organization of IVD, see Chapter 1. In particular, it has been speculated that the presence of microtubes (see Figure 1.2) has implications with the anisotropic diffusive transport properties of IVD.[96;192] In the past, the relationship between tissue morphology and anisotropic solute transport was investigated in cartilage,[111;117;214] ligaments,[119] and meniscus.[194] However, little is known about the relationship between solute diffusive transport and the unique structure of IVD. Knowledge of transport properties of solutes (e.g., oxygen and glucose) and their relation to tissue morphology is crucial for better understanding nutritional supply to IVD cells.

The focus of this chapter is to investigate on the implications of the complex IVD structure (e.g., microtubes) and composition on the inhomogeneous and anisotropic solute diffusivity in the human lumbar disc. Hereby, it is hypothesized that, for human lumbar AF tissue, (1) diffusion of solutes is anisotropic and inhomogeneous; and (2) transport properties are associated with tissue composition and structure. In order to test these hypotheses, diffusivity of fluorescein in human lumbar AF was determined using the FRAP technique developed in Chapter 3. Fluorescein was chosen as a solute due to its relatively small size (332 Da), making it comparable to important nutrients, such as glucose.

The anisotropic behavior of diffusive transport was investigated by measuring fluorescein diffusion coefficients in two directions (axial and radial), while its inhomogeneous behavior was studied by determining the diffusivities in three different regions of human AF: inner AF (IAF), middle AF (MAF), and outer AF (OAF). In order to investigate the relationship between solute diffusivity and tissue morphology and composition, the water content and the microtube density were measured in the three regions of AF. The density of microtubes in human tissue was determined from the analysis of AF images obtained using Scanning Electron Microscopy (SEM). Additionally, the images were also used to qualitatively examine the structure of the tissue and its implications for transport phenomena in the disc.

4.2 Methods

4.2.1 Specimen description

Human lumbar spines (*n*=3; 41, 45, and 45 y.o.) were obtained from cadavers within approximately 24 hours from death and stored at -80^{o}C until dissected. Information regarding disc donors is summarized in Table 4.1. On the day of dissection, spines were partially thawed, and three L3-L4 discs (one from each spine) were isolated. After dissection, discs were classified according to Thompson's morphologic grading scheme.[190] In particular, one disc (41 y.o.) was classified as grade I, another disc (45 y.o.) as grade II, and the third disc (45 y.o.) as grade III, see Figure 4.1.

Specimens were harvested from the inner AF (IAF), middle AF (MAF), and outer AF (OAF) of both anterior and posterior parts of three human IVDs, as illustrated in Figure 4.2a. Preliminary studies indicated that the values of diffusion coefficients in the anterior and posterior regions of the disc were not statistically different. Therefore, in statistical analysis, specimens belonging to the anterior and posterior regions of AF were combined in the same group. For diffusivity measurements, 7 IAF specimens, 8 MAF specimens, and 6 OAF specimens were harvested from each disc. Thus, the total number of specimens for IAF, MAF, and OAF regions was: 21, 24, and 18, respectively. For each region of the disc investigated, 36 FRAP experiments were performed (at least one test for each specimen). For water content measurement, a total of 8 specimens were harvested from each AF region (2-3 specimens each disc). In measuring the microtube area fraction, 4 specimens from each of the 3 regions were harvested from one disc (Grade III). On each specimen, 2-3 SEM images were taken. The total number of measurements was 10 for each of AF regions.

DEGENERATIVE GRADE	AGE	GENDER	CAUSE OF DEATH
I	41	M	Hemorrhagic stroke
II	45	F	Schizophrenia
III	45	F	Mixed drug intoxication

Table 4.1. Age, gender, and cause of death for patients from whom discs were obtained during autopsy.

4.2.2 Measurement of diffusivity

Measurements of fluorescence diffusivity in human AF were performed by FRAP, see Chapter 3. Circumferential sections of AF specimens (area of ~30 mm^2 and thickness of 500 μm) were prepared using a microtome (SM24000, Leica Microsystems GmbH, Wetzlar, Germany) with a freezing stage (Model BFS-30, Physitemp, Clifton, NJ). Prior to testing, the specimens were equilibrated in a phosphate buffered saline (PBS) solution (Sigma®, St. Louis, MO, USA) with 0.1 mol/m^3 fluorescein (332 Da, λ_{ex} 490 *nm*; λ_{em} 514 *nm*, Fluka-Sigma-Aldrich®, St. Louis, MO, USA) while confined between two sinterized stainless steel plates (20 μm average pore size, Mott Corp., Farmington, CT) and an impermeable spacer, in order to prevent tissue swelling,[192] see Figure 4.2b.

In these tests, the protocols of experimental testing and image post-processing were similar to those reported in Chapter 3 for experiments on bovine coccygeal annulus fibrosus (see Section 3.4.2, 3.4.4, and 3.4.5). Data analysis of video-FRAP image series provided the fluorescein diffusion coefficients along axial (D_{axi}) and radial (D_{rad}) directions of the disc.

4.2.3 Measurement of water content

In this study, the water content of the tissue was expressed in terms of water volume fraction (ϕ^w), see definition in Chapter 2. The measurement of water content was performed using the Archimedes' principle. Briefly, tissue samples were first weighed in air (W_{wet}), and then in PBS bathing solution (W_s) using the density determination kit together with a Sartorius analytical balance (Model LA120S, Goettingen, Germany). In order to minimize tissue swelling while weighting in PBS, measurements of W_s performed in less than 15 seconds.[59;60;95;220] Finally, specimens were lyophilized and their dry weight (W_{dry}) was measured. Thus, the water volume fraction was calculated by:[59]

$$\phi^w = \frac{(W_{wet} - W_{dry})\rho_s}{(W_{wet} - W_s)\rho_w}, \qquad (4.1)$$

where ρ_s and ρ_w are the densities of PBS solution and water, respectively. Measurements of water content were performed on samples belonging to the three regions of AF.

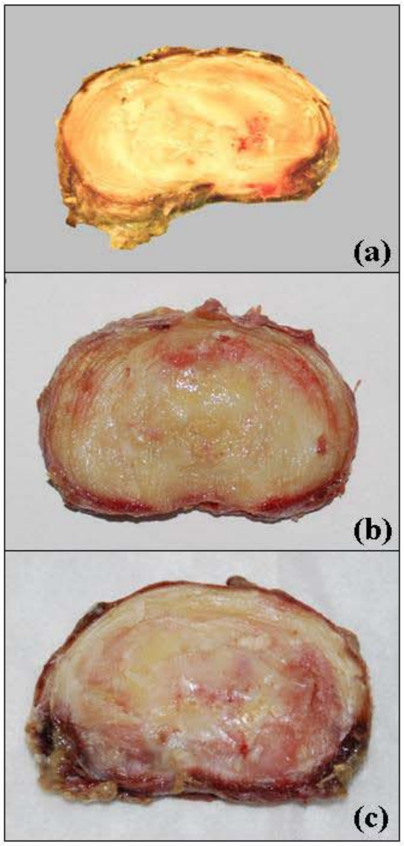

Figure 4.1 Human L3-L4 used in the experiments. (a) Disc obtained from lumbar spine (41 y.o.) classified as Grade I. (b) Disc obtained from lumbar spine (45 y.o.) classified as Grade II. (c) Disc obtained from lumbar spine (45 y.o.) classified as Grade III

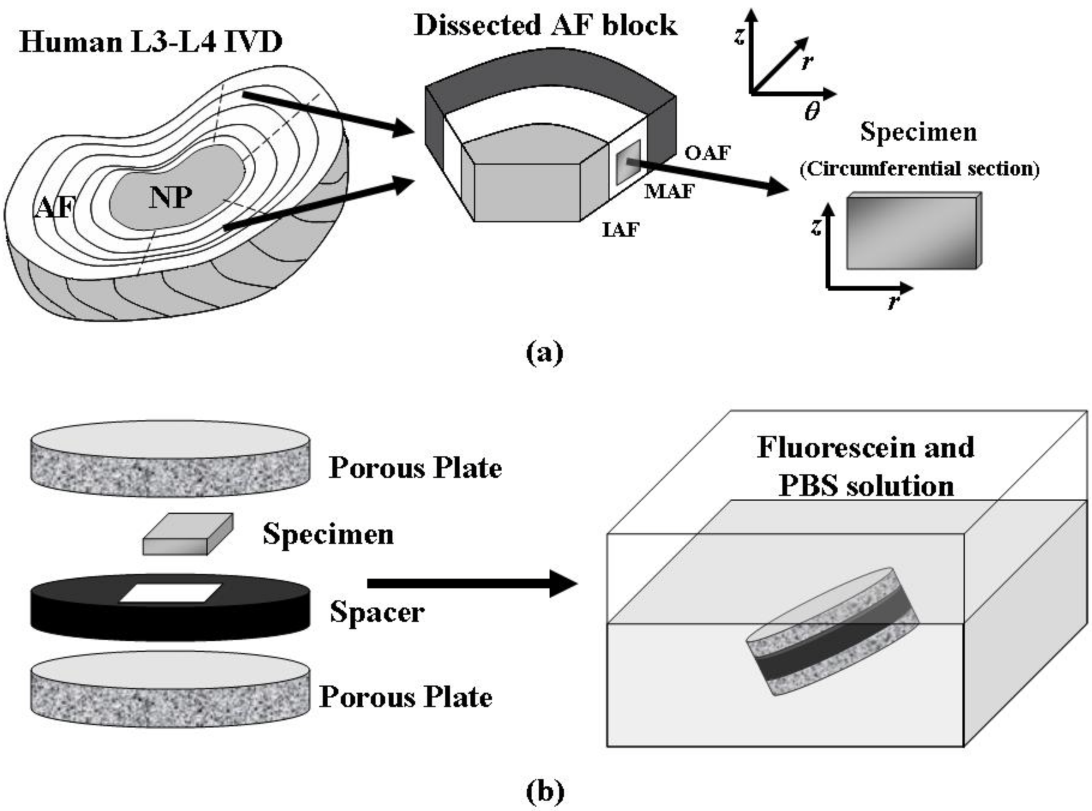

Figure 4.2 (a) Schematic of specimen preparation showing the regions of AF used in experiments: OAF (outer annulus fibrosus), MAF (middle annulus fibrosus) and IAF (inner annulus fibrosus). (b) Schematic of the setup for the equilibration of specimens in a PBS solution with 0.1 mol/m^3 fluorescein.

4.2.4 Imaging and quantitative analysis of disc morphology

For the analysis of AF structure, tissue images were collected by an environmental scanning electron microscope (XL30 ESEM-FEG, FEI Company, Hillsborg, OR, USA) operating in both Scanning Electron Microscopy (SEM) mode, and Environmental Scanning Electron Microscopy (ESEM) mode.

Specimens were harvested from IAF, MAF, and OAF of one disc (grade III). Specifically, two axial sections, and two radial sections were harvested from each of the AF regions.

For SEM imaging, the specimens were fixed with a solution of 2% gluteraldehyde (Electron Microscopy Sciences, Hatfield, PA, USA) in PBS, dehydrated in ethanol and dried by immersion in hexamethyldisilizane (Electron Microscopy Sciences, Hatfield, PA, USA).[71] After sputter coating with Pd (Sputter Coater 108auto, Cressington, Watford, UK), SEM images of specimens were captured.

In addition, in order to corroborate the images acquired in SEM mode, two additional axial specimens from OAF region were imaged in ESEM mode. More specifically, one specimen was observed immediately after dissection. The other specimen was cryogenically frozen after dissection, and then observed by ESEM.

Measurements of the microtube area fraction were performed on SEM images of axial sections of the three regions of AF. The microtube area fraction was defined as the percentage ratio of the voids (microtube cross-sectional areas) to the total area of the image. The image analysis was performed by means of the Particle Analyzer tool provided by ImageJ software (Version 1.39f, by Wayne Rasband, National Institutes of Health, USA), as described in previous studies.[67;164;165;208;209]

4.2.5 Statistical Analysis

A two-way analysis of variance (ANOVA) was performed using SPSS software (SPSS, Inc., Chicago, IL) to analyze the results for fluorescein diffusion coefficients in human AF. The two factors were direction (2 levels: axial and radial) and region (3 levels: IAF, MAF, OAF). Single factor ANOVA tests were performed using SPSS software to determine if regions within AF (i.e., IAF, MAF, and OAF) significantly affected microtube area fraction and water content. Student-Newman-Keuls post hoc test was used in order to determine between which levels of each factor the differences were significant. For all tests, the significance level was set at $p<0.05$. All data are given in mean ± standard deviation.

4.3 Results

Fluorescein diffusivity data in human AF are reported in Table 4.2. The values of the diffusion coefficients in the axial direction (D_{axi}) were significantly higher than those in the radial direction (D_{rad}) in all three regions of AF investigated ($p<0.05$). In particular, it was found that D_{axi} was ~1.4 to ~2.7x of D_{rad}, indicating a significant anisotropic trend for diffusion of fluorescein in human AF tissue. Moreover, disc region significantly affected solute diffusivity ($p<0.05$), with the highest values of both axial and radial diffusion coefficients found in IAF, and the lowest in OAF.

SEM images of radial and axial sections of AF showed differences in the organization of the collagen fibers among IAF, MAF, and OAF. In particular, images showed that, in axial sections, non-contiguous microtubes, with diameters varying from 5 to 50 μm, are clearly visible and extend along the direction of the collagen fiber bundles in AF, see Figure 4.3. Figure 4.4(a-c) shows the difference in microtube density in the three regions of the disc investigated. In contrast, no microtube structures were evident in images of radial sections of AF, see Figure 4.4(d-f), likely due to their orientation parallel to the plane of the radial section. Microtubes were also evident in the images captured in ESEM mode. Figure 4.5(a-b) shows the images of axial sections of OAF obtained using both ESEM protocols (see section 4.2.4). The density and the diameter of the microtubes are similar to those observed in SEM images. The quantitative measurement of the regional variation of microtube area fraction is reported in Table 4.2. It was found that disc region significantly affected the microtube distribution

($p<0.05$), decreasing from IAF to OAF. The trend for decreasing microtube area fraction was similar to that of the diffusion coefficients in both axial and radial direction moving from IAF to OAF.

The values for water volume fraction were highest in IAF and lowest in OAF, see Table 4.2. No statistical difference in water content was found among different groups ($p=0.69$). However, a decreasing trend moving from IAF to OAF was found.

	n	**IAF**	**MAF**	**OAF**
D_{axi} $(x10^{-6}cm^2s^{-1})^{\S}$	36	2.68 ± 0.84	1.54 ± 0.70	1.04 ± 0.45
D_{rad} $(x10^{-6}cm^2s^{-1})^{\S}$	36	1.19 ± 0.76	0.58 ± 0.37	0.38 ± 0.25
ϕ^w	8	0.78 ± 0.16	0.75 ± 0.27	0.69 ± 0.13
Microtube Area Fraction (%)*	10	33.18 ± 2.37	27.45 ± 2.85	17.01 ± 3.58

§: regional and directional significance IAF > MAF > OAF; $D_{axi} > D_{rad}$ ($p < 0.05$)

*: regional significance IAF > MAF > OAF ($p < 0.05$)

Table 4.2. Results for diffusivity of fluorescien in axial (D_{axi}) and radial (D_{rad}) directions, water volume fraction (ϕ^w), and Microtube Area Fraction in the three regions of AF tissue investigated. Microtube Area Fraction was measured in axial specimens only. Values for n shown are for number of tests performed in each region.[193]

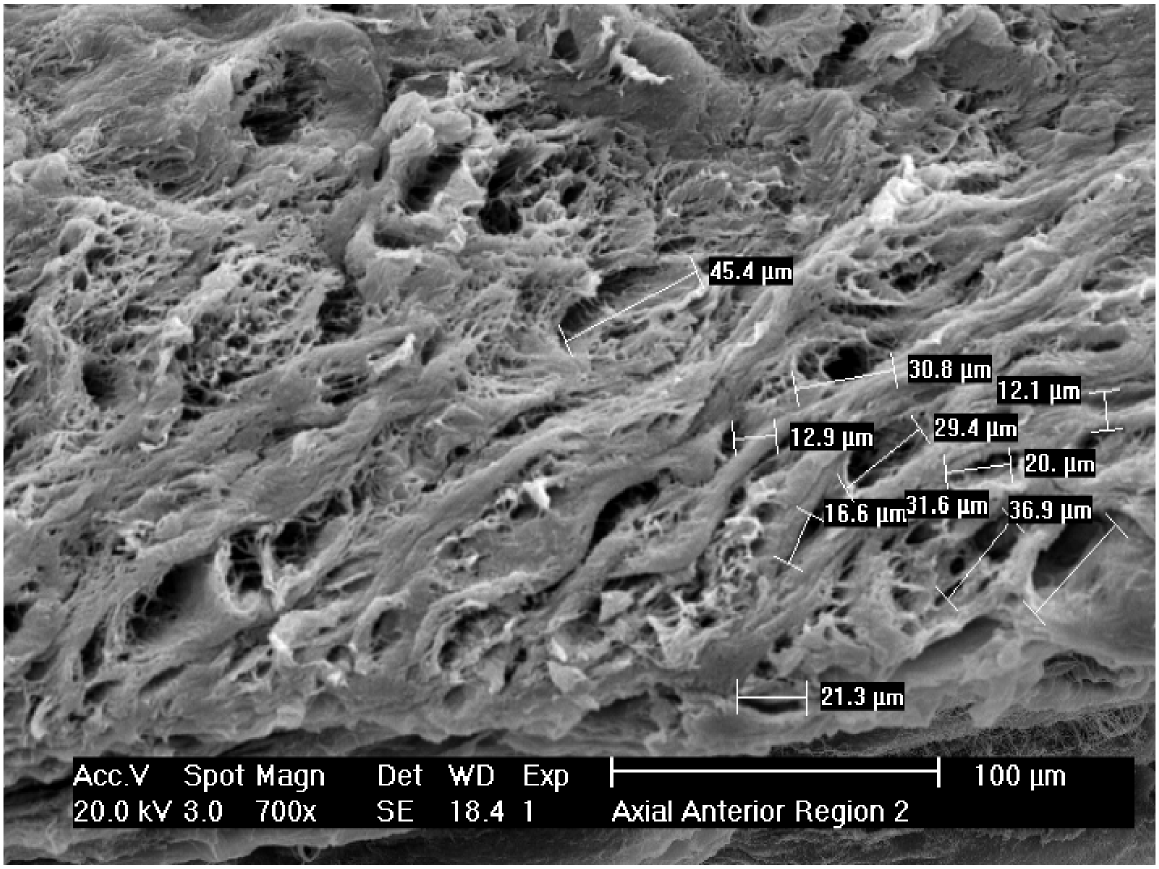

Figure 4.3. SEM image of axial section of human anterior MAF. The diameters of the microtubes can vary from 5 to 50 µm.

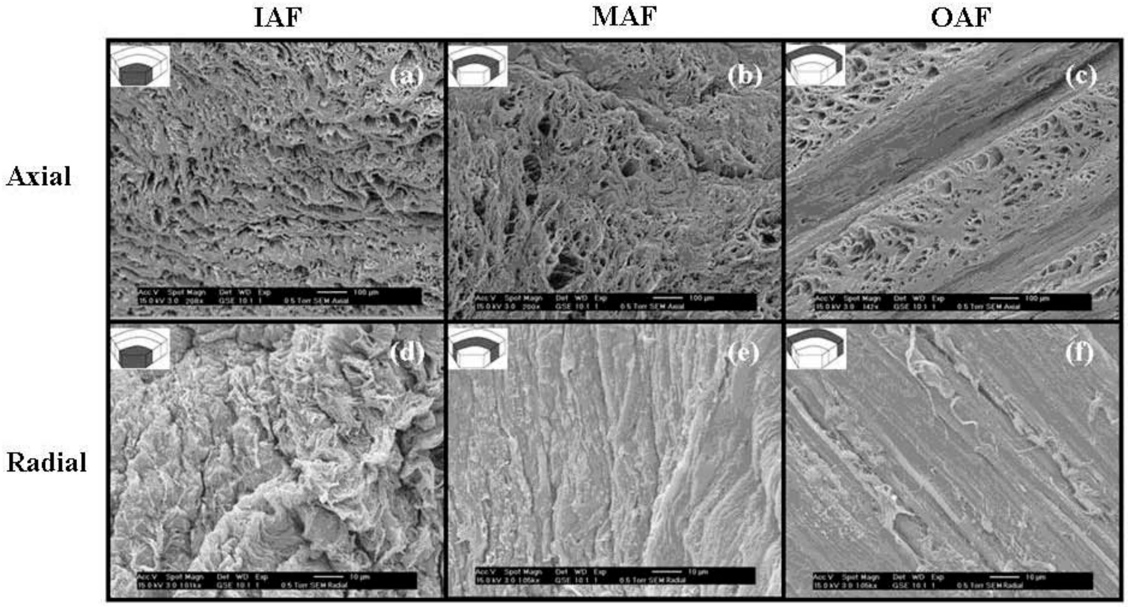

Figure 4.4. SEM images of anterior AF samples. (a-c) Axial sections of IAF, MAF, and OAF. (d-f) Radial sections of IAF, MAF, and OAF.[193]

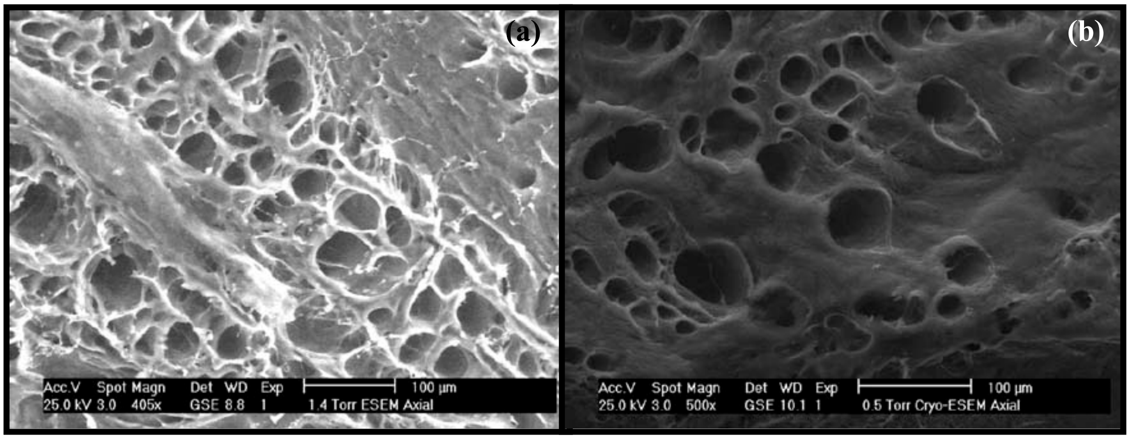

Figure 4.5 ESEM images of anterior axial sections of OAF. (a) Image captured right after specimen dissection. (b) Image captured after cryogenically freezing the dissected specimen.[193] The density and the diameter of the microtubes are similar to those observed in SEM images.

4.4 Discussion

Diffusivity measurements demonstrated that fluorescein diffusion in human AF is both anisotropic (with D_{axi} = ~1.4 to ~2.7x of D_{rad}) and inhomogeneous (both D_{axi} and D_{rad} are the highest in IAF and the lowest in OAF). Water content and microtube area fraction were also found to be inhomogeneous within AF, being highest in the IAF and smallest in OAF. The same trend of variation was found for diffusion coefficients in both the axial and radial directions in human AF.

The values of fluorescein diffusion coefficients determined in this study are lower than those previously determined for ions (Na^+ and Cl^-),[204] glucose,[133] and lactate[173] in human IVD, see Table 1.1. This was expected, since, among these solutes, fluorescein has the highest molecular weight. Moreover, the finding that fluorescein diffusive transport in AF is anisotropic is in agreement with experimental observations previously reported in the literature: the values for the diffusion coefficients of ions (Na^+ and Cl^-), glucose, and fluorescein in bovine coccygeal AF were found to be higher in the axial direction than in the radial.[95;96;192] Similar results were also reported in measurements of water diffusion in ovine and human AF by MRI.[33;43] Furthermore, in each AF region investigated, the ratio of the radial to the axial fluorescein diffusion coefficient was found to be approximately 0.4. By comparison, studies on water and glucose anisotropic diffusion in AF indicated that the ratios of the smallest to the largest diffusion coefficient, measured in different directions of the tissue, are 0.75-0.9 for water,[33;43;84] and 0.66 for glucose,[96] see Table 1.1. These findings would suggest that hindrance to diffusion in the radial direction, caused by the collagen fiber organization within the disc, increases with the size of the solute diffusing in IVD.

The findings reported in this study suggest that solute diffusive transport and tissue composition (i.e., water volume fraction) are related. Indeed, as reported in Table 4.2, the values of diffusion coefficients and water volume fraction consistently decrease from IAF to OAF. This finding is in agreement with a previous study reporting a correlation between solute diffusive transport properties in cartilage and tissue porosity.[66] Moreover, the trend of variation of solute diffusivity was also similar to that of microtube area fraction, remarking the effect of tissue morphology on the transport properties in human AF tissue. As it has been previously suggested by Travascio and Gu (2007),[192] and Jackson et al. (2008),[96] the presence of microtubes may provide justification for the anisotropic behavior of diffusive transport in AF tissue. That is, microtubes, oriented in the direction of the collagen fibers of the lamella, could represent a preferential pathway for solutes, enhancing diffusive transport in the axial direction. In contrast, in the radial direction of AF, solute diffusive transport is hindered by the collagen fiber network, since the microtubes do not appear to be interconnected. The findings reported in this study support this hypothesis, since axial diffusion coefficients are higher than those in the radial direction in all the regions of AF investigated.

Hereby, some of the limitations of this study are discussed. Microtube area fraction measurements could be affected by the sampling, the specimen preparation, and the measurement technique. Indeed, due to the limited number of discs available for the study, all the samples used for image analysis of AF structure were harvested by the same disc (grade III). Besides, during specimen preparation, tissue samples were fixed with gluteraldehyde and then dehydrated in ethanol and dried in hexamethyldisilizane. Dehydration might have altered the size of the samples and, consequently, of the microtubes. However, analysis of ESEM images of AF specimens (non-dehydrated) indicated that the density and the diameter of the microtubes were similar to those observed in SEM images (performed on dehydrated samples). Furthermore, microtube area fraction was determined by measuring the values of cross-sectional areas of microtubes in axial sections of the samples. However, microtube orientation is not perpendicular to the axial section of AF. Thus, the values of microtube area fraction measured in this study might differ from those determined by analyzing images of tissue sections orthogonal to microtube orientation. Additionally, it should be noted that collagen fibers emit fluorescence (auto-fluorescence) when exposed to the laser source used in these experiments (488 *nm* wavelength, see section 4.2.2).[41] However, the effect of collagen auto-fluorescence on the measurement of solute diffusivity by FRAP is expected to be negligible. In a FRAP experiment, the solute diffusivity is determined by the measurement of the time variation of the fluorescence intensity,[195] see Chapter 3. Hence, the variation of the fluorescence intensity is due to the diffusive transport of the fluorescent probes, since collagen fibers are immobile.

4.5 Summary

In this study, it has been hypothesized that: (1) solute diffusivity in human AF is anisotropic and inhomogeneous; (2) transport properties of IVD are associated with its composition and structure. To test these hypotheses, diffusion coefficients of fluorescein in the axial and radial directions of the disc were measured using FRAP. The results were related to the regional variation in water content and collagen architecture in the tissue. Fluorescence recovery experiments confirmed that diffusivity in human lumbar AF is both anisotropic and inhomogeneous. The anisotropic diffusivity may be attributed to the orientation of the microtubes seen in both SEM and ESEM images (i.e., oriented in axial, but not radial direction in AF specimens), suggesting a preferred pathway for axial diffusion. Moreover, the trends of variation of diffusion coefficients, water content and microtube area fraction were consistent among each other (being highest in IAF and lowest in OAF), further indicating a relationship between structure and composition of AF and its transport properties.

The findings of this study are crucial for a better understanding of transport properties in IVD and their complex relationship with the unique structure of this tissue.

Chapter 5: DEVELOPMENT OF NEW TECHNIQUE FOR THE SIMULTANEOUS DETERMINATION OF SOLUTE DIFFUSIVITY AND BINDING INTERACTIONS WITH ECM OF BIOLOGICAL TISSUES

5.1 Introductory remarks

The nutrition and the biosynthetic activity of cells are granted by the availability of several components, such as nutrients, growth factors, extracellular matrix components, etc. In avascular tissues (e.g., articular cartilage, intervertebral disc (IVD), etc.), supply of such components mainly occurs through diffusive transport.[131;199;200]. It has been reported that, certain molecules (e.g., growth factors, amino-acids, etc.,), develop binding reactions with the ECM of the tissue.[3;12;55;93;163]. Binding interactions can have significant implications on solute transport in biological tissues. For instance, Garcia et al. (2003) reported that diffusive transport of IGF-I was dramatically slowed by binding reactions with the ECM of cartilage. Therefore, knowledge of the kinetics of molecular binding is crucial in order to fully understand the mechanisms for molecular transport in tissues.

Techniques able to experimentally investigate solute binding interactions in cells and biological tissues are limited. Recently, fluorescence photobleaching approaches have been proposed for the determination of solute diffusivity and binding reaction rates in living cells and bulk solutions.[22,26,28,29,35,46,102,105,106,120,185,197]However, these methods have only been developed for the case of solute isotropic diffusion. Therefore, their application in those tissues characterized by anisotropic diffusive properties (e.g., intervertebral disc) is limited.

The objective of this study is to develop a new FRAP method to simultaneously determine solute anisotropic diffusivity and binding reaction rates in a biological tissue.

Similarly to the method developed for determining anisotropic diffusion (see Chapter 3), this technique is based on Fourier analysis of the fluorescence emission of video-FRAP images. Hereby, the theoretical approach for this new technique is shown. Moreover, following the same methodological approach used in Chapter 3, the accuracy and the robustness of the method are investigated by numerical simulations of FRAP experiments in presence of binding interactions. Furthermore, the technique is also applied to the simultaneous determination of the two-dimensional (2D) diffusion tensor and the binding reaction rates of a cationic solute, 5-dodecanoylaminofluorescein (DAF), in bovine coccygeal annuls fibrosus (AF).

5.2 Theoretical background

Hereby, the theoretical approach used to develop the new FRAP method is shown. The field equations for diffusive-reactive transport are presented and specialized for the case of a FRAP experiment. It is also shown that, under certain conditions, the diffusive-reactive equations can be reduced to idealized cases of pure diffusion, effective diffusion, or reaction-dominated transport. Finally, the solution of fluorescence recovery for the more general case of diffusive-reactive transport is given.

5.2.1 Field equations of diffusive-reactive transport in FRAP experiments

In the following, it is assumed that solute diffusive-reactive transport is a two-dimensional (2D) anisotropic phenomenon occurring in the focal plane (*x,y*) of the microscope objective. Besides, solute binding interactions with tissue are described by a Langmuir binding model,[53;222] so that a fluorescent solute F can reversibly react with a binding site *S* of the extracellular matrix of the tissue to generate an immobile fluorescent complex *B*. Since, during a FRAP experiment, the tissue can be considered in mechanical equilibrium (i.e., no deformations), the mass balances over the species *F*, *S*, and *B* read:

$$\frac{\partial c^f}{\partial t} = \boldsymbol{D}\nabla^2 c^f - k_{on}c^{bs}c^f + k_{off}c^b, \qquad (5.1a)$$

$$\frac{\partial c^b}{\partial t} = k_{on}c^{bs}c^f - k_{off}c^b, \qquad (5.1b)$$

$$\frac{\partial c^{bs}}{\partial t} = -k_{on}c^{bs}c^f + k_{off}c^b, \qquad (5.1c)$$

where $\boldsymbol{D}$ is the anisotropic diffusion tensor of the solute *F*, and k_{on} and k_{off} are the constant rates of binding and unbinding. Note that, consistent with the notation used in Section 2.2, c^f, c^{bs}, and c^b denote the molar concentration of *F*, *S*, and *B*, respectively. It should be also noted that, in Equations (5.1b and 5.1c), no diffusive terms are present, since both *S* and *B* are attached to the extracellular matrix of the tissue. The set of Equations (5.1) can be further simplified by assuming that, before photobleaching, the tissue is in chemical equilibrium. This condition means that, before a FRAP experiment, the concentrations of *F*, *S*, and *B* can be expressed in terms of concentrations at equilibrium (i.e., steady state) as it follows:

$$c^f = c^f_{eq}, \qquad (5.2a)$$

$$c^b = c^b_{eq}, \qquad (5.2b)$$

$$c^{bs} = c^{bs}_{eq}. \qquad (5.2c)$$

During a FRAP experiment, the amount of binding sites is constant ($c^{bs} = c^{bs}{}_{eq}$), since the act of bleaching only changes the number of fluorescent molecules (*F* or *B*) present in the tissue. Under this assumption, Equations (5.1) can be written as:

$$\frac{\partial c^f(x,y,t)}{\partial t} = \boldsymbol{D}\nabla^2 c^f(x,y,t) - \frac{\partial c^b(x,y,t)}{\partial t}, \quad (5.3a)$$

$$\frac{\partial c^b(x,y,t)}{\partial t} = k^*_{on} c^f(x,y,t) - k_{off} c^b(x,y,t). \qquad (5.3b)$$

In Equation (5.3b), $k^*{}_{on}$ is the pseudo-binding rate, defined as:[185]

$$k^*_{on} = k_{on} c^{bs}_{eq}. \quad (5.4)$$

Note also that, from Equation (5.3b), the following relationship between free and bound solutes holds at equilibrium:

$$\frac{c^b_{eq}}{c^f_{eq}} = \frac{k^*_{on}}{k_{off}}. \qquad (5.5)$$

Normalizing c^f and c^b by the total pre-bleach concentration of F and B yields to:

$$\bar{c}^f_{eq} + \bar{c}^b_{eq} = 1, \quad (5.6)$$

where $\overline{c}_{eq}^{f}$ and $\overline{c}_{eq}^{b}$ are the normalized pre-bleach concentrations of free and bound solute, respectively. Thus, from Equations (5.5) and (5.6) we have:

$$\overline{c}_{eq}^{f} = \frac{k_{off}}{k_{on}^{*} + k_{off}}, \qquad (5.7a)$$

$$\overline{c}_{eq}^{b} = \frac{k_{on}^{*}}{k_{on}^{*} + k_{off}}. \qquad (5.7b)$$

After photobleaching, within the bleached spot, the equilibrium between visible (fluorescent) and bleached molecules is altered. The recovery of the equilibrium (i.e., fluorescence) is achieved by diffusion of free fluorescent solute in the bleached spot, according to Equations (5.3). Several strategies have been proposed in order to solve the system of equations (5.3). In this study, an approach based on 2D Fourier transform is used. The details of the method are reported in Section 5.2.3.

5.2.2 Dimensionless analysis of the field equations for diffusive-reactive transport

In this analysis, for the sake of simplicity, the ideal case of isotropic diffusive-reactive transport is considered. The extension of the dimensionless analysis to the more general case of anisotropic diffusion can be easily derived.

In FRAP experiments involving isotropic diffusive-reactive transport, the recovery of the fluorescence intensity within the images is controlled by four parameters: the diffusion coefficient D, the binding and unbinding rates k^{*}_{on} and k_{off}, and the initial dimension of the bleach spot (d). Let Da and R be two dimensionless numbers defined as:

$$Da = \frac{d^2 k^*_{on}}{D}, \quad R = \frac{k^*_{on}}{k_{off}} \qquad (5.8)$$

The number *Da* represents the ratio of the diffusion time to the characteristic time of binding association, and, therefore, has the physical meaning of the Damkhöler number.[52] The number *R* represents the ratio of the characteristic times of binding dissociation to that of binding association. Let *d* be the characteristic length and τ the characteristic time of the diffusive-reactive process, defined as:

$$\alpha = \frac{d^2}{D}(1+R). \qquad (5.9)$$

Therefore, the Equations (5.3), for an isotropic case, can be rewritten in the dimensionless form as it follows:

$$\frac{\partial \bar{c}^f}{\partial \hat{t}} = (1+R) \cdot \hat{\nabla}^2 \bar{c}^f - \frac{\partial \bar{c}^b}{\partial \hat{t}}, \quad (5.10\text{ a})$$

$$\frac{\partial \bar{c}^b}{\partial \hat{t}} = (1+R) Da \cdot \bar{c}^f - (1+\frac{1}{R}) Da \cdot \bar{c}^b, \quad (5.10\text{b})$$

where $\bar{c}^f$ and $\bar{c}^b$ are the concentrations of free and bound solutes normalized by the total pre-bleach concentration of fluorescent solute; $\hat{t}$ (defined as $\hat{t} = t/\tau$) and $\hat{\nabla}^2$ (defined as $\hat{\nabla}^2 = \nabla^2 \cdot d^2$) are the dimensionless time and the dimensionless Laplacian operator, respectively. Equations (5.10) indicate that the two dimensionless numbers, *Da* and *R*, govern the diffusive-reactive fluorescence recovery. For special values of *Da* and *R*, Equations (5.10) can be approximated to idealized cases,[185] whose solutions have been reported in literature.

5.2.2.1 Purely diffusive transport

Fluorescence recovery can be considered purely diffusive when $R \ll 1$. Indeed, Equation (5.10 b) can be approximated by the following relationship:

$$\frac{\partial \bar{c}^b}{\partial \hat{t}} \cong -\frac{Da}{R} \cdot \bar{c}^b , \qquad (5.11)$$

which yields to:

$$\bar{c}^b(x,y,t) = \bar{c}^b(x,y,0) e^{-\frac{Da}{R} t} . \qquad (5.12)$$

It can be proven that (5.12) yields to $\bar{c}^b(x,y,t) = 0$ since, for $R \ll 1$, $\bar{c}^b(x,y,0) \leq 0$, see Equation (5.5). Under these conditions, Equation (5.10 a), rewritten in dimensional form, modifies into the diffusion equation:

$$\frac{\partial c^f}{\partial t} = D \cdot \nabla^2 c^f . \qquad (5.13)$$

A FRAP method for determining the diffusion coefficient from Equation (5.13) has been presented in Chapter 3.

5.2.2.2 Effective diffusive transport

In the case *Da*>>1, fluorescence recovery is considered to be governed by effective diffusion (or instantaneous reaction[36]). In this case, binding reactions occur much faster than diffusive transport, so that, at each time≤, $c^b/{\leq}t \leq 0$. From Equation (5.10b), we have:

$$c^b = R \cdot c^f \,. \quad (5.14)$$

Introducing Equation (5.14) into (5.10 a) and rewriting in dimensional form, we have:

$$\frac{\partial c^f}{\partial t} = \frac{D}{(1+R)} \cdot \nabla^2 c^f \,, \ (5.15)$$

where the term $D/(1+R)$ is referred as effective diffusion coefficient (D_{eff}).[36;185] From Equation (5.15) it can be concluded that, in effective diffusion, fluorescence recovery follows a diffusive transport kinetic regulated by D_{eff}.

In the case of effective diffusion, D_{eff} can be determined by using the FRAP approach reported in Chapter 3.

5.2.2.3 Reaction dominated transport

When Da<<1 and R≤1, fluorescence recovery is mainly reaction-driven. In this case, diffusion occurs much faster than binding reaction, so that, at any time, free solute is considered to be at equilibrium [$\partial \bar{c}^f/\partial t = 0, \Rightarrow \bar{c}^f(x,y,t) = \bar{c}^f_{eq} = 1/(1+R)$, see Equation (5.7a)]. Therefore, Equations (5.10) modify into:

$$\bar{c}^f = \frac{1}{1+R}, \quad (5.16a)$$

$$\frac{\partial c^b}{\partial t} = \frac{k^*_{on}}{1+R} - k_{off} c^b. \quad (5.16b)$$

Equations (5.16) indicate that reaction dominant fluorescence recovery is only controlled by binding and unbinding reaction rate constants. Note that the rate of fluorescence recovery is only regulated by k_{off}, see second term on the right hand side of Equation (5.16b). This result is consistent with previously reported analytical solutions for fluorescence recovery in the case of reaction-driven transport.[26;105;106;185]

5.2.3 Model for diffusive-reactive transport in FRAP experiments

The system of equations (5.3) is transformed into the Fourier space defined by the system of coordinates (u,v):

$$\frac{dC^f(u,v,t)}{dt} = -4\alpha^2(u^2+v^2)D(\xi)C^f(u,v,t) - \frac{dC^b(u,v,t)}{dt} \qquad (5.17a)$$

$$\frac{dC^b(u,v,t)}{dt} = k^*_{on}C^f(u,v,t) - k_{off}C^b(u,v,t) \qquad (5.17b)$$

where C^f and C^b are the 2D Fourier transforms of the concentrations of free and bound solutes, respectively. The function $D(\xi)$, defined in Chapter 3 as:

$$\begin{aligned} &D(\xi) = D_{xx}\cos^2\alpha + 2D_{xy}\cos\xi\sin\xi + D_{yy}\sin^2\alpha \\ &(\text{with} \quad \alpha = tan^{-1}(v/u)) \end{aligned} ,(3.8)$$

embeds the components of the 2D diffusion tensor ***D*** (i.e., D_{xx}, D_{xy}, and D_{yy}). Introducing the auxiliary variables C^{f*} and C^{b*}, defined as:

$$\begin{aligned} C^{f*}(u,v,t) &= \frac{C^f(u,v,t)}{C^f(u,v,0)+C^b(u,v,0)} \\ C^{b*}(u,v,t) &= \frac{C^b(u,v,t)}{C^f(u,v,0)+C^b(u,v,0)} \end{aligned} , \qquad (5.18)$$

Equations (5.17) can be rewritten in a more compact form as:

$$\begin{bmatrix} \dot{C}^{f*} \\ \dot{C}^{b*} \end{bmatrix} = \begin{bmatrix} a & b \\ c & d \end{bmatrix} \begin{bmatrix} C^{f*} \\ C^{b*} \end{bmatrix}, \qquad (5.18)$$

with

$$\begin{aligned} a &= -4\alpha^2(u^2+v^2)D(\xi) - k_{on}^* \\ b &= k_{off} \\ c &= k_{on}^* \\ d &= -k_{off} \end{aligned} \qquad (5.19)$$

For the system of equations (5.18), the characteristic equation and its discriminant (*Δ*) are written as:

$$\alpha^2 - (a+d)\alpha + ad - bc = 0, \quad (5.20)$$

and

$$\alpha = (a-d)^2 + 4bc\,. \quad (5.21)$$

Since it can be proven that *Δ*>0 and (*ad-bc*)α0, the solution of the system of equations (5.18) is:

$$C^{f*}(u,v,t) = K_1 b e^{\alpha_1 t} + K_2 b e^{\alpha_2 t} \qquad (5.22a)$$

$$C^{b*}(u,v,t) = K_1(\alpha_1 - a)e^{\alpha_1 t} + K_2(\alpha_2 - a)e^{\alpha_2 t}, \qquad (5.22b)$$

where α_1 and α_2 are the roots of the characteristic equation (5.20). Providing initial conditions to equations (5.18), the constants of integration K_1 and K_2 can be determined. Assuming that, before bleaching ($t=0$), the system is at equilibrium (both dC^{f*}/dt and dC^{b*}/dt equal zero), from equations (5.18) we have:

$$k^*_{on} C^{f*}(u,v,0) = k_{off} C^{b*}(u,v,0)\,. \quad (5.23)$$

Since $C^{f*}(u,v,0)+C^{b*}(u,v,0)=1$, we have:

$$C^{f*}(u,v,0)=\frac{k_{off}}{k_{on}^{*}+k_{off}}, \qquad (5.24a)$$

$$C^{b*}(u,v,0)=\frac{k_{on}^{*}}{k_{on}^{*}+k_{off}}, \qquad (5.24b)$$

which represent the initial conditions for equations (5.18). By evaluating equations (5.22) at $t = 0$ and using Equation (5.24), we have:

$$K_2=\frac{a+c-\alpha_1}{(b+c)(\alpha_2-\alpha_1)}, \qquad (5.25a)$$

$$K_1=\frac{\alpha_2-a-c}{(b+c)(\alpha_2-\alpha_1)}. \qquad (5.25b)$$

Note that, in Fourier space, the intensity of the fluorescence emission is proportional to the total concentration of the fluorescent solute ($C=C_f+C_b$)[185] according to the following relationship:[9]

$$\frac{I(u,v,t)}{I(u,v,0)}=\frac{C(u,v,t)}{C(u,v,0)}, \quad (5.26)$$

where I is the 2D Fourier transform of the fluorescence intensity of FRAP images. Therefore, combining equations (5.22), (5.25), and (5.26), it follows:

$$\frac{I(u,v,t)}{I(u,v,0)} = Ae^{\alpha_1 t} + Be^{\alpha_2 t}, \quad (5.27)$$

with:

$$A = \frac{(\alpha_2 - a - c)(\alpha_1 - a + b)}{(b + c)(\alpha_2 - \alpha_1)}, \qquad (5.28a)$$

$$B = \frac{(a + c - \alpha_1)(\alpha_2 - a + b)}{(b + c)(\alpha_2 - \alpha_1)}. \qquad (5.28b)$$

By curve-fitting the 2D Fourier transform of the intensity of the fluorescence emission of a time series of video-FRAP images with equation (5.27), one can simultaneously determine the reaction rate constants k^*_{on} and k_{off}, together with the coefficient $D(\xi)$. The principal components of $\boldsymbol{D}$ can be calculated from $D(\xi)$ as shown in Chapter 3.

5.3 Methods

In this study, numerically simulated FRAP experiments were used to validate the method proposed and to evaluate its sensitivity to experimental parameters, such as reaction rates of binding and unbinding, anisotropic ratio of the principal components of the diffusion tensor, and initial dimension of the bleached spot. Finally, the technique was applied to the experimental determination of diffusivity and binding rate constants of a cationic solute, 5-dodecanoylaminofluroescein, in bovine coccygeal annulus fibrosus (AF).

5.3.1 Computer simulations of FRAP tests

A finite element method package (COMSOL® 3.2, COMSOL Inc., Burlington, MA) was used to simulate 2D anisotropic fluorescence recovery after photobleaching in presence of binding reactions. Initially, the normalized fluorescent solute concentration (both free and bound) was assumed to be uniform ($c^f+c^b=1$) within the sample and zero within the bleached spot. At the boundaries of the simulation domain (4x4 mm^2), the normalized concentration of the fluorescent probe was assumed to be constant ($c^f+c^b=1$). A mesh of approximately 8000 quadratic Lagrange triangular elements was used in the simulations. The implicit solver of COMSOL® (based on the implicit Euler backward scheme) was used for the simulations. The convergence criterion for the solution was the relative error tolerance of less than 10^{-3}. In each simulation fluorescence recovery was always more than 95% of the initial concentration value in the sample ($c^f+c^b=1$). For data analysis purposes, a time series of 200 images (8-bit grey scale) of 128x128 pixel, representing the fluorescence recovery on the focal plane of the microscope objective, was extracted from the simulation domain, see Figure 5.1. The physical dimension (L) of the series of FRAP images corresponded to 8 times the value of the diameter of the bleach spot (d) used in the simulations (see below).

In FRAP experiments involving diffusive-reactive transport, the behavior of fluorescence recovery is regulated by two dimensionless numbers, Da and R, which depend on the rates of binding and unbinding (k^*_{on} and k_{off}), the solute diffusivity ($\boldsymbol{D}$), and the initial diameter of the bleach spot (d), see Section 5.2.2. The sensitivity of the new model was investigated for a wide range of both Da and R. This was done by varying both transport and experimental parameters used in the simulations. For most solutes, the measured values of diffusion coefficients in cartilaginous tissues range from $5\cdot10^{-8}$ to $5\cdot10^{-6}$ cm^{2}s^{-1}.[94] In simulations of isotropic diffusive-reactive fluorescence recovery, it was chosen a representative value of the diffusion coefficient (D) equal to $5\cdot10^{-7}$ cm^{2}s^{-1}. In numerically simulated FRAP experiments involving anisotropic diffusion, the trace of the diffusion tensor ($tr(\boldsymbol{D})=D'_{xx}+D'_{yy}$) was set to 10^{-6} cm^{2}s^{-1}. Besides, the anisotropic ratio between the two principal components of $\boldsymbol{D}$ (i.e., D'_{xx} and D'_{yy}) varied from D'_{xx} = 1.5x to 3x of D'_{yy}, and the orientation (θ) of the principal directions of $\boldsymbol{D}$ with respect to the coordinate system of the microscope objective (x,y) was equal to 45°. Few studies reported the values of the binding and unbinding rates of solutes in tissues. In this framework, a 10^6–fold range of the reaction rates was explored by varying k^*_{on} and k_{off} from 10^{-3} to 10^3 s^{-1}. Additionally, since confocal laser scanning microscopes (CLSM) allow to define the initial dimensions of the bleach spot used during a FRAP experiment, in the simulations, the value of d varied from 4 to 16 μm.

The evaluations of the accuracy and the robustness of this FRAP method were performed following the same methodological approach followed in Chapter 3: FRAP experiments were simulated by inputting the components of $\boldsymbol{D}$, k^*_{on} and k_{off}; subsequently, the numerically simulated FRAP images were analyzed to output the values of the same quantities. The accuracy of the method was assessed by the relative error (ε), defined as:

$$\varepsilon = 100\cdot\frac{|Input - Output|}{Input}\ (\%). \quad (5.29)$$

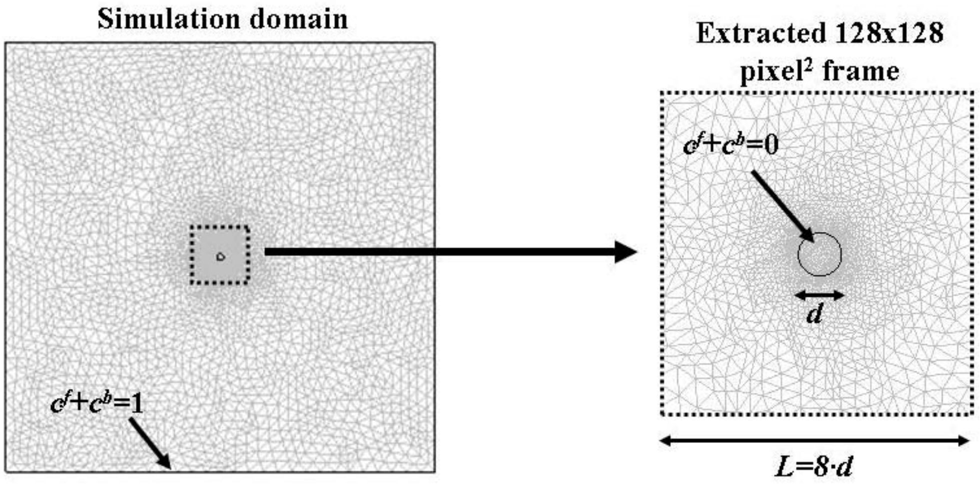

Figure 5.1 Mesh and size of the simulation domain. The initial and boundary conditions are shown.

Simulated FRAP experiments involving isotropic diffusion were used to investigate the accuracy of the new method when different sizes of bleach spot are used. The results were compared to those obtained by simultaneously analyzing multiple FRAP tests, obtained at different values of *d*. In addition, the accuracy of the technique was also investigated for anisotropic diffusive-reactive fluorescence recovery.

5.3.2 FRAP experiments on bovine annulus fibrosus

The protocol of specimen preparation adopted in this study is similar to that used in Chapter 3 for FRAP tests on bovine AF (see Section 3.4.2). Briefly, eight cylindrical specimens (5 mm diameter, 270 μm thickness) were obtained from circumferential sections of AF blocks harvested from a bovine coccygeal S2-S3 IVD, see Figure 5.2a. A cationic solute, 5-dodecanoylaminofluorescein (DAF), was used in the experiments to investigate diffusion and binding reactions in AF tissue. Specimens were equilibrated in a

PBS solution with 0.1 mol/m^3 DAF (529 Da, λ_{ex} 485 nm; λ_{em} 535 nm, Molecular Probes, Inc., Eugene, OR). In order to prevent swelling during equilibration, AF specimens were confined between two sinterized stainless steel plates (10 μm porosity) and an impermeable spacer,[192;193] see Figure 5.2b. A total of sixteen FRAP experiments (2 experiments each specimen) were performed.

Experiments were conducted at room temperature (22°C) with a confocal laser scanning microscope (LSM 510 Zeiss, Jena, Germany) using a Planar-Neofluar 20x/0.5 WD 2.0 objective (Zeiss). Specimens were photobleached using a 25mW argon laser (488nm wave length). For data analysis purposes (see section 5.3.3), each FRAP experiment comprised three consecutive cycles of photobleaching and recovery, performed in the same area of the sample. For each cycle of photobleaching and recovery, a different size of bleach spot diameter (*d*) was used. More specifically, three values of *d* were used: d_1=3.6 μm, d_2=7.2μm, and d_3=14.4μm. In each cycle, the size of the video-FRAP images was eight times the value of *d* used in photobleaching. A total of 200 frames (128x128 pixel), five of them before bleaching the sample, were collected in each cycle. The time delay between two consecutive frames was 0.1 seconds. The time delay between two consecutive cycles was sufficient for reaching complete fluorescence recovery in the sample. Due to the thickness of the samples (270 μm), a multi-layer bleaching (MLB) protocol, similar to that used in previous studies on fluorescein diffusion in bovine AF (see Section 3.4.4), was adopted.

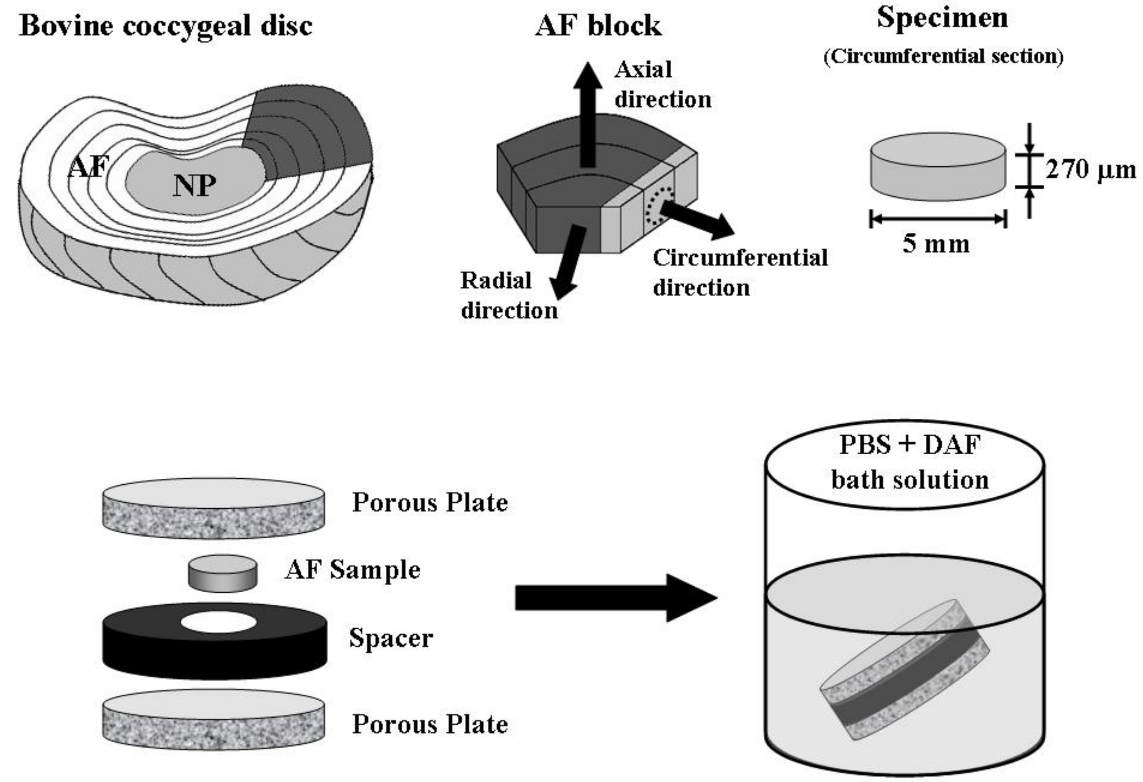

Figure 5.2 Schematic of specimen preparation. The orientation and the dimensions of the bovine AF sample are shown. The setup for the equilibration of specimens in a PBS solution with 0.1 mol/m^3 DAF is shown.

5.3.3 Data analysis

Both computer-simulated and experimental FRAP images were analyzed by a custom-made, MATLAB-based algorithm (MATLAB® Version 7.7.0.471 (R2008b), The MathWorks Inc., Natick, MA) performing the curve-fitting of the Fourier transform of video FRAP images with the model Equation (5.27), to yield k^*_{on}, k_{off}, and $D(\xi)$. The orientation (θ) of the principal directions of $\boldsymbol{D}$ (see Figure 3.1) was determined by Karhunen-Loéve transform (KLT) analysis of the bleached spot in the recovered images, as described in Section 3.4.5. Finally, the principal components of $\boldsymbol{D}$ were determined from Equations (3.13) and (3.14), provided tr($\boldsymbol{D}$) and D_{xy} from Equations (3.9) and (3.15), respectively.

Experimental FRAP data relative to 3 consecutive cycles of photobleaching and recovery (d varying from 3.6 to 14.4 μm), were simultaneously curve-fitted to yield k^*_{on}, k_{off}, and the components of $\boldsymbol{D}$ along the axial (D_{axi}) and the radial (D_{rad}) direction of AF.

5.3.4 Statistical analysis

A paired *t*-test was performed using Excel Spreadsheet software (Microsoft® Office Excel 2003, Microsoft Corp., Seattle, WA) in order to determine if a statistically significant difference existed between the binding and unbinding rates (k_{on}^* and k_{off}) of DAF in bovine AF. Additionally, a paired *t*-test was also performed to verify statistical differences between the components of the diffusion tensor along the axial (D_{axi}) and radial (D_{rad}) directions of AF.

5.4 Results

5.4.1 Numerical validation

The case of isotropic diffusion with binding reaction was used to validate the method. The relative errors (ε) in determining D, k^*_{on}, and k_{off}, using FRAP, are reported in Figures 5.3-6. The areas of the contour plots indicate values of ε less than 2% (white), between 2 and 5% (blue), between 5 and 10% (light blue), between 10 and 20% (green), and more than 20% (red). In determining D, the method was sensitive to the choice of the initial diameter of the bleach spot. The accuracy of the technique was the lowest when d was the smallest, see Figures 5.3a-c. The highest accuracy was obtained when data from 3 FRAP experiments, performed at d = 4, 8, and 16 μm, were simultaneously analyzed:

the relative error was less than 2% for most values of k_{off} (ranging from 10^{-3} to 10^{3} s^{-1}) and k^{*}_{on} (ranging from 10^{-3} to 10^{2} s^{-1}), see Figure 5.3d.

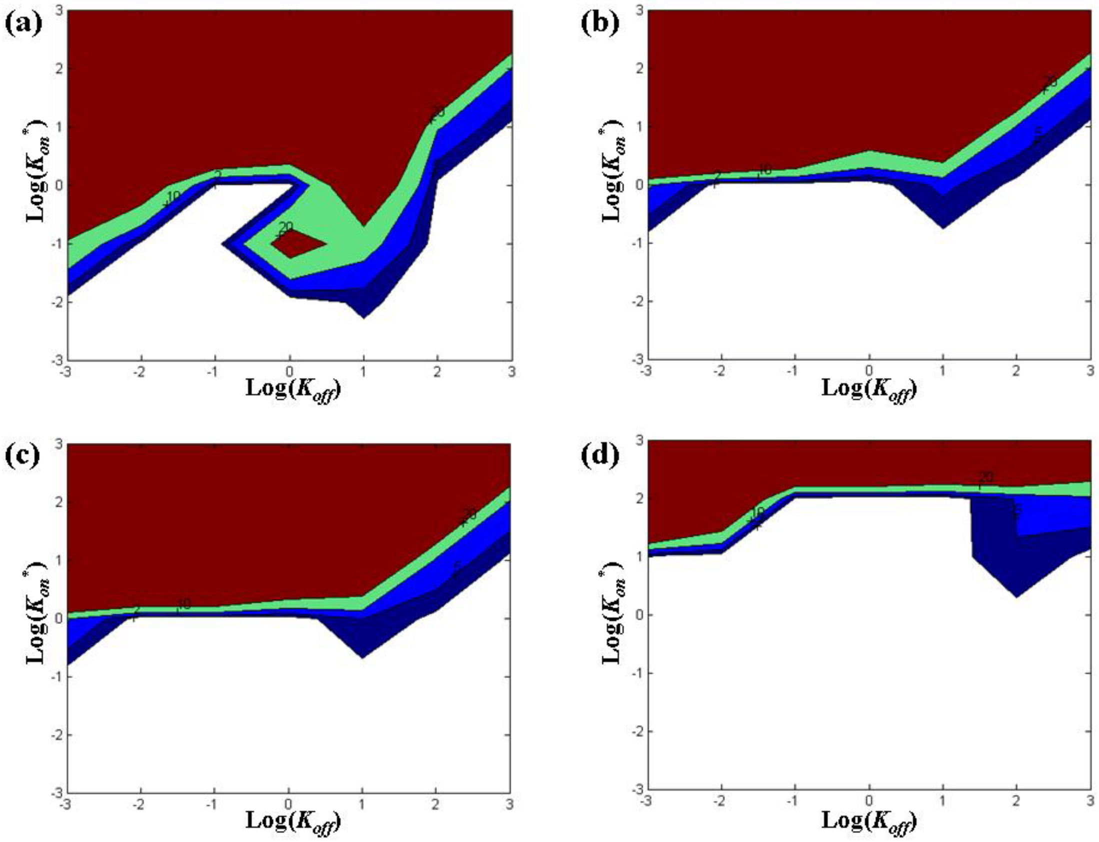

Figure 5.3 Effect of the initial bleached spot size (d) on the relative error (ε) for the determination of D. The areas of the contour plot indicate values of ε less than 2% (white), between 2 and 5% (blue), between 5 and 10% (light blue), between 10 and 20% (green), and more than 20% (red). **(a)** d = 4 μm; **(b)** d = 8 μm; **(c)** d = 16 μm; **(d)** simultaneous analysis of data produced at d = 4, 8, and 16 μm. For all the cases reported in this figure, $D = 5 \cdot 10^{-7}$ $cm^{2}s^{-1}$.

In contrast, the choice of d slightly affected the accuracy for determining k^{*}_{on}, and k_{off}, see Figures 5.4a-c and 5.5a-c. However, the accuracy of the method significantly improved when FRAP experiments produced with 3 different d were simultaneously curve-fitted, see Figures 5.4d and 5.5d.

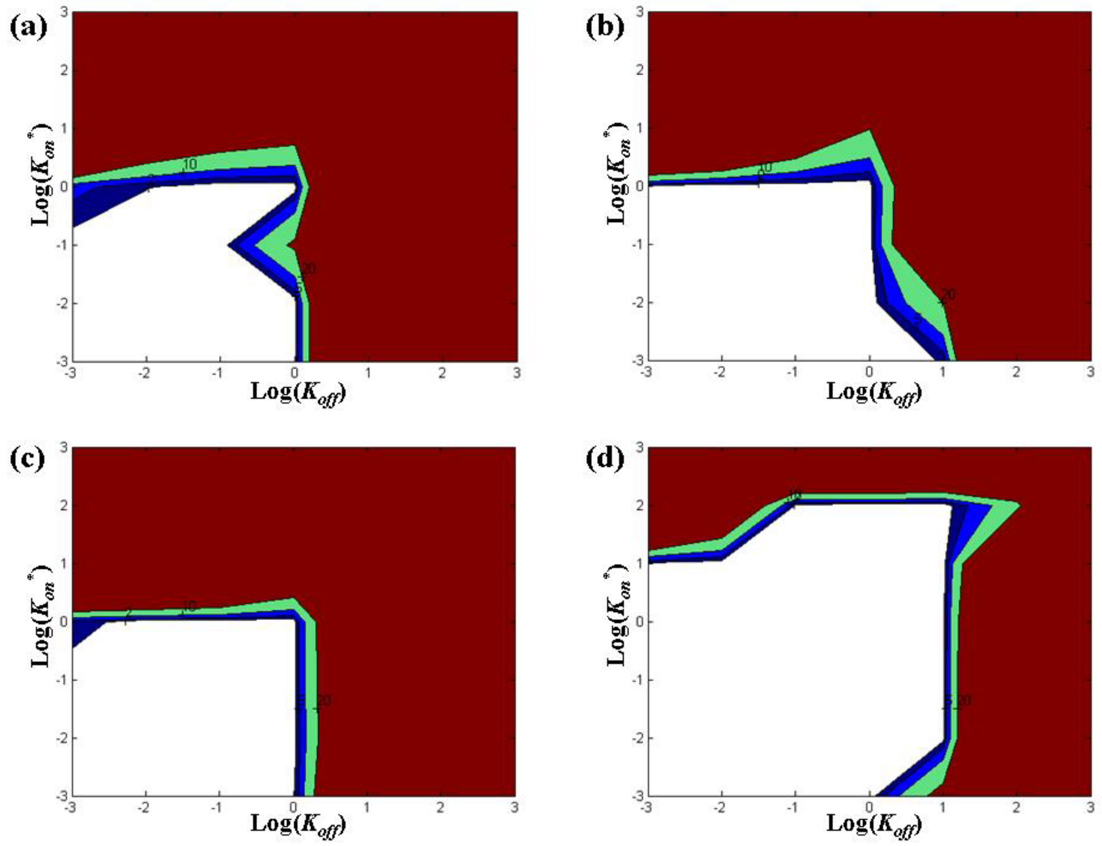

Figure 5.4 Effect of the initial bleached spot size (d) on the relative error (ε) for the determination of k^*_{on}. **(a)** d = 4 μm; **(b)** d = 8 μm; **(c)** d = 16 μm; **(d)** simultaneous analysis of data produced at d = 4, 8, and 16 μm. For all the cases reported in this figure, $D = 5 \cdot 10^{-7}$ cm^{2}s^{-1}.

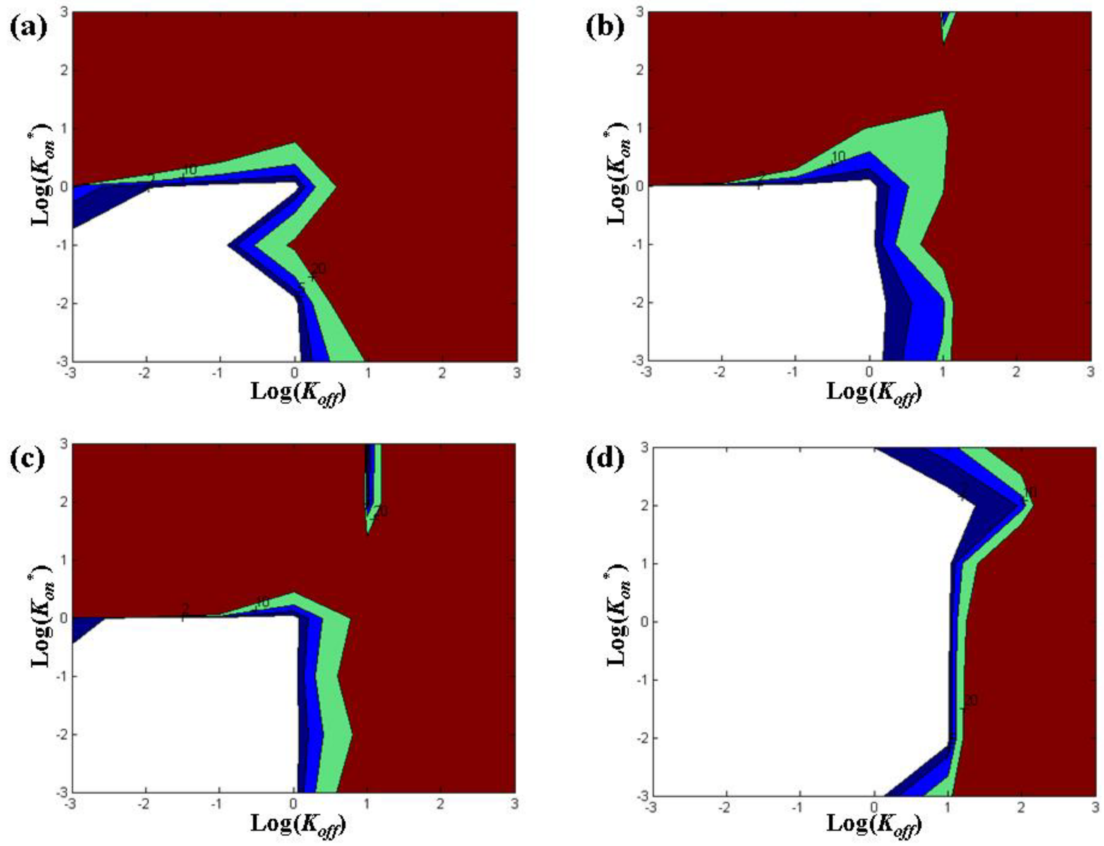

Figure 5.5 Effect of the initial bleached spot size (*d*) on the relative error (ε) for the determination of k_{off}. **(a)** d = 4 µm; **(b)** d = 8 µm; **(c)** d = 16 µm; **(d)** simultaneous analysis of data produced at d = 4, 8, and 16 µm. For all the cases reported in this figure, $D = 5 \cdot 10^{-7}$ cm^{2}s^{-1}.

The diagrams reported in Figure 5.6, obtained by intersecting the values of ε generated in determining D, k^*_{on}, and k_{off}, summarize the robustness of the method in determining the experimental parameters of diffusive-reactive fluorescence recovery. When 3 FRAP experiments were simultaneously analyzed, the value of ε was less than 2% for most values of k_{off} (ranging from 10^{-3} to 10^{1} s^{-1}) and k^*_{on} (ranging from 10^{-3} to 10^{2} s^{-1}), see Figure 5.6d.

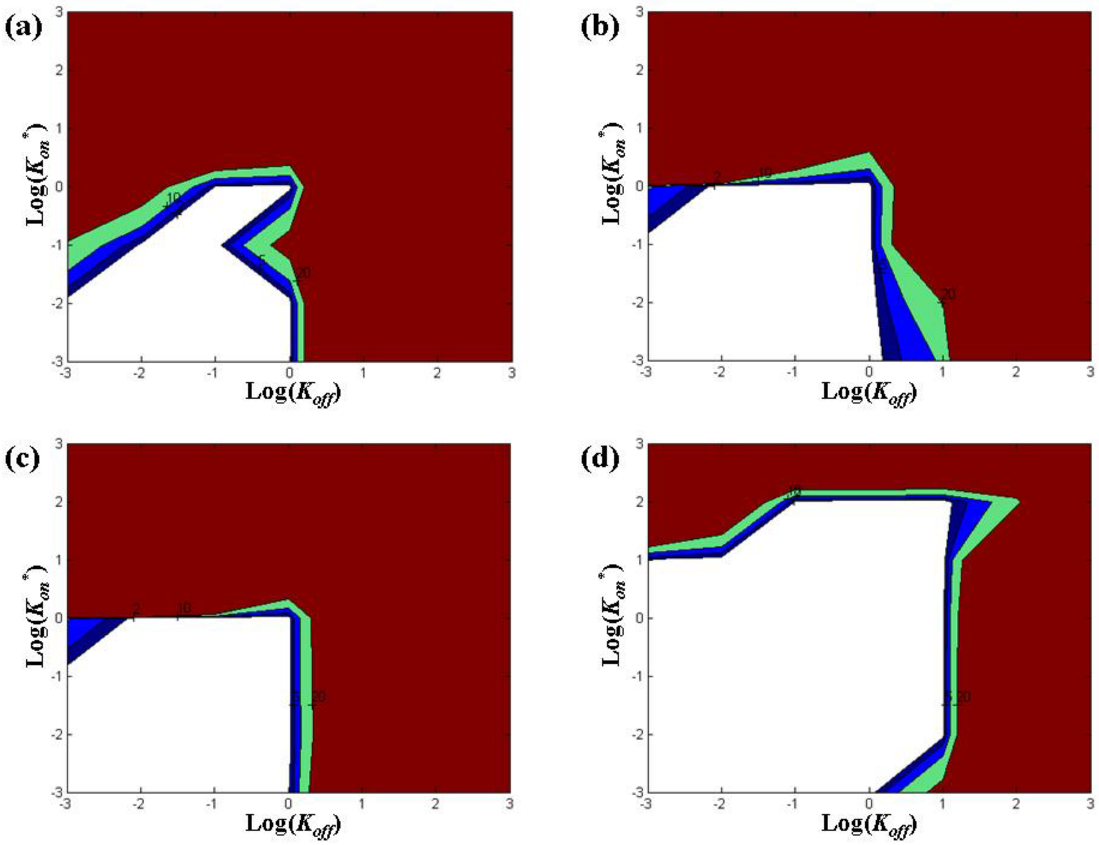

Figure 5.6 Intersection of the relative errors (ε) for the determination of D, k^{*}_{on}, and k_{off}. **(a)** $d = 4$ μm; **(b)** $d = 8$ μm; **(c)** $d = 16$ μm; **(d)** simultaneous analysis of data produced at $d = 4$, 8, and 16 μm. For the case reported in this figure, $D = 5 \cdot 10^{-7}$ cm^{2}s^{-1}.

The accuracy of the technique was also investigated in the case of anisotropic diffusion. Specifically, three anisotropic ratios were studied, namely $D'_{xx}/D'_{yy} = 1.5$, 2, and 3. For each of the cases investigated, 3 FRAP experiments, obtained at $d = 4$, 8, and 16 μm, were simultaneously curve-fitted to yield $tr(\boldsymbol{D})$, D_{xy}, k^{*}_{on}, and k_{off}. For the range of k^{*}_{on} and k_{off} explored, the accuracy of the technique in determining both $tr(\boldsymbol{D})$ and D_{xy} slightly reduced when the anisotropic ratio increased, see Figures 5.7a-f.

The values of ε in estimating k^{*}_{on} and k_{off} in the case of anisotropic diffusion were comparable to those reported for the case of isotropic diffusion (data not shown). In

Figures 5.7g-i, the intersection of the values of ε in estimating the experimental parameters $tr(\boldsymbol{D})$, D_{xy}, k^*_{on} and k_{off} is reported. For all the anisotropic cases investigated, ε was ~3% for most values of k_{off} (ranging from 10^{-3} to 10^{1} s^{-1}) and k^*_{on} (ranging from 10^{-3} to 10^{2} s^{-1}).

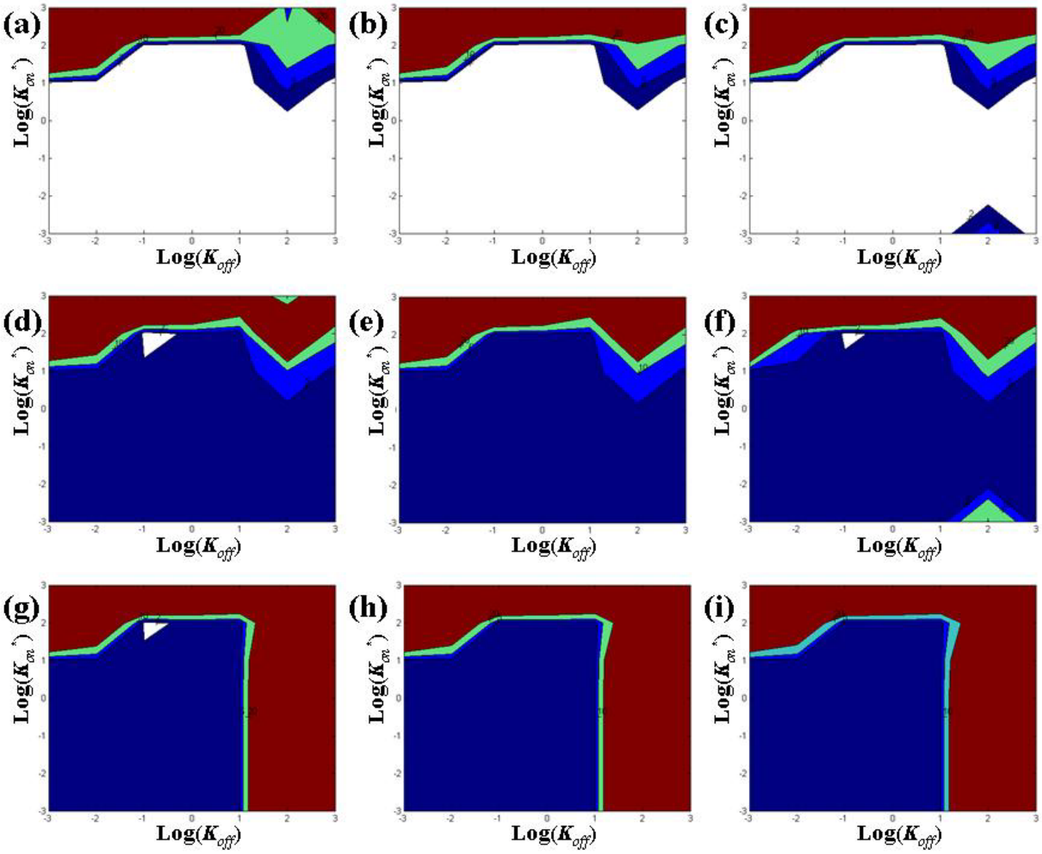

5.7. Effect of anisotropic ratio (D'_{xx}/D'_{yy}) on the accuracy of the method in estimating the experimental parameters: the values of ε are reported. Determination of $tr(\boldsymbol{D})$: **(a)** $D'_{xx}/D'_{yy} = 1.5$; **(b)** $D'_{xx}/D'_{yy} = 2$; **(c)** $D'_{xx}/D'_{yy} = 3$. Determination of D_{xy}: **(d)** $D'_{xx}/D'_{yy} = 1.5$; **(e)** $D'_{xx}/D'_{yy} = 2$; **(f)** $D'_{xx}/D'_{yy} = 3$. Intersection of the relative errors for determining $tr(\boldsymbol{D})$, D_{xy}, λ, and μ: **(g)** $D'_{xx}/D'_{yy} =1.5$; **(h)** $D'_{xx}/D'_{yy} = 2$; **(i)** $D'_{xx}/D'_{yy} = 3$. For all the cases reported in this figure, tr($\boldsymbol{D}$)= 10^{-6} cm^2s^{-1}, and $\theta = 45°$.

5.4.2 FRAP experiments

Transport of DAF in bovine coccygeal AF was characterized by binding interactions with the ECM of AF. The value of k^*_{on} (0.12±0.04 s^{-1}) was significantly larger than k_{off} (0.07±0.01 s^{-1}) for a total of 16 tests (2 tests on each specimen, *t*-test, $p<0.05$). The values of DAF diffusivity in axial (D_{axi} = 3.41±0.93x$10^{-7}cm^2s^{-1}$) and radial (D_{rad} = 2.43±0.84x$10^{-7}cm^2s^{-1}$) directions were also statistically different ($p<0.05$). A summary of the results is reported in Table 5.1.

n	D_{axi}	D_{rad}	k^*_{on}	k_{off}
16	3.41±0.93	2.43±0.84	0.12±0.04	0.07±0.01

Table 5.1. Anisotropic diffusivities (D x $10^7cm^2s^{-1}$) and reaction rates (s^{-1}) in bovine AF.

5.5 Discussion

A new FRAP approach for the simultaneous determination of solute anisotropic diffusivity and binding reaction rates in a biological tissue has been presented. In this new method, multiple sets of video-FRAP images, obtained at different sizes of the bleach spot, are simultaneously analyzed to yield the components of $\boldsymbol{D}$ and the binding and unbinding reaction rates k^*_{on} and k_{off}.

The new method was validated by computer simulated FRAP tests, and then applied to the simultaneous determination of the diffusion-reaction parameters of a cationic solute, DAF, in bovine coccygeal AF. Experimental results showed that DAF developed binding interactions with ECM of AF. These findings are in agreement with previous studies reporting binding of cationic solutes in articular cartilage,[3;93] likely due to the presence of negatively charged glycosaminoglycans in the ECM of the tissue.[93] It has been also found that diffusion of DAF is anisotropic, with D_{axi}/D_{rad} ~1.35, see Table 1. The same anisotropic ratio was reported in the previous studies on fluorescein (332 Da) diffusion in bovine AF.[192;194]

Numerical simulations indicated that the choice of d significantly affects the accuracy of the method for determining D: less accurate results were obtained when $d = 4$ μm was used, see Figures 5.3a-c. This was expected since the characteristic diffusion time depends on the square of d, see Equation (5.9). However, it should be noted that for some values of the binding and unbinding reaction rates, the accuracy of the method was not sensitive to the choice of size of the bleach spot. This was found, for instance, for both k^*_{on} and k_{off} varying from 10^{-3} to 10^{-1} s^{-1}. Within this range of parameters, diffusive-reactive fluorescence recovery was mainly governed by reaction (Da<<1 and R~1, see section 5.2.2.3), and consequently insensitive to the dimension of the bleach spot. Similar findings have been reported in a previous study.[185] Additionally, the accuracy of the technique was found to be independent from d as well for most of the couples k^*_{on} and k_{off} such that R<<1 (case of pure diffuse transport, see Section 5.2.2.1).

For all the anisotropic cases investigated, the values of ε in estimating $tr(\boldsymbol{D})$ were comparable to those generated in determining D in the case of isotropic diffusion. However, the accuracy of the technique in analyzing the FRAP data in the case of anisotropic diffusion was lower than that obtained in the case of isotropic diffusion. This was mainly due to the error generated in estimating D_{xy}, see Figure 5.7d-f.

The simultaneous analysis of multiple FRAP experiments, obtained at different values of d, significantly improved the accuracy of the method, see Figure 5.6. This strategy was especially efficient for improving the accuracy in determining k^*_{on} and k_{off}, see Figure 5.4 and 5.5. When the bi-exponential Equation (5.27) is used to analyze FRAP data, the set of parameters which provide a good curve-fitting may be not unique. This may lead to an erroneous estimation of D, k^*_{on}, and k_{off} during data analysis. In a previous work, Sprague et al. (2004), using a different bi-exponential model for data analysis of simulated fluorescence recovery data, also observed that accurate curve-fitting was achieved only when the initial guess parameters were equal to the true values.[185] The results of this study indicate that simultaneous analysis of multiple FRAP experiments significantly improve the uniqueness of the experimental parameters of curve-fitting. This is likely due to the fact that different fluorescence recovery regimes (different values of Da), characterized by the same value of D, k^*_{on}, and k_{off}, are simultaneously evaluated.

The new technique proved to be accurate for a wide range of parameters used in this study. However, the accuracy of the method reduced when k^*_{on} was larger than 100 s^{-1} and when k_{off} was larger than 10 s^{-1}, see Figure 5.6d. For all the values of d used in this study, values of k^*_{on} larger than 100 s^{-1} characterized a fluorescence recovery governed by effective diffusion (Da>>1, see Section 5.2.2.2). In this case, the use of multiple analyses of FRAP experiments did not improve the uniqueness of the curve-fitting parameters, and the accuracy of the model was affected. Additionally, when k_{off} was larger than 10 s^{-1} (and k^*_{on} significantly smaller than k_{off}), fluorescence recovery was governed by pure diffusion (R<<1, see Section 5.2.2.1). In this case, the binding reaction rates did not influence fluorescence recovery. As a consequence, in analyzing pure diffusive FRAP tests, the curve-fitting values of k^*_{on}, and k_{off} are not unique. The numerical results indicated that the low accuracy of the method in the case of pure diffusion was due to the error in determining the binding and unbinding rates, and not the diffusion coefficient (compare Figures 5.3d, 5.4d, and 5.5d).

5.6 Summary

A new method for the simultaneous determination of solute anisotropic diffusivity and binding reaction rates has been presented. The new technique is based on Fourier analysis of FRAP images. Numerical simulated FRAP experiments have been used to evaluate the sensitivity and the robustness of the method to experimental parameters, such as reaction rates of binding and unbinding, anisotropic ratio of the principal components of the diffusion tensor, and initial dimension of the bleached spot. Simultaneous analysis of multiple FRAP tests significantly enhances the robustness of the new technique.

Finally, the method has been successfully applied to the characterization of binding interactions of a cationic solute with the ECM of IVD. The experimental results indicate that DAF develops binding interactions with the ECM of bovine AF. Although DAF does not represent a physiologically relevant molecule, the findings of this study added new knowledge on the transport and the binding interactions of cationic solutes in IVD. In future studies, the new FRAP technique hereby developed could be applied to the investigation of binding interactions between more physiologically relevant solutes (i.e., growth factors) and the ECM of biological tissues or tissue engineered constructs.

Chapter 6: FINITE ELEMENT ANALYSIS OF SOLUTE TRANSPORT IN CARTILAGINOUS TISSUES: EFFECT OF MECHANICAL LOADING ON DIFFUSION, CONVECTION, AND BINDING REACTIONS

6.1 Introductory remarks

Transport of solutes in cartilaginous tissues involves many coupled electro-chemical and mechanical phenomena. In Chapter 2, a theoretical framework, based on the mixture theory, was developed for describing solute transport and binding reactions in charged hydrated soft tissues. Due to the high non-linearity of the set of the governing equations, it is not possible, in general, to provide analytical solutions to specific problems. In this chapter, a finite element model, based on the theoretical framework developed in Chapter 2, was used for analyzing solute diffusive-convective-reactive transport in cartilaginous tissues. More specifically, this numerical framework was applied to model solute transport and binding reactions in both articular cartilage and intervertebral disc. The insulin-like growth factor-I (IGF-I) was chosen as a reacting solute, since it has been reported that this molecule binds to the extracellular matrix of cartilaginous tissues.[12;15;54] The kinetics of IGF-I transport and binding were investigated in the case of free diffusion (i.e., absence of mechanical load on the tissue), and in the case of static and cyclic axial compression of the tissue. The results were compared to those reported in literature.[56;136;215;222]

6.2 Finite element formulation

The cartilaginous tissue was modeled as a mixture composed by an intrinsically incompressible elastic solid, water, an electrolyte (NaCl), and a non-charged solute (i.e., IGF-I) able to react with binding sites (i.e., IGF binding proteins) present in the solid matrix (see Section 2.2). Based on the balance of the linear momentum of the mixture, the conservation of mass of each of its constituents, the electroneutrality condition, and the law of mass action, the governing equations for the mixture and its components were derived, see Equations (2.12), (2.29), (2.30), (2.33), (2.34), and (2.35) in Section 2.2.8. Consistent with previous studies,[86;87;189;216-219] in the formulation of the finite element model presented in this chapter, the primary degrees of freedom were the solid matrix displacement $\boldsymbol{u}$, and the modified electro-chemical potentials of the fluid, ions, and solutes ε^{α} ($\alpha = w, +, -, f, b$), see Appendix A.2 for details.

6.2.1 Constitutive equations

From the equivalent formulation of the mixture theory (see Appendix A.2), a constitutive equation for the solid stress was provided, see Equation (A.17). Due to the lack of experimental data relative to the chemical stress (T_c), and the inter-phase coupling coefficient (B_w), in this model, these two terms were neglected. Thus, the constitutive equation adopted for the solid stress was:

$$\sigma = -[RT\alpha^{w} + RT\Phi(c^{+} + c^{-} + c^{f}) - p_{o}] + \alpha\nabla \cdot \boldsymbol{u} + \mu[\nabla \boldsymbol{u} + (\nabla \boldsymbol{u})^{T}] \quad (6.1)$$

In addition, the following constitutive equation was used for solutes diffusivity:[66]

$$\frac{D}{D_o} = exp[-a_1(r_s/\sqrt{k})^{b_1}] , \quad (6.2)$$

where D_o is the solute diffusion coefficient in water solution, a_1 and b_1 are two positive parameters depending on the morphology of the tissue, r_s is the hydrodynamic radius of the solute, and k is the Darcy permeability which is related to the hydraulic permeability (K) by $k = K\eta$ (where η is the fluid viscosity). The Darcy permeability was considered to be dependent on the porosity of the tissue (ϕ^w). Its constitutive equation was:[65]

$$k = a_2 \left(\frac{\alpha^w}{1 - \alpha^w} \right)^{b_2}, \qquad (6.3)$$

where a_2 and b_2 are two positive parameters, also dependent on the structure of the tissue. Note that, the porosity of the tissue can be related to tissue deformation according to the following relationship:[61;114]

$$\phi^w = \frac{\phi_o^w + e}{1 + e}, \qquad (6.4)$$

where the dilatation e is related to the strain tensor of the solid matrix $\boldsymbol{E}$ by $e = \mathrm{tr}(\boldsymbol{E})$; $\phi^w{}_o$ is the interstitial fluid volume fraction at reference configuration (i.e., at $e = 0$). In this framework, the configuration in which the tissue is equilibrated in a solution with infinite salt concentration (hypertonic solution) will be chosen as the reference configuration. Therefore, in this model, both solute diffusivities and Darcy permeability were strain dependent.

Considering the set of governing equations (2.12), (2.29), (2.30), (2.33), (2.34), and (2.35), combined with the above set of constitutive equations and appropriate boundary and initial conditions, solute diffusive-convective-reactive transport in cartilaginous tissues can be analyzed by using the finite element model presented in the following.

6.2.2 Numerical implementation

In implementing the finite element model, the governing equations (2.12), (2.29), (2.30), (2.33), (2.34), and (2.35) were non-dimensionalized by the introduction of the following non-dimensional quantities:[85-87]

$$x_r = \frac{x}{h},\ \boldsymbol{u}_r = \frac{\boldsymbol{u}}{h},\ \boldsymbol{v}_r^s = \frac{\boldsymbol{v}^s}{H_A k_0/h},\ t_r = \frac{t}{h^2 / H_A k_0},\ D_r^{+,-,f} = \frac{D^{+,-,f}}{H_A k_0},\ c_r^{+,-,F} = \frac{c^{+,-,F}}{c*},$$

$$c_r^{f,b,bs} = \frac{c^{f,b,bs}}{c^f *},\ \sigma_r = \frac{\sigma}{RTc*},\ \alpha_r^{w,+,-} = \frac{\alpha^{w,+,-}}{c*},\ \alpha_r^{f,b} = \frac{\alpha^{f,b}}{c^f *},\ \boldsymbol{J}_r^w = \frac{\boldsymbol{J}^w}{H_A k_0/h},$$

$$\boldsymbol{J}_r^{+,-} = \frac{\boldsymbol{J}^{+,-}}{H_A k_0 c*/h},\ \boldsymbol{J}_r^f = \frac{\boldsymbol{J}^f}{H_A k_0 c^f */h},\ k_{on_r} = \frac{k_{on} h^2 c^f *}{H_A k_0},\quad k_{off_r} = \frac{k_{off} h^2}{H_A k_0}, \tag{6.5}$$

where x is the generic spatial coordinate, H_A is aggregate modulus ($H_A = \lambda + 2\mu$), k_0 is the basic scale of permeability, h is the basic scale of height or length, $c*$ and c^f* are the concentrations of electrolytes and free solute at the boundary of the tissue, respectively.

The finite element formulation was obtained using the Galerkin weighted residual method.[189] The weak formulation of the governing equations is reported in Appendix A.3.1, see Equations (A.28-33). Note that, the numerical studies carried out in this chapter simulated solute transport in cylindrical samples of articular cartilage or intervertebral disc. Moreover, mechanical deformation was applied in the axial direction of the cylindrical samples. Therefore, the more general finite element formulation represented by Equations (A.28-33) was specialized for an axisymmetric coordinate system to yield Equations (A.44-50), see Appendix A.3.2.

The commercial finite element software COMSOL (COMSOL® 3.2, COMSOL Inc., Burlington, MA) was used to numerically solve the governing equations (A.44-50). At each computational time step, the solid displacement and the modified electrochemical potentials of water, ions, free solute, and bound solute were calculated.

6.3 Solute transport and binding interactions in cartilaginous tissue

6.3.1 Background

Articular cartilage is a connective tissue whose functions are to reduce static contact stresses on the bones, lubricate the joints, and to absorb mechanical stress during physiological dynamic loading.[132;142]

The ability of cartilage in withstanding mechanical loading relies on the structural integrity of its extracellular matrix (ECM). The integrity of ECM requires constant remodeling and restoration, which is achieved through the biosynthetic activity of the chondtocytes.[58] The production and replacement of collagen, glycoproteins, and other ECM components requires the supply of nutrients and growth factors.[100] Among all the growth factors, insulin-like growth factors (IFGs) seem to have a crucial role in cartilage maintenance.[126] It has been reported that IGFs, binding on surface receptors of chondocytes, not only promote synthesis of ECM, but also act as inhibitor for catabolic agents which cause tissue degeneration.[140]

Since cartilage is avascular, its nourishment is provided by the synovial fluid and the vascular network surrounding the tissue. [86;132]A major transport mechanism for solutes in cartilage is diffusion. However, since in normal physiological conditions cartilage is subjected to cyclic compressive deformation, solute transport also occurs via convective flux induced by dynamic mechanical loading. Several studies have been performed in order to investigate on the contribution of advection to solute transport in cartilaginous tissues. It has been found that mechanically induced solute convection enhances fluid transport in the tissue.[56;136;215;216;224;225] In addition, some solutes (e.g., IGFs), while transported within the cartilaginous tissue, interact with binding proteins present in the extracellular matrix.[12;15;55;141] The binding interactions of IGFs with the extracellular matrix of cartilage have been investigated experimentally and theoretically in the case of static diffusion (i.e., no mechanical stimulation),[12;55] and in the case of dynamic compression of the tissue.[222;223] In particular, Zhang et al. (2007)[222] developed a numerical model, based on the biphasic theory,[144] which described the transport and binding reactions of IGF-I in articular cartilage in the presence of cyclic compressive deformations. However, in their analysis, Zhang and co-workers only provided quantitative information on the total amount of IGF-I present in the tissue (i.e., average IGF-I uptake ratio), and did not report the distribution of the solute within the tissue.[222]

The objective of this preliminary study is to provide a more detailed picture on solute transport and binding interactions in cartilaginous tissues, gaining additional insights on the effect of binding on molecular distribution within the tissue.

In order to achieve this goal, a numerical model, based on the weak formulation of the mixture theory presented in the previous section, is used. The numerical results are presented in light of the effects of mechanical stimulation (i.e., frequency and amplitude of cyclic compressive deformation), the concentration of binding sites in the tissue, and the values of the characteristic binding rate constants on solute transport within a cartilage explant. The solute modeled in this study is IGF-I, since most of its transport and binding properties are available in the literature.

6.3.2 Methods

In this study, a homogeneous cylindrical disc of cartilage (1 mm radius and 1 mm thickness) is axially compressed by a rigid frictionless impermeable platen, see Figure 6.1(a). Initially, the tissue is in equilibrium with a bathing solution of 0.15 M NaCl (at $t = 0$). Then, an uncharged solute, able to develop binding interactions with the extracellular matrix of the cartilage (IGF-I), is gradually introduced in the bathing solution. The concentration of the solute in the bathing solution is linearly increased until reaching a prescribed value (at $t = t_1$), see Figure 6.1(c). Immediately after, a sinusoidal compressive displacement is applied to the tissue, see Figure 6.1(d). During compression, the tissue is assumed to be perfectly adhesive to the platens.

For this 2D problem of interest, due to the symmetry with respect to $r = 0$ and $z = 0$, only the right upper quadrant of the sample is modeled, see Figure 6.1(b). In the following, the initial and boundary conditions of the problem are provided.

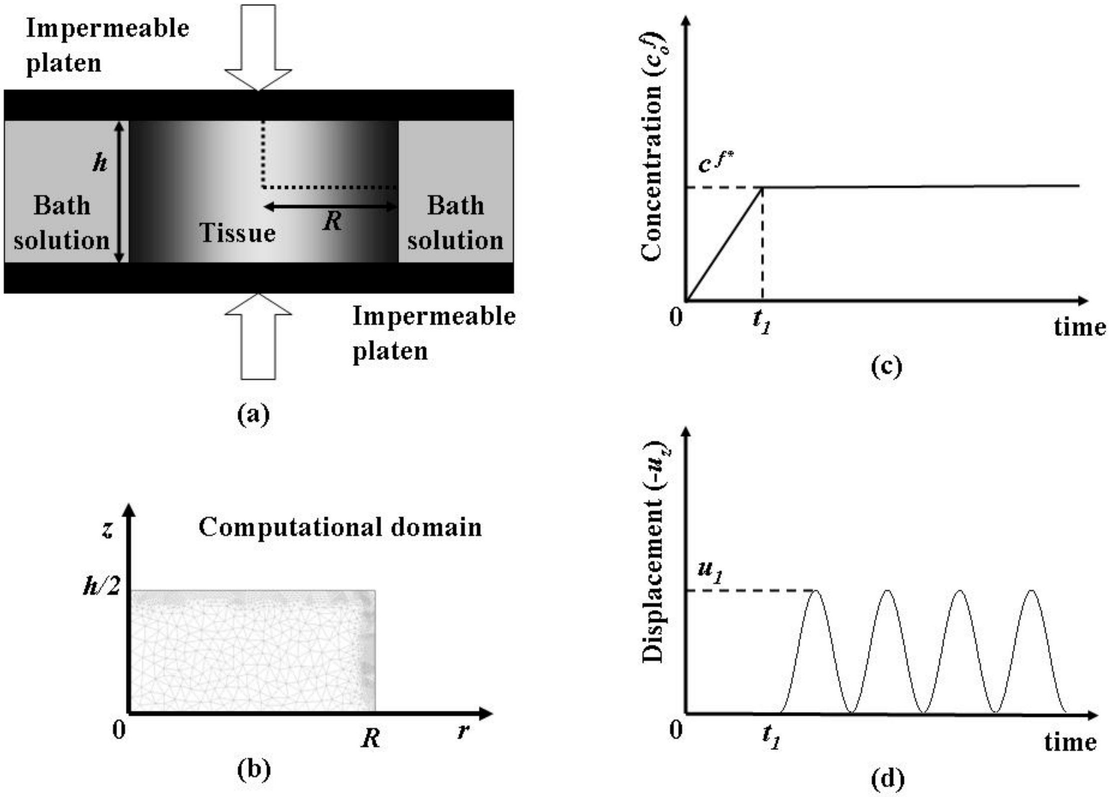

Figure 6.1 Schematic of dynamic unconfined compression of a cartilage explant. (a) A cylindrical sample (1 mm thickness and 1 mm radius) is confined by two impermeable rigid frictionless platens and surrounded by a bath solution containing 0.15 M NaCl. (b) Due to the geometrical symmetry of the problem of interest, only upper quadrant of the sample is modeled with a mesh of 2689 quadratic Lagrange triangular elements. (c) IGF-I is gradually introduced in the bath solution, until its concentration reaches the value c^{f*} ($t = t_1$). (d) At $t = t_1$, a sinusoidal compression (u_1 peak-to-peak dynamic displacement) is applied to the tissue.

6.3.2.1 Initial conditions

Let the superscript (*) indicate the quantities in the bath solution. The initial condition of the problem are:[114;189;215]

$$\boldsymbol{u} = 0\,,\ \varepsilon^{w} = \varepsilon^{w^*},\ \varepsilon^{+} = \varepsilon^{+^*},\ \varepsilon^{-} = \varepsilon^{-^*},\ \varepsilon^{f} = 0,\ \varepsilon^{b} = 0 \qquad (6.6)$$

Note that, the electrochemical potential of the water in the bath solution is proportional to the concentration (c^*) of both Na^+ and Cl^-:

$$\alpha^{w*} = -2\Phi^* c^*, \tag{6.7}$$

where Φ^* is the osmotic coefficient in the bath solution. By combining the above equation with Equation (6.6) and the definition of the modified electrochemical potential of the fluid phase (see Equation (A.12) in Appendix A.2), the expression of the pressure at reference configuration (i.e., pre-stress of the tissue) is given:

$$p_o = RT[\Phi(c_o^+ + c_o^-) - 2\Phi^* c^*], \tag{6.8}$$

where ${c^+}_o$ and ${c^-}_o$ are the initial concentrations of ions in the tissue at equilibrium with the bath solution.

6.3.2.2 Boundary conditions

The symmetry of the computational domain requires that:

$$r = 0: \quad u_r = \alpha_{rz} = 0, \quad J_r^w = J_r^+ = J_r^- = J_r^f = 0; \tag{6.9}$$

$$z = 0: \quad u_z = \alpha_{rz} = 0, \quad J_z^w = J_z^+ = J_z^- = J_z^f = 0; \tag{6.10}$$

At the unconfined boundary of the cartilage we have:

$$r = R\text{:}\ \alpha_{rr} = \alpha_{rz} = 0,\ \varepsilon^{w} = \varepsilon^{w^*}, \varepsilon^{+} = \varepsilon^{+^*}, \varepsilon^{-} = \varepsilon^{-^*},\ \alpha^{f} = \alpha^{f^*}(t), \qquad (6.11)$$

where (see Figure 6.1)

$$\alpha^{f^*}(t) = \frac{\alpha_f^* c^{f^*}}{t_1} t \qquad \text{for } t < t_1, \qquad (6.12a)$$

$$\alpha^{f^*}(t) = \alpha_f^* c^{f^*} \qquad \text{for } t \leq t_1. \qquad (6.12b)$$

In Equations (6.12), c^{f*} is the concentration of IGF-I in the bath solution, and γ_f^* its activity coefficient. The sinusoidal strain is applied in the axial direction by a rigid impermeable frictionless platen. Consequently, we have:

$$z = h/2\text{:}\ u_z = u(t),\ u_r = 0,\ J_z^w = J_z^+ = J_z^- = J_z^f = J_z^b = 0; \qquad (6.13)$$

where (see Figure 6.1)

$$u(t) = \frac{u_1}{2}\{1 - cos[2\pi f(t - t_1)]\} \cdot H(t - t_1). \qquad (6.14)$$

In the above equation, $H(t-t_1)$ is the Heaviside step function satisfying $H = 0$ for $t < t_1$ and $H = 1$ for $t \geq t_1$; f is the loading frequency; u_1 is amplitude of the dynamic compression.

Note that, at all the boundaries of the tissue, the concentration bound IGF-I must satisfy the law of mass action:

$$\frac{d(c^b)}{dt} = k_{on}(c_o^{bs} - c^b)c^f - k_{off}c^b . \qquad (6.15)$$

6.3.2.3 Numerical implementation

The governing equations (A.44-50), together with the initial and boundary conditions (see Equations (6.6-15)), were solved using a finite element method package (COMSOL® 3.2, COMSOL Inc., Burlington, MA). A mesh of 2689 quadratic Lagrange triangular elements was used in the simulations. Note that the mesh was refined near the loading platen and the radial edge of the sample. The implicit solver of COMSOL® (based on the implicit Euler backward scheme) was used for the simulations. The convergence criterion for the solution was the relative error tolerance of less than 10^{-3}. In the simulations, the maximum time-step varied from 0.3125 s (for a sinusoidal compression at frequency = 0.1 Hz) to 31.25 s (for a sinusoidal compression at frequency = 10^{-3} Hz). These maximum time steps can guarantee at least 32 time steps per cycle. Although at least 32 time steps per cycle were taken in the computation, only 4 points per cycle (with uniform time intervals) were output in order to avoid the overflow of the output data structure.

The following parameters were used in the simulations: temperature was set to T = 298K, the electrolyte concentration in the bath solution was c* = 0.15 M NaCl, the initial water content of cartilage was $\phi^w{}_o$ = 0.8,[16;143] the initial fixed charge density $c^F{}_o$ =

0.2 mEq/ml,[146] and the Lamé coefficients λ and μ were 0.1 and 0.2 MPa,[146] so that the aggregate modulus was H_A = 0.5 Mpa. The reference hydraulic permeability for non-dimensionalization was $k_o = 2\cdot10^{-15}$ m^{4}N^{-1}s^{-1},[143] and the coefficients a_2 and b_2 used in constitutive equation for the strain dependent Darcy permeability (see Equation (6.5)) were 0.00339 nm^2 and 3.24,[65] respectively. The experimental coefficients used in the constitutive equation for the strain dependent solute diffusivity (see Equation (6.4)) were a_1 = 1.25, and b_1 = 0.681.[66] The hydrodynamic radii of the ions were r^+_s = 0.197 nm and r^-_s = 0.142 nm,[217] and their diffusivities in water solution were $D^+_o = 1.28\cdot10^{-9}$ m^2/s, and $D^-_o = 1.77\cdot10^{-9}$ m^2/s.[87;216] The binding solute considered in this study was IGF-I, whose diffusion coefficient in water solution is $D^f_o = 3.23\cdot10^{-11}$ m^2/s,[16;172] and its hydrodynamic radius is r_s = 1.72 nm.[112] It should be noted that, in *vivo*, IGF-I may interact with various types of binding proteins, as well as cartilage cell surface receptors.[115] For the sake of simplicity, in this study, only the interactions between IGF-I and IGFBP-3 binding protein are taken into account, since IGFBP-3 is the most abundant binding protein and IGF-I is mostly found in a complex with IGFBP-3.[34] The rates of association and dissociation of IGF-I and IGFBP-3 used in this study were $k_{on} = 3.67\cdot10^5$ M^{-1}s^{-1}, and k_{off} = 0.001 s^{-1}.[31] Previous studies suggested that the concentration of IGFBP-3 in bovine cartilage varies from 30 to 150 nM.[141] Consistently, in this study, the initial concentration of binding sites (c^{bs}_o) had the same range of variation. In addition, it was assumed that Φ = 1, and, for any solute, $\gamma_\alpha/\gamma_\alpha^* = 1$ (α = +, -, f, b).

In this study, the loading frequencies (f) of the dynamic compression varied from 0.001 Hz to 0.1 Hz. The ramp time for the free solute concentration in the bath solution (c^{f*}) was the half of the period of the mechanical loading (e.g., t_1 = 5 s when f = 0.1 Hz).

For simulated cases of free diffusion (i.e., no mechanical loading), t_1 = 50 s. Moreover, the amplitude of the dynamic compression (u_1) varied from 0.00625 to 0.025 mm (corresponding to 2.5 to 10% peak-to-peak dynamic strain).

6.3.3 Results and discussion

Hereby, the effect of binding on solute transport is investigated in the cases of free diffusion (i.e., no deformation of the tissue), and diffusion with cyclic deformation. The results are compared to those obtained when binding interactions are neglected. Note that, in this study, solute concentrations are normalized with respect to the solute concentration of the bath solution surrounding the tissue (c^{f*}). In addition, some of the quantitative results are also expressed in terms of average free solute uptake ratio (R_{free}), average bound solute uptake ratio (R_{bound}), and average total solute uptake ratio (R_{tot}), defined as:

$$R_{free} = \frac{\int_0^{h/2}\int_0^{R} 2\pi r c_r^f \, dr dz}{\int_0^{h/2}\int_0^{R} 2\pi r \, dr dz}, \qquad (6.16)$$

$$R_{bound} = \frac{\int_0^{h/2}\int_0^{R} 2\pi r c_r^b \, dr dz}{\int_0^{h/2}\int_0^{R} 2\pi r \, dr dz}, \qquad (6.17)$$

$$R_{tot} = R_{free} + R_{bound}. \qquad (6.18)$$

6.3.3.1 Free diffusion

The average total IGF-I uptake ratio (R_{tot}) after 48 hours of free diffusion was evaluated at several concentrations of IGF-I in the bath solution (c^{f*}). In the simulations, three different initial concentration of binding sites (IGFBP-3) were investigates: $c^{bs}{}_{o}$ = 30, 45, and 60 nM. The results were compared to the average uptake ratio of IGF-I in the case of pure diffusion (i.e., when binding effects are neglected). The effect of binding interactions was to increase the IGF-I uptake with respect to the case of pure diffusion, see Figure 6.2. This effect was significant for low concentrations of IGF-I in the bath solution. In particular, the highest values of R_{tot} were found when the concentration of IGFBP-3 was the highest. In contrast, for high values of c^{f*} (c^{f*} > 100 nM), the effect of binding was negligible for all the values of $c^{bs}{}_{o}$ investigated. These results are consistent with previous experimental observations and theoretical studies.[55;222] When the solute concentration of the bath solution is significantly higher than $c^{bs}{}_{o}$, during diffusion, all the binding sites present in the tissue are saturated, and IGF-I transport is essentially diffusive. However, in normal human synovial fluid, the concentration of IGF-I is very low (~6.5 nM).[171] Therefore, in modeling solute transport, it is crucial to include binding effects.

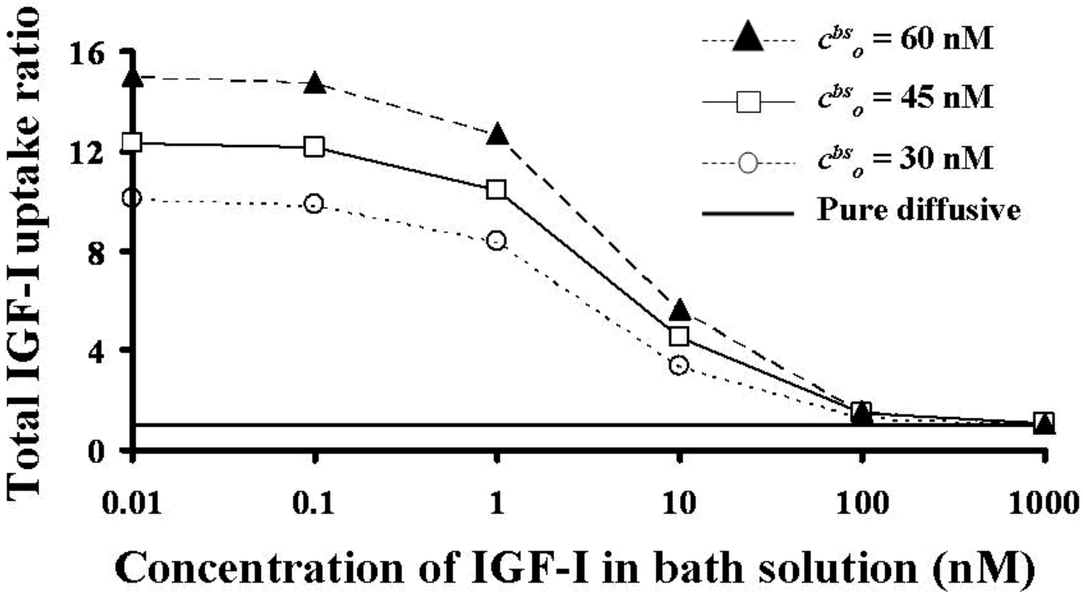

Figure 6.2 Comparison of total IGF-I uptake ratio as a function of the IGF-I concentration in the bath solution and parametric with the concentration of IGFBP-3 within tissue after 48 hours of free diffusion

The distribution of solutes within the tissue during free diffusion was also investigated. Figure 6.3 reports the profiles of normalized concentration of a binding solute (free fraction, bound fraction, and total concentration). The concentration distribution of a solute that does not develop binding interactions is also shown. Transport of solute across the cartilage disc is dramatically slowed by the effect of binding interactions between the solute and the binding sites within the tissue. After six hours of free diffusion, the penetration of the binding solute reaches only the 30% of the disc. In contrast, the non-reacting solute penetrates the entire tissue, with a normalized concentration of $2{\cdot}10^{-3}$ at $r = 0$. These findings are in agreement with experimental observations reported by Garcia et al. (2003).[55]

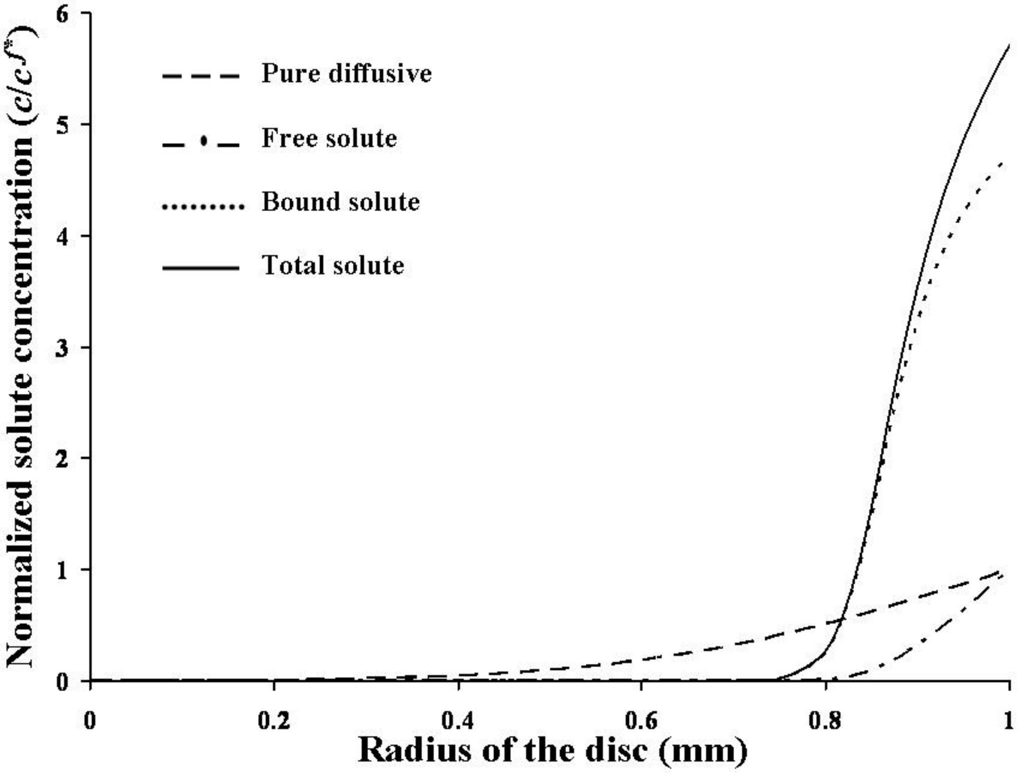

Figure 6.3 Profiles of IGF-I concentration within the cartilage disc after 6 hours of free diffusion at $z = 0$. The solute concentrations are normalized with respect to the IGF-I concentration in the bath solution (c^{f*}). For the case reported in this figure, $c^{f*} = 10$ nM, and the initial concentration of the binding sites in the tissue was $c^{bs}{}_{o} = 60$ nM.

6.3.3.2 Effect of cyclic deformation

In normal cartilage, as well as in other avascular tissues, convection is potentially an important transport mechanism. Herein, the effect of solute convection, induced by cyclic compression of the tissue, is investigated.

The effect of the bath concentration (c^{f*}) on the uptake of IGF-I in the tissue under dynamic compression was studied. Figure 6.4 reports the total IGF-I uptake over a time frame of 6 hours of cyclic compression at $f = 0.01$ Hz with a peak-to-peak strain amplitude $u_1 = 5\%$. The data are normalized with respect to the IGF-I uptake in the case of free diffusion. Under the same dynamic loading conditions, lower bath solute concentration results in higher percent increase of solute uptake ratio (R_{tot}), when compared to the free diffusion case. Thus, the enhanced solute transport due to dynamic compression is most significant when c^{f*} is the lowest. However, for all the values of bath solute concentration, the enhancement due to dynamic loading fades with time. This trend of variation is consistent with previous findings reported in studies investigating solute transport in absence of binding reactions.[56]

The effects of frequency of stimulation and magnitude of compression on solute uptake were investigated. Figure 6.5 shows the increase of free, bound, and total IGF-I average uptake ratios after 30 minutes of cyclic compression for loading frequencies raging from 0.001 to 0.1 Hz. Data are normalized with respect to the corresponding average uptake ratios for the case of free diffusion. Consistent with previous studies,[56;136;222] the increase of loading frequency enhances solute transport within the tissue. In particular, it was found that the free pool of IGF-I present in the tissue was the most dramatically sensitive to the value of the frequency.

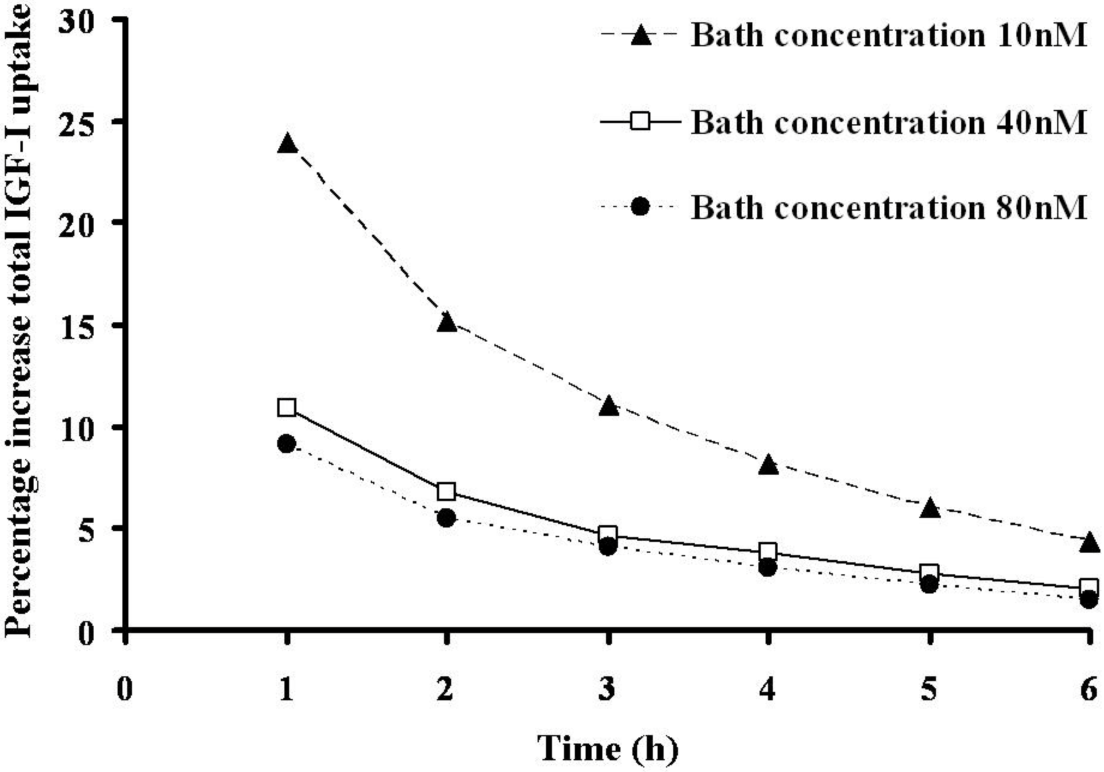

Figure 6.4 Effect of cyclic compression on total IGF-I uptake at several values of IGF-I concentrations in the bath solution. Data are normalized with respect to the case of free diffusion. For the all cases reported in this figure, the initial concentration of IGFBP-3 was c^{bs}_{o} = 50 nM, the frequency of dynamic compression was f = 0.01 Hz, and the peak-to-peak strain deformation was u_1 = 5%.

The magnitude of compressive strain also affected the percentage increase of solute uptake within the tissue. Figure 6.6 reports the percentage increase of free, bound and total IGF-I average uptake ratios in dynamic compression (f = 0.01 Hz) when u_1 = 2.5, 5, and 10%. Consistent with findings reported in previous studies,[56;136;222] the higher the magnitude of dynamic compression, the greater is the enhancement of solute uptake in the tissue. In particular, the most beneficial effects of increasing the strain amplitude are seen in the free pool of IGF-I. However, as expected,[56;222] the enhancement of dynamic compression reduces with time.

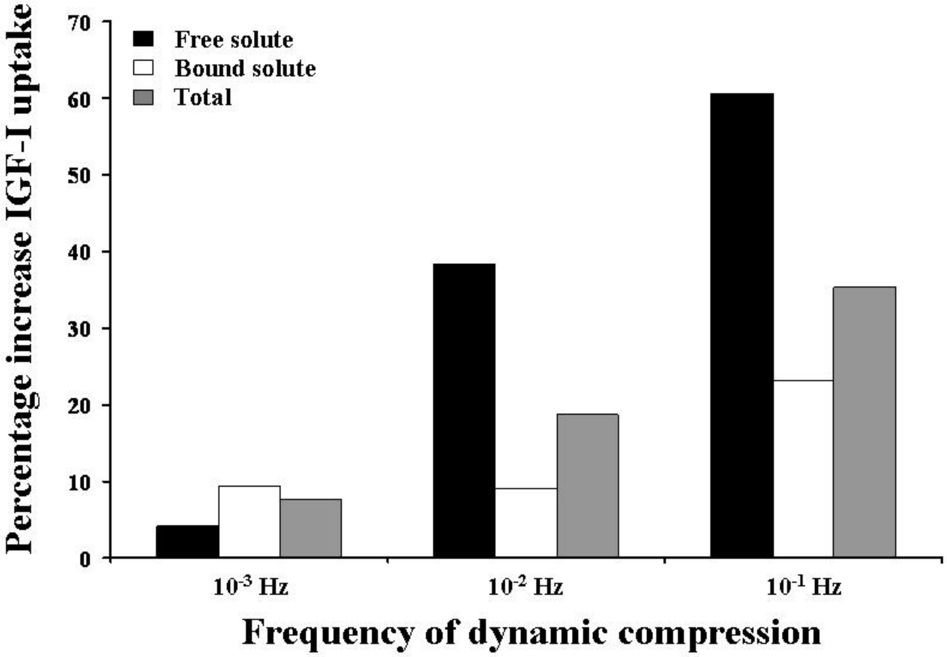

Figure 6.5 Effect of frequency of dynamic compression on IGF-I uptake after 30 minutes of stimulation. Data are normalized with respect to the case of free diffusion. For the all cases reported in this figure, the initial concentration of IGFBP-3 was c^{bs}_{o} = 50 nM, and the peak-to-peak strain deformation was u_1 = 5%.

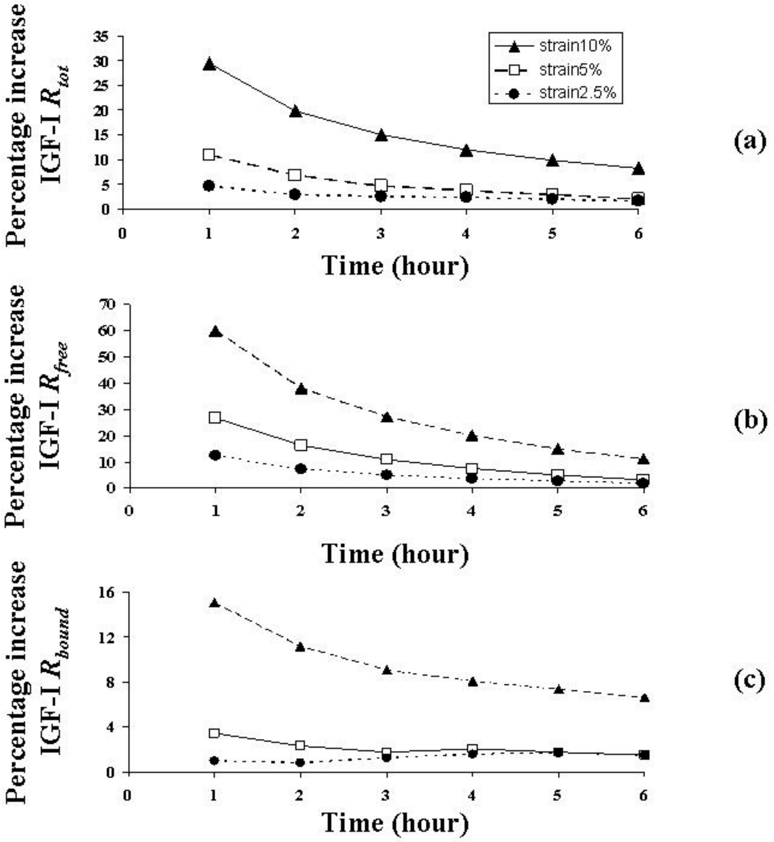

Figure 6.6 Effect of amplitude of dynamic compression on percentage increase of solute uptake. Data are normalized with respect to the solute uptake in case of free diffusion. (a) Percentage increase of total solute uptake. (b) Percentage increase of free solute uptake. (c) Percentage uptake of bound solute. For all the cases reported in the figure, the frequency of dynamic load was $f = 0.01$ Hz, the initial concentration of IFGBP-3 was $c^{bs}_{o} = 50$ nM, and the concentration of IGF-I in the bath solution was $c^{f*} = 40$ nM.

In this study, for the sake of simplicity, the only interaction between IGF-I and IGFBP-3 was investigated. However, in *vivo*, IGF-I can interact with various types of binding proteins.[115] In all these cases, the rates of binding reactions might be different from those for IGFBP-3. In order to investigate on the effect of the binding reaction rates on the transport of IGF-I in cartilage, the solute uptake in tissue was evaluated for different association rates (k_{on}), at various IGF-I concentrations in the bath solution. More specifically, three association rates were sampled: $k_{on}^{0} = 3.67\cdot10^{5}$ $M^{-1}s^{-1}$ (association rate for IGF-I and IGFBP-3 in articular cartilage[31]), $k_{on}^{1} = 0.1 \cdot k_{on}^{0}$, and $k_{on}^{2} = 10 \cdot k_{on}^{0}$. Figure 6.7 reports the free, bound, and total percentage increase in IGF-I average uptake ratio when tissue is stimulated for 30 minutes with a dynamic compression of $f = 0.01$ Hz with $u_1 = 5\%$. As in the previous cases reported, data are normalized with respect to the corresponding values in case of free diffusion. For low values of IGF-I concentration in the bath solution, the average solute uptake ratio dramatically increases with the association rate. This effect is more pronounced for the free pool of IGF-I molecules. However, when IGF-I concentration in the bath solution is high, the percentage increase of solute uptake is independent from the association rate. It should be also noted that, for the lowest value of the association rate (k_{on}^{1}), the percentage increase of solute uptake is independent from the IGF-I concentration in the bath solution. These results are in agreement with similar findings previously reported.[222]

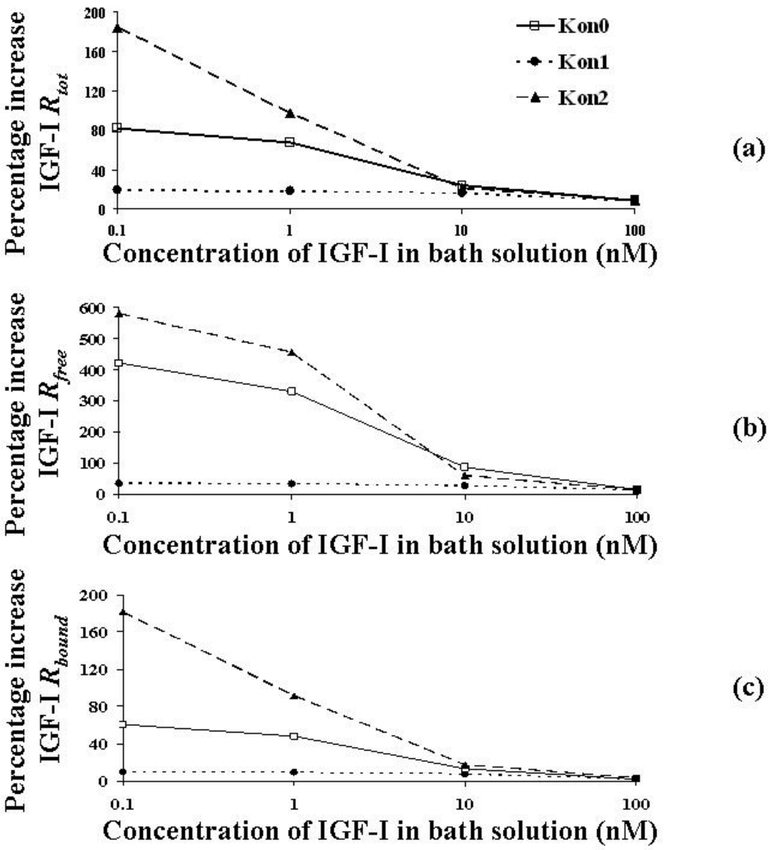

Figure 6.7 Effect of the binding association rate on percentage increase of IGF-I average uptake ratio after 30 minutes of dynamic compression. (a) Percentage increase of total solute uptake. (b) Percentage increase of free solute uptake. (c) Percentage uptake of bound solute. For all the cases reported in the figure, the frequency of dynamic compression was f = 0.01 Hz, the peak-to-peak strain deformation was u_1 = 5%, the initial concentration of binding protein was c^{bs}_{o} = 50 nM, and the rate of dissociation was k_{off} = 0.001 s^{-1}.

6.3.4 Conclusions

The objective of this study was to investigate the effect of binding interactions on solute transport in cartilaginous tissues. A finite element model, based on the mixture theory for charged hydrated soft tissues, was used to describe the coupled solute transport and electromechanical behavior of cartilage. More specifically, the uptake of solute and its distribution within the tissue were investigated for the case of free diffusion (i.e., no mechanical load applied to the tissue), and for the case of cyclic unconfined compression of a cartilage disc.

It was found that binding interactions significantly affect the solute uptake in the sample when the initial bath concentration of the solute is low compared to the concentrations of binding sites in the tissue. In contrast, when the concentration of the solute in the bath solution is significantly higher than the concentration of the binding proteins in the tissue, the effect of binding is negligible since all the binding sites in the sample are saturated.

Cyclic compression of the tissue generally increases the uptake of both free and bound solutes within the tissue. This effect is further enhanced when high loading frequencies (e.g., $f = 0.1$ Hz) and high amplitudes of compressive strain (e.g., $u_1 = 10\%$) are used. However, dynamic compression is only effective on a short time scale (e.g., $t <$ 6 hours), after than that the value of solute uptake is similar to that obtained for the case of free diffusion.

The profiles of concentration within the tissue of both a binding solute and a non-reacting solute were compared for the cases of free diffusion. When compared at the same time frame, the penetration into the tissue of the non-reacting solute was significantly deeper than that of the binding solute. It was concluded that, although binding increases the solute uptake in the sample, solute transport across the cartilage disc is slowed by the interactions with the binding sites present in the tissue.

6.4 Preliminary study on the binding effects on solute transport in IVD

6.4.1 Background

The intervertebral disc (IVD) is a structure that contributes to flexibility and load support in the spine. The continuous presence of a compressive load on the disc may compromise the integrity of the extracellular matrix of the tissue. Therefore, in order to accomplish with its structural function, this cartilaginous tissue undergoes a continuous turnover of its ECM.[58] New extracellular matrix is biosynthesized by disc cells, provided a sufficient amount of nutrients.[100]

Nutrients access the disc from the vascular network surrounding the tissue[74;153;200] (see Figure 1.5), and reach disc cells mainly by passive transport (i.e., diffusive transport).[74;104;131;199;200;203] However, due to the continuous compressive deformation of the disc, convective transport of nutrients, induced by fluid flow, also occurs.[49;75;137;155;168;200;203;217] In addition, during transport, some solutes (e.g., IGFs) bind to specific sites in the extracellular matrix of the cartilaginous tissue.[12;55]

Since determining the in vivo distribution of nutrients in human IVD is often invasive and difficult,[7] little is known on nutrient transport. Recently, several numerical models have been proposed to study transport of nutrients and metabolites (e.g., oxygen, glucose, and lactate) in IVD.[37;85-87;173;180-182;219]. These models focused on several aspects of solute transport in the disc: the determination of the distribution of nutrients and metabolites within the tissue;[37;173;180-182] the effect of mechanically induced fluid convective flow on solute transport;[219] [87]; the effect of compressive load on the metabolism of disc cells.[85] However, none of these models investigated the effect binding reactions on solute transport in IVD.

The objective of this preliminary study was to examine the effects of kinetics of binding reactions on solute transport in IVD. The finite element model presented in this chapter was applied to the study of transport of IGF-I in the disc under static compressive load. The averaged total IGF-I content and IGF-I concentration profiles in nucleus pulposus (NP) and annulus fibrosus (AF) were determined.

6.4.2 Methods

In this study, a human lumbar IVD is schematized as an axisymmetric object consisting of two anatomical regions (i.e., NP and AF), with dimensions similar to those reported in previous studies, see Figure 6.8a.[85;173;182] The NP is superiorly and inferiorly confined by perfectly permeable cartilage endplates (CEPs). In contrast, the AF is superiorly and inferiorly confined by perfectly impermeable vertebral bodies. At the CEPs and on the lateral (i.e., periannular) surface, IVD is in contact with a physiological solution containing 0.15 M of NaCl. In this study, it was assumed that, during transport, IGF-I only reacted with IGFBP-3.

In the simulations, two cases were investigated: absorption of IGF-I from the physiological solution; release of IGF-I from the disc to the surrounding physiological solution. In both cases, the effect of static compression on the kinetics of solute absorption and release was investigated. The results were compared to those obtained when the effect of binding interactions on IGF-I transport was neglected.

For this 2D problem of interest, due to the symmetry with respect to $r = 0$ and $z = 0$, only the right upper quadrant of IVD was modeled, see Figure 6.8(b). In the following, the initial and boundary conditions of the problem are provided.

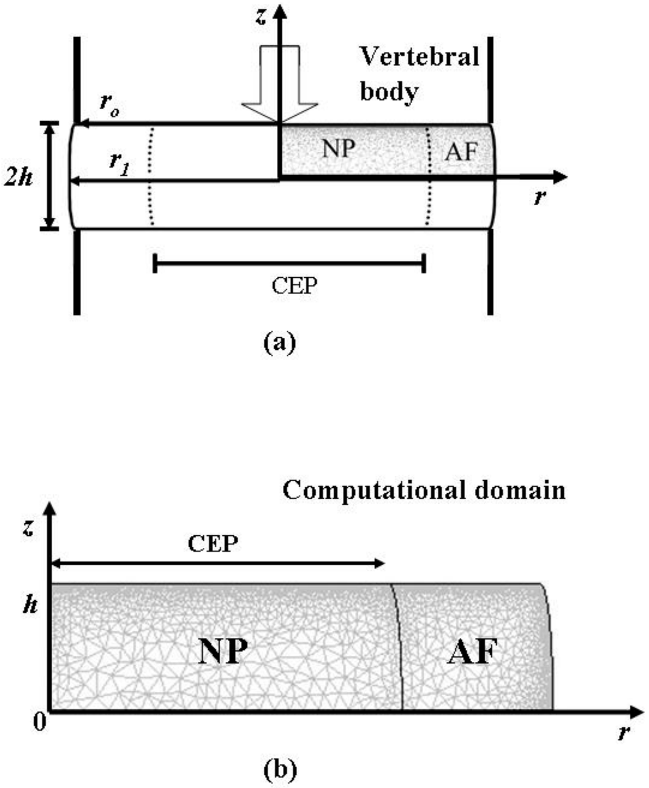

Figure 6.8 Schematic of disc sample and computational domain. (a) The IVD (h = 5 mm, r_o = 19.5 mm, and r_1 = 20 mm) confined between two impermeable vertebral bodies. The superior and inferior surface of the nucleus pulposus (NP) are in contact with perfectly permeable cartilage endplates (CEP). Along the lateral surface of the annulus fibrosus (AF) and at CEP, the disc is in contact with a physiological solution containing 0.15 M NaCl. (b) Computational domain: due to the geometrical symmetry of the problem of interest, only upper quadrant of the sample is modeled with a mesh of 3284 quadratic Lagrange triangular elements.

6.4.2.1 Initial and boundary conditions

Adsorption experiments

It is assumed that, initially, IVD is in equilibrium with the surrounding physiological electrolytic solution of concentration c^* of NaCl. Therefore, letting the superscript (*) indicate the quantities in the physiological solution, the initial condition of the problem are:[114;189;215]

$$\boldsymbol{u} = 0\,,\ \varepsilon^{w} = \varepsilon^{w^*},\ \varepsilon^{+} = \varepsilon^{+^*},\ \varepsilon^{-} = \varepsilon^{-^*},\ \varepsilon^{f} = 0,\ \varepsilon^{b} = 0, \qquad (6.19)$$

where

$$\alpha^{w*} = -2\Phi^{*}c^{*}\,. \qquad (6.20)$$

During testing, IGF-I was gradually introduced in the physiological solution until reaching a prescribed value of c^{f*} (at $t = t_1$). Therefore, at the periannular surface and at the endplate we have:

$$\alpha^{f}(t) = \frac{\alpha_{f}^{*}c^{f*}}{t_1}t \qquad \text{for } t < t_1, \qquad (6.21a)$$

$$\alpha^{f}(t) = \alpha_{f}^{*}c^{f*} \qquad \text{for } t\ \alpha\ t_1, \qquad (6.21b)$$

Mechanical compression to IVD was applied by ramp and hold of the displacement in the z-direction (u_z). Therefore, at $z = h$, the boundary conditions on the solid displacement are:

$$u_z(t) = \frac{u_1}{(t_2 - t_1)}(t - t_1) \quad \text{for } t_1 \leq t < t_2, \qquad (6.22a)$$

$$u_z(t) = u_1 \qquad \text{for } t \leq t_2. \qquad (6.22b)$$

The rest of the boundary conditions are similar to those provided in Section 6.3 for the study of solute transport in unconfined compressed cartilaginous explants.

Desorption experiments

It is assumed that IVD has been formerly equilibrated with a $c^f{}_o$ concentration of IGF-I. Subsequently, the disc, at the CEP and at the periannular surface, is put in contact with a physiological solution of concentration c* of NaCl. In this case, the initial conditions of the problem are:

$$\boldsymbol{u} = 0\,,\ \varepsilon^w = \varepsilon^{w^*}\,,\ \varepsilon^+ = \varepsilon^{+^*}\,,\ \varepsilon^- = \varepsilon^{-^*}\,,\ \varepsilon^f = c^f{}_o\,\gamma_f^*,\ \varepsilon^b = c^b{}_o\,\gamma_b, \qquad (6.23)$$

where

$$\alpha^{w^*} = -2\Phi^* c^* - \Phi^* c_o^f\,. \qquad (6.24)$$

Note that in Equation (6.23), γ_f^* and γ_b are the activity coefficients of free and bound IGF-I solute. The term $c^b{}_o$ is the concentration of bound IGF-I at equilibrium, and its value is calculated from the law of mass action (see Equation (2.29)). At equilibrium (i.e., $dc^b/dt = 0$):

$$c_o^b = \frac{k_{on} c_o^{bs} c_o^f}{k_{on} c_o^f + k_{off}}\,, \qquad (6.25)$$

where $c^{bs}{}_o$ is the initial concentration of IGFBP-3 in the tissue. During desorption, the concentration of IGF-I in the physiological solution was assumed to be negligible.

Therefore, at the periannular surface and at the CEP, the boundary condition for the electrochemical potential of free solute is:

$$\alpha^f = 0, \qquad (6.26)$$

Mechanical compression to IVD was applied by ramp and hold of the displacement in the *z*-direction (u_z). Therefore, at $z = h$, the boundary conditions on the solid displacement are:

$$u_z(t) = \frac{u_1}{t_1} t \qquad \text{for } t < t_1, \qquad (6.27a)$$

$$u_z(t) = u_1 \qquad \text{for } t \leq t_1. \qquad (6.27b)$$

The rest of the boundary conditions are similar to those provided in Section 6.3 for the study of solute transport in unconfined compressed cartilaginous explants.

6.4.2.2 Numerical implementation

The numerical implementation performed in this study is similar to that reported in Section 6.3. Briefly, a mesh of 3284 quadratic Lagrange triangular elements was used in the simulations. The implicit solver of COMSOL® was used for the simulations, and the convergence criterion for the solution was the relative error tolerance of less than 10^{-3}. For each case investigated, the total time of simulation was 12 hours. The maximum time-step was to 15 s. However, in order to avoid the overflow of the output data structure, only 8 points per computed hour (with uniform time interval) were output.

The parameters of the theoretical model were the same as those used in previous studies,[85;86] except for those regarding IGF-I and IGFBP-3. Due to the lack of information about the concentration of IGFBP-3, the binding rate constants k_{on} and k_{off}, and the transport parameters of IGF-I in IVD, in this study, several assumptions were made. First, it was assumed that the concentration of IGFBP-3 in the extracellular matrix was proportional to cell density. In articular cartilage, cell density is $14.1 \cdot 10^{-3}$ cell/mm^3,[187] and the concentration of IGFBP-3 has been estimated to be 50.1 nM.[12] The cellular density in NP and AF are 4.3 and $9.0 \cdot 10^{-3}$ cell/mm^3, respectively.[133] Therefore, it was assumed that IGFBP-3 concentration in NP and AF was 15.3 nM, and 32 nM, respectively. It was also assumed that the kinetics of interactions between IGF-I and IGFBP-3 did not change from cartilage to NP or AF. Therefore, in both NP and AF, it was assumed that $k_{on} = 3.67 \cdot 10^5$ M^{-1}s^{-1}, and $k_{off} = 0.001$ s^{-1}.[31] Diffusive properties of IGF-I in IVD have never been characterized. Therefore, IGF-I diffusion coefficient in NP was chosen as that of articular cartilage reported in literature,[16;172] $D^f_{NP} = 3.23 \cdot 10^{-11}$ m^2/s. However, in AF, solute diffusion is anisotropic. The experimental results reported in Chapter 4 suggest that, in human lumbar IVD, the ratio of the diffusion coefficient in the axial direction (D_{axi}) to that of radial direction (D_{rad}) is $D_{axi}/D_{rad} \sim 2.5$. Therefore, it was assumed that, in AF, $D^f_{axi} = 3.23 \cdot 10^{-11}$ m^2/s, and $D^f_{rad} = 1.29 \cdot 10^{-11}$ m^2/s.

In simulations of absorption, the maximum concentration of IGF-I in the physiological solution (c^{f*}) was 6.5 nM.[171] Besides, the ramp time for IGF-I concentration in the solution was $t_1 = 50$ s. Moreover, the ramp and hold of the mechanical compression applied to the tissue (u_1) corresponded to 5% of the height of the disc. The ramp started at $t_1 = 50$ s and lasted 50 s (until $t_2 = 100$ s).

In simulated cases of desorption, it was assumed that IVD, before releasing the solute, had been equilibrated with a 6.5 nM solution of IGF-I. The ramp of the mechanical compression (maximum compression u_1 = 5% of the height of the disc) lasted 50 s (until t_1= 50s)

6.4.3 Results and discussion

6.4.3.1 Simulation of absorption experiments

In this study, average free solute uptake ratio (R_{free}), average bound solute uptake ratio (R_{bound}), and average total solute uptake ratio (R_{tot}), were determined through the expressions reported in Equations (6.16-18). The effect of static compression on solute uptake in the tissue was compared to the case of free diffusion (i.e., no mechanical load). The results were reported as percentage increase of total solute uptake with respect to the case in which binding interactions between IGF-I and IGFBP-3 were neglected. By compressing the disc, the concentration of binding sites within the tissue increased, and, consequently, IGF-I uptake was enhanced, see Figure 6.9. This effect was especially evident in AF, where the percentage increase of IGF-I uptake changed from 129% (case of free diffusion) to 141% when static compression was applied.

Solute uptake depends non-linearly from the concentration of binding sites present in the tissue, see Figure 6.2. The average uptakes of free and bound IGF-I when static load is applied are reported in Figure 6.12. Data are normalized with respect to the free and bound solute uptakes obtained in the case of free diffusion. While in NP (initial concentration of binding sites c^{bs}_o = 15.3 nM) the increase in solute uptake is 1%, in AF (c^{bs}_o = 32 nM) the gain in IGF-I uptake is more than 6% for both free and bound solute.

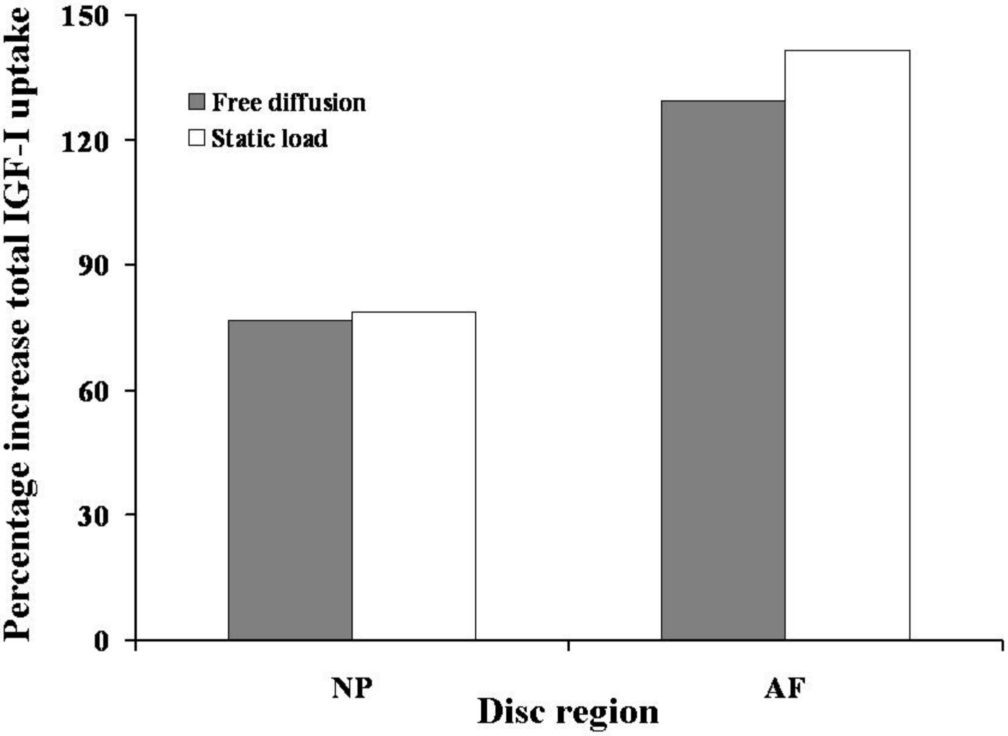

Figure 6.9 Percentage increase of total solute uptake in NP and AF. Data relative to the cases of free diffusion (i.e., no mechanical load) and static compression are compared.

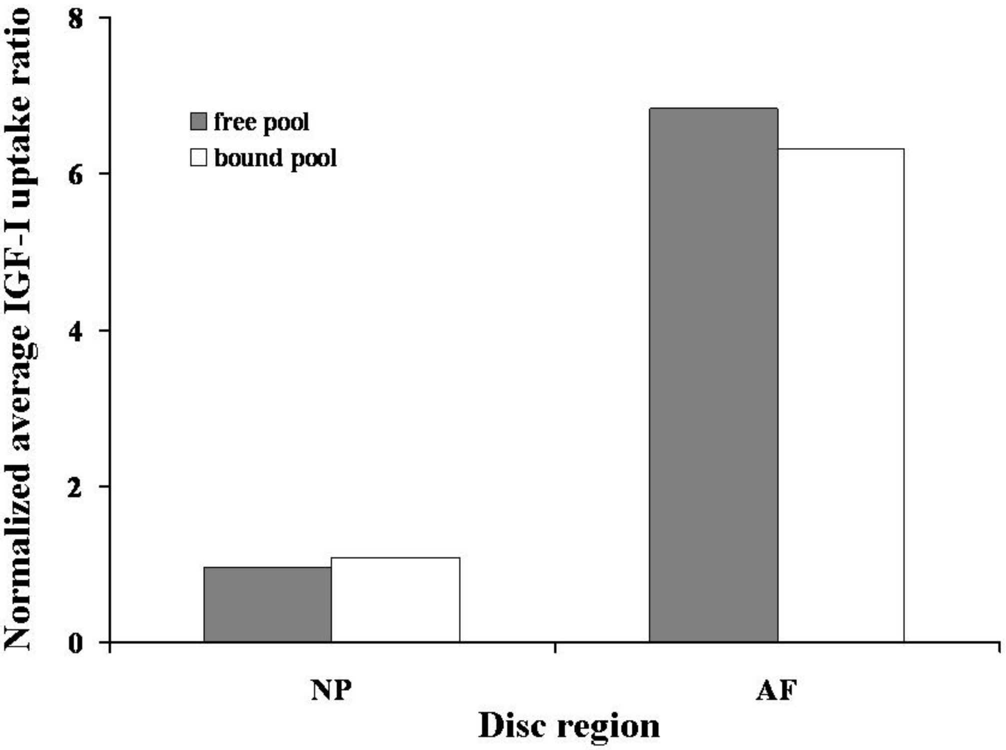

Figure 6.10 Average uptake ratio of free and bound IGF-I in IVD in case of static compression. Data are normalized with respect to the values of uptake ratios obtained in case of free diffusion.

6.4.3.2 Simulation of desorption experiments

Hereby, the effect of binding reactions on solute release from the disc is investigated. The percentage of IGF-I release from IVD is evaluated in case of free diffusion and in case of static compressive load. The results are compared to those obtained in case binding reactions are neglected. In the following, the percentage release of solute is defined as:

$$\%Release = 100 \cdot \frac{M_o - M(t)}{M_o}, \qquad (6.28)$$

where M_o is the initial content of solute in the tissue, and $M(t)$ is its value at specific time.

Due to the presence of binding interactions, IGF-I release from the disc significantly reduced, see Figure 6.11. For both binding and non-reacting solute, the highest percentage release was observed in NP. For the reacting solute this is explained considering that the concentration of binding sites in AF is more than the double of that of NP, therefore the effect of binding is more pronounced in this region of the disc. In contrast, for the non-reacting solute, its diffusion coefficient in NP (D^f_{NP}) is larger than that in the radial direction of AF (D^f_{rad}), see Section 6.4.2.2. Static compression had little effect on the percentage release of IGF-I for both reacting and non-reacting solute.

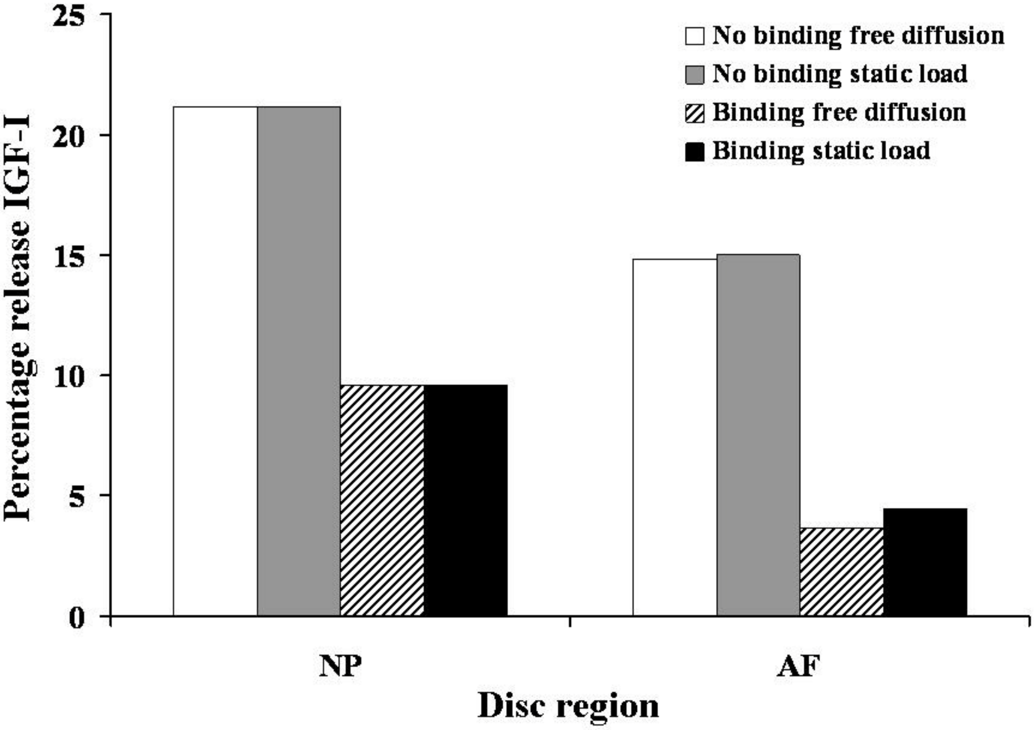

Figure 6.11 Percentage release of IGF-I from IVD for the cases of free diffusion and static compression after 12 hours of desorption. Data relative to non-reacting and binding solutes are reported. For all the cases reported in this figure, the static compression was $u_1 = 5\%$.

The profiles of concentrations of bound and free IGF-I along the radial direction of the disc (i.e., $z = 0$) are reported in Figure (6.12). The concentration of bound IGF-I in AF was higher than that in NP, see Figure (6.12a). In contrast, free IGF-I had the opposite gradient of distribution: higher in NP than in AF, see Figure (6.12b). The jumps in concentration of both free and bound IGF-I from NP to AF were due to the heterogeneous distribution of IGFBP-3 within the tissue (i.e., higher in AF and lower in NP).

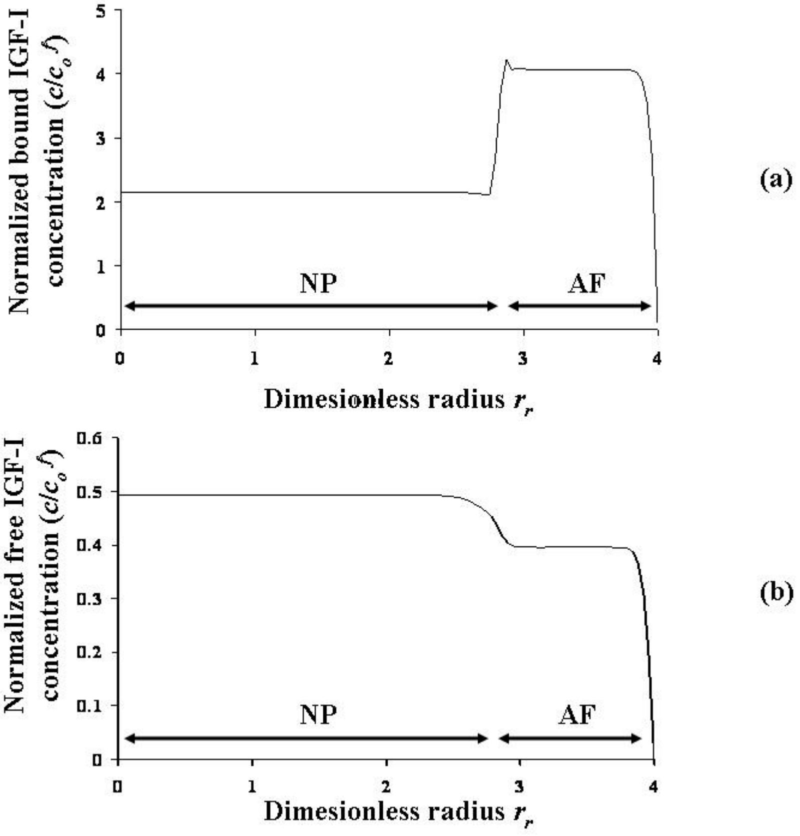

Figure 6.12 Distribution of IGF-I in IVD along the radial direction (at $z = 0$) after 12 hours of desorption. The profiles of concentration of bound (a) and free (b) fractions of solute are shown. For the case reported in the figure no mechanical load was applied to the tissue.

6.4.4 Conclusions

The objective of this study was to investigate the effect of binding interactions on solute transport in intervertebral disc. A finite element model, based on the mixture theory for charged hydrated soft tissues, was developed to describe the anisotropic and heterogeneous solute transport in IVD. The absorption and the desorption of a solute interacting with the extracellular matrix of the disc were investigated in the case of free diffusion and in the case of mechanical deformation of the tissue. The role of the binding proteins in regulating solute transport was highlighted.

Chapter 7: GENERAL CONCLUSIONS AND RECOMMENDATIONS

7.1 Overview

Knowledge of transport phenomena in IVD is crucial in order to elucidate the mechanisms of disc degeneration and also in order to develop strategies for tissue repair (in *vivo*), and tissue engineering (in *vitro*). Solute transport within the disc is complex, and involves a series of mechanical, electrical, chemical and biological coupled events. Despite of the large amount of studies performed in the past, transport phenomena in IVD are still poorly understood. For instance there is still a lack of knowledge on the relationship between anisotropic solute diffusivity in annulus fibrosus and the morphology and composition of this region of the disc. Moreover, it is known that several solutes (e.g., growth factors) bind to the cells and the extracellular matrix of the disc. However, binding mechanisms in IVD have never been investigated. This is partly due to the limited number of available experimental techniques for investigating binding phenomena, and the paucity of theoretical or numerical methods for systematically predicting the kinetics of transport and binding in IVD.

In light of the current state of knowledge in the field, this dissertation was focused on (1) the development of new imaging techniques for experimentally determine solute diffusivity and binding reaction rates in biological tissues, (2) the investigation on the relationship between transport properties and the structure of IVD, and (3) the development of a numerical framework for predicting solute binding and transport in cartilaginous tissues. In order to achieve these research aims, three major studies were carried out: (1) development of two new FRAP techniques for measuring the anisotropic diffusion tensor and the binding reaction rates of solutes in biological tissues (see Chapters 3 and 5); (2) investigation on the relationship between solute diffusivity and the microstructure of the human lumbar annulus fibrosus (see Chapter 4); (3) development of a finite element framework for modeling solute transport and binding interactions in cartilaginous tissues (see Chapter 6). The most important findings and the recommendations for future development of research are reported below.

7.2 FRAP methods for determining binding and transport parameters in biological tissues

The experimental methods developed in this study were based on two independent image analyses: the Fourier analysis of light intensity decay of video-FRAP image series, and the Karhunen-Loéve transform (KLT) for the analysis of the shape and the orientation of the bleach spot. The combination of these two techniques allowed the determination of the solute anisotropic tensor and the rates of solute binding and unbinding within the extracellular matrix of a biological tissue.

Numerically simulated FRAP experiments were used for assessing the accuracy and the robustness of the techniques. It was found that the solute diffusivity and binding rates are determined with good accuracy for most cases simulated over a wide range of variation of both diffusion coefficients (three orders of magnitude) and binding rates (six orders of magnitude).

The results of the numerical validations also provided important guidelines for the optimization of the experimental and data analysis parameters. For instance, it was found that the highest accuracy in determining the diffusion tensor is obtained when the initial dimension of the bleach spot is eight times smaller than the size of the FRAP image. Besides, results indicated that Fourier analysis provides the most accurate results when frequency couples belonging to 'Ring 4' are used. Moreover, it was also shown that, in the presence of binding interactions, the simultaneous analysis of multiple FRAP tests, obtained at different initial sizes of the bleach spot, significantly increases the robustness of the technique in determining both the diffusion tensor and the rates of binding and unbinding.

Through KLT analysis, the orientation of the principal directions of the diffusion tensor was related to the structure of the tissue. Therefore, these new techniques can characterize solute binding and diffusivity and, in addition, relate tissue morphology to its transport properties.

The techniques and the analyses developed in these studies present two major limitations. The molecular probes used in the experiments were fluorescein and 5-dodecanoylaminofluorescein (DAF). Neither probe is present in IVD, therefore, these are not physiologically relevant. Although the use of these solutes provided new insights on transport and binding interactions in IVD, in future studies, the behavior of more physiologically relevant molecules (e.g., growth factors) should be investigated.

The new technique can determine the pseudo-binding rate k^*_{on}. This parameter is related to the constant rate of solute association k_{on} and the concentration of available binding sites present in the tissue during experiments (c^{bs}_{eq}):

$$k^*_{on} = k_{on} c^{bs}_{eq} . \qquad (7.1)$$

It should be noted that:

$$c_{eq}^{bs} = c_o^{bs} - c_{eq}^{b}, \qquad (7.2)$$

where $c^{bs}{}_{o}$ is the total concentration of binding sites present in the tissue, and $c^{b}{}_{eq}$ is the concentration of bound solute at equilibrium (i.e., during a FRAP experiment). Therefore, the value of $c^{bs}{}_{eq}$ is not generally constant since it depends on the concentration of fluorescent probe introduced in the tissue before performing a FRAP experiment. In order to determine the value of k_{on}, knowledge of the total concentration of binding sites in the tissue ($c^{bs}{}_{o}$) is required. Indeed, from Equations (7.1-2) and from Equations (5.7a-b), the following relationships hold:

$$k_{on}^{*} = k_{on}(c_o^{bs} - c_{eq}^{b}), \qquad (7.3)$$

$$\frac{k_{on}^{*}}{k_{off}} = \frac{c_{eq}^{b}}{c_{eq}^{f}}. \qquad (7.4)$$

The values of $k^{*}{}_{on}$ and k_{off} can be determined by a FRAP experiment. Besides, known the partition coefficient of the molecular probe in the tissue, the concentration of free solute at equilibrium ($c^{f}{}_{eq}$) can be calculated (and so $c^{b}{}_{eq}$ from Equation (7.4)). Finally, if the total concentration of binding sites in the tissue ($c^{bs}{}_{o}$) is known, the solute association rate k_{on} can be determined from Equation (7.3).

In light of the above requirements, additional studies should be performed in order to determine, for each solute of interest, the concentration of the corresponding binding sites in tissues.

7.3 Relationship between solute anisotropic diffusivity and morphology of human lumbar annulus fibrosus

The aim of this study was to test the hypothesis that the anisotropic and inhomogeneous diffusive behavior of solutes in annulus fibrosus is related to the unique arrangement of collagen fibers of the extracellular matrix of the disc (i.e., microtubes). In order to achieve this goal, two independent analyses were carried out: (1) characterization of the anisotropic diffusion tensor of fluorescein in the inner (IAF), the middle (MAF) and the outer (OAF) annulus fibrosus of L3-L4 human lumbar discs; (2) scanning electron microscopy (SEM) imaging of IAF, MAF, and OAF in order to determine the orientation of microtubes and their density (i.e., microtube area fraction) in the three different regions of the disc. The anisotropic behavior of fluorescein diffusivity was attributed to the orientation of the microtubes in AF (running parallel to the direction of the collagen fibers). Moreover, the trends of variation of diffusion coefficients and microtube area fraction were consistent among each other (being highest in IAF and lowest in OAF), further indicating a relationship between structure of AF and its transport properties. These findings suggested that microtubes may represent preferential pathways for solute diffusion in IVD.

The major limit of this study was that only a limited number of discs were used: 3 for diffusivity measurements, and 1 for SEM imaging analysis. In particular, the disc used for structure analysis was classified as Grade III according to Thompson's morphologic grading scheme. It is reasonable to hypothesize that disc degeneration could significantly alter the structural arrangement and the density of collagen fibers within the extracellular matrix. In light of the findings of this study, a structural change of the extracellular matrix of the tissue could have significant implications on the transport properties of the disc. Therefore, structural analysis and measurement of transport properties of degenerated discs (higher than Grade III) are crucial for a better understanding of the nutritional pathways and the related degenerative pathology of the intervertebral disc.

7.4 Modeling solute transport and binding interactions in cartilaginous tissues.

A numerical framework was developed for modeling solute transport and binding interactions in biological tissues. The model was applied to describe the coupled solute transport and electromechanical behavior of articular cartilage and intervertebral disc. In specific, the absorption and the release of solute and its distribution within the tissue were investigated for the case of free diffusion (i.e., no mechanical load applied to the tissue), and for the case of static and cyclic unconfined compression of the tissues.

Binding interactions significantly affected solute transport in the tissue. It was found that tissue absorption and release of solutes is mainly controlled by the concentration of binding site in the extracellular matrix and by the rates of association and dissociation of the solutes with the binding proteins. Binding interactions promoted the accumulation of solute in the extracellular matrix and slowed its transport through the tissue. When mechanical load was applied, these phenomena were enhanced by the increase in concentration of binding sites due to compressive deformation of the tissue.

In applying this numerical framework to modeling solute transport and binding interactions in IVD the major limitation of the study was the lack of knowledge of diffusivity and binding rates of IGF-I, and the concentration of IGFBP-3 in the disc. Therefore, the natural recommendation for future studies is to experimentally determine binding and transport properties of growth factors and their corresponding binding protein.

In addition, the finite element model herein developed could provide more realistic predictions if two major limitations are overcome. First, the theoretical framework, on which this numerical model is based, assumed only one binding state for the reacting solute. In general, reacting solutes can be characterized by multiple binding states. For instance, in articular cartilage IGF-I may interact with various types of binding proteins, as well as cell surface receptors.[115] Therefore, the numerical model should take into account the possibility of multiple binding interactions for the reacting solute. Moreover, it was assumed that the binding solute was uncharged. However, some amino-acids which develop binding interactions with the extracellular matrix are electrically non-neutral.[93] Therefore, the theoretical and numerical frameworks developed could be further extended in order to consider the presence of charged binding solutes.

APPENDIX

A.1 Convective flux and diffusive flux in porous media

In this framework, fluid and solute transport in the mixture are described by the relative fluid and solutes fluxes (relative to the solid phase of the mixture). Therefore, the relative fluid flux ($\boldsymbol{J}^w$) is defined as:

$$\boldsymbol{J}^w = \phi^w(\boldsymbol{v}^w - \boldsymbol{v}^s), \qquad (2.14)$$

and the relative molar fluxes of solutes ($\boldsymbol{J}^\alpha$) are defined as:

$$\boldsymbol{J}^\alpha = \phi^w c^\alpha(\boldsymbol{v}^\alpha - \boldsymbol{v}^s) \quad (\alpha = +,-,f). \qquad (2.15)$$

For solute phases, solving Equation (2.13) for $\boldsymbol{v}^\alpha$ yields:

$$\boldsymbol{v}^\alpha = (\sum_\alpha f_{\alpha\alpha}\boldsymbol{v}^\alpha - \alpha^\alpha\nabla\mu^\alpha)/d^\alpha, \quad (\alpha = w,s,+,-,f) \qquad (A.1)$$

where d^α is defined as:

$$d^\alpha = \sum_\alpha f_{\alpha\alpha}. \qquad (A.2)$$

Introducing the solute convective velocity $\boldsymbol{v}_c^\alpha$, defined as:[217]

$$\boldsymbol{v}_c^{\alpha} = \sum_{\alpha} f_{\alpha\alpha} \boldsymbol{v}^{\alpha} / d^{\alpha}, \qquad \text{(A.3)}$$

equation (A.1) can be rewritten as it follows:

$$\boldsymbol{v}^{\alpha} = \boldsymbol{v}_c^{\alpha} - \alpha^{\alpha} \nabla \mu^{\alpha} / d^{\alpha}. \qquad \text{(A.4)}$$

The above equation indicates that, within the mixture, each solute phase move through the mixture with a convective velocity ($\boldsymbol{v}_c^{\alpha}$) and a diffusive velocity resulted from the gradient of its electro-chemical potential. Let D^{α} be the intrinsic diffusion coefficient of the α-solute, defined as:[61]

$$D^{\alpha} = RT\phi^{w} c^{\alpha} / d^{\alpha}. \qquad \text{(A.5)}$$

Using Equations (2.15), (A.4), and (A.5), the relative molar flux of the α-solute can be rewritten as:

$$\boldsymbol{J}^{\alpha} = \phi^{w} c^{\alpha} (\boldsymbol{v}_c^{\alpha} - \boldsymbol{v}^{s}) - D^{\alpha} \alpha^{\alpha} \nabla \mu^{\alpha} / RT. \text{ (A.6)}$$

Considering the case in which the frictional interactions among solutes are negligible, using Equation (A.3), the relative convective velocity ($\boldsymbol{v}_c^{\alpha}$ - $\boldsymbol{v}^{s}$) can be expressed as:

$$\boldsymbol{v}_c^{\alpha} - \boldsymbol{v}^{s} = H^{\alpha} (\boldsymbol{v}^{w} - \boldsymbol{v}^{s}), \qquad \text{(A.7)}$$

where the parameter H^{α} is defined as:[217]

$$H^{\alpha} = \frac{f_{\alpha w}}{f_{\alpha w} + f_{\alpha s}}. \quad (\alpha = +,-,f) \qquad \text{(A.8)}$$

The parameter H^{α} is the hindrance factor (or convection coefficient) and represents the hindrance effect on convection due to steric and hydrodynamic interactions between the solute and the solid matrix.[40;47;99] The hindrance factor is equal to unity in the case of binary mixtures (in absence of solid phase). However, little is known about the value of H^{α} in charged hydrates soft tissues. Yao and Gu (2006) defined the range of possible values for the hindrance factor:[217]

$$\frac{D^{\alpha}}{D_o^{\alpha}} \le H^{\alpha} \le 1, \qquad \text{(A.9)}$$

where D_o^{α} is the α-solute diffusion coefficient of the binary mixture (α-solute and fluid phase). It should be noted that the above inequality does not hold for those solutes that diffuse faster in porous media than in water.[217]

Combining Equations (2.14), (A.6), and (A.7), the relative molar flux of solutes can be written as:

$$\boldsymbol{J}^{\alpha} = H^{\alpha} c^{\alpha} \boldsymbol{J}^{w} - D^{\alpha} \alpha^{\alpha} \nabla \mu^{\alpha} / RT. \quad (\alpha = +,-,f) \quad \text{(2.16)}$$

Finally, from Equations (2.13), (2.14), and (A.8), the flux of the interstitial fluid can be rewritten as:

$$\boldsymbol{J}^w = -\frac{K}{\phi^w}(\alpha^w \nabla \mu^w + \sum_\alpha H^\alpha \alpha^\alpha \nabla \mu^\alpha). \quad (\alpha = +,-,f) \qquad (2.17)$$

In the above equation, K is the hydraulic permeability, defined as:

$$K = \frac{(\phi^w)^2}{F}, \qquad (A.10)$$

where the coefficient F depends on the frictional coefficients as it follows:[85]

$$F = f_{ws} + \sum_\alpha f_{w\alpha}(1 - H^\alpha). \quad (\alpha = +,-,f) \qquad (A.11)$$

A.2 Equivalent formulation of the mixture theory

Due to the complexity of the system of equations defining the mechano-electrochemical behavior and the solute transport in charged hydrated soft tissues, no analytical solution is available for most boundary value problems. Therefore, solutions of the problems are generally achieved by numerical approaches. Sun et al. (1998) proposed a finite element formulation of the governing equations of the mixture theory in which the degrees of freedom of the mixture are expressed as a function of the solid displacement and the modified electro-chemical potentials of the interstitial fluid and ions.[189] Recently, extensions of this formulation included the description of uncharged solute transport and chemical reactions within the tissue.[86;87;216-219] In this thesis, the formulation of the finite element model for solute diffusive-convective-reactive transport in charged hydrated soft tissues follows the same methodological approach. Therefore, consistent with the formulation proposed by Sun et al. (1998), the modified electro-chemical potentials are defined as follows:[189]

Water phase

$$\alpha^w = \frac{\alpha_T^w(\mu^w - \mu_o^w)}{RT} = \frac{p}{RT} - \Phi(c^+ + c^- + c^f) + \frac{B_w}{RT}e, \tag{A.12}$$

Cation

$$\alpha^+ = exp[M^+(\mu^+ - \mu_o^+)/RT] = \alpha^+ c^+ exp(\frac{F_c\alpha}{RT}), \tag{A.13}$$

Anion

$$\alpha^- = exp[M^-(\mu^- - \mu_o^-)/RT] = \alpha c^- exp(-\frac{F_c\alpha}{RT}), \tag{A.14}$$

Uncharged free solute

$$\alpha^f = exp[M^f(\mu^f - \mu_o^f)/RT] = \alpha^f c^f. \tag{A.15}$$

Bound complex

$$\alpha^b = exp[M^f(\mu^b - \mu_o^b)/RT] = \alpha^b c^b. \tag{A.16}$$

Solving Equation (A.12) for the pressure (*p*) provides a new expression for the constitutive equation of the mixture stress tensor presented in Equation (2.18):

$$\sigma = -[RT\alpha^w + RT\Phi(c^+ + c^- + c^f) - p_o - T_c] + (\alpha + B_w)\nabla \cdot \boldsymbol{u} + \mu[\nabla \boldsymbol{u} + (\nabla \boldsymbol{u})^T], \tag{A.17}$$

where p_o represents the pressure at the reference configuration (this is discussed in Chapter 6). Moreover, the definitions of the modified electro-chemical potentials also require a consistent redefinition of the fluxes of fluid, ions and solute as it follows:

Water phase
$$\boldsymbol{J}^{w} = -RTK(\nabla\alpha^{w} + \frac{H^{+}c^{+}}{\alpha^{+}}\nabla\alpha^{+} + \frac{H^{-}c^{-}}{\alpha^{-}}\nabla\alpha^{-} + \frac{H^{f}c^{f}}{\alpha^{f}}\nabla\alpha^{f}), \tag{A.19}$$

Cation
$$\boldsymbol{J}^{+} = H^{+}c^{+}\boldsymbol{J}^{w} - \frac{\phi^{w}D^{+}c^{+}}{\varepsilon^{+}}\nabla\varepsilon^{+}, \tag{A.20}$$

Anion
$$\boldsymbol{J}^{-} = H^{-}c^{-}\boldsymbol{J}^{w} - \frac{\phi^{w}D^{-}c^{-}}{\varepsilon^{-}}\nabla\varepsilon^{-}, \tag{A.21}$$

Uncharged free solute
$$\boldsymbol{J}^{f} = H^{f}c^{f}\boldsymbol{J}^{w} - \frac{\phi^{w}D^{f}c^{f}}{\varepsilon^{f}}\nabla\varepsilon^{f}. \tag{A.22}$$

A.3 Formulation of the finite element model

A.3.1 The weak formulation

Using the Galerkin weighted residual method, the weak form of the governing equations (2.12), (2.29), (2.30), (2.33), (2.34), and (2.35) reads:

$$\int_{\alpha} \boldsymbol{w}\cdot\nabla_{r}\cdot\sigma_{r}d\alpha = 0, \tag{A.23}$$

$$\int_{\alpha} w^{(1)}[\nabla_{r}\cdot(\boldsymbol{v}_{r}^{s} + \boldsymbol{J}_{r}^{w})]d\alpha = 0, \tag{A.24}$$

$$\int_{\alpha} w^{(2)}[\nabla_{r}\cdot(\boldsymbol{J}_{r}^{+} - \boldsymbol{J}_{r}^{-})]d\alpha = 0, \tag{A.25}$$

$$\int_{\alpha} w^{(3)}[\partial(\phi^{w}c_{r}^{k})/\partial t + \nabla_{r}\cdot(\boldsymbol{J}_{r}^{+} + \boldsymbol{J}_{r}^{-} + \phi^{w}c_{r}^{k}\boldsymbol{v}_{r}^{s})]d\alpha = 0, \tag{A.26}$$

$$\int_{\alpha} w^{(4)}[\partial(\phi^{w}c^{f} + \phi^{w}c^{b})/\partial t + \nabla_{r}\cdot(\boldsymbol{J}^{f} + \phi^{w}c_{r}^{f}\boldsymbol{v}_{r}^{s} + \phi^{w}c_{r}^{b}\boldsymbol{v}_{r}^{s})]d\alpha = 0, \tag{A.27}$$

$$\int_{\alpha} w^{(5)}[dc_{r}^{b}/dt - k_{on_{r}}(c_{o_{r}}^{bs} + c_{o_{r}}^{b} - c_{r}^{b})c_{r}^{f} + k_{off_{r}}c_{r}^{b}]d\alpha = 0, \tag{A.28}$$

where vector $\boldsymbol{w}$ and four scalar functions $w^{(1)}$, $w^{(2)}$, $w^{(3)}$, $w^{(4)}$, and $w^{(5)}$ are arbitrary admissible weighting functions for the five governing equations.

Applying the divergence theorem to equations (A.23-27), we have:

$$\int_{\alpha} tr[(\nabla_r \boldsymbol{w})^T \cdot \sigma_r]d\alpha = \int_{\alpha_t} \boldsymbol{w} \cdot \boldsymbol{t}_r^* d\alpha\,, \tag{A.29}$$

$$\int_{\alpha} w^{(1)}\nabla_r \cdot \boldsymbol{v}_r^s d\alpha - \int_{\alpha} \boldsymbol{J}_r^w \cdot \nabla_r w^{(1)} d\alpha = -\int_{\alpha_{J^w}} w^{(1)}\boldsymbol{J}_r^{w*} \cdot \boldsymbol{n} d\alpha\,, \tag{A.30}$$

$$\int_{\alpha} (\boldsymbol{J}_r^+ - \boldsymbol{J}_r^-) \cdot \nabla_r w^{(2)} d\alpha = \int_{\alpha_{J^+}} w^{(2)}\boldsymbol{J}_r^{+*} \cdot \boldsymbol{n} d\alpha - \int_{\alpha_{J^-}} w^{(2)}\boldsymbol{J}_r^{-*} \cdot \boldsymbol{n} d\alpha\,, \tag{A.31}$$

$$\begin{aligned}&\int_{\alpha} w^{(3)}\, \partial(\phi^w c_r^k)/\partial t d\alpha - \int_{\alpha} (\boldsymbol{J}_r^+ + \boldsymbol{J}_r^-) \cdot \nabla_r w^{(3)} d\alpha \\ &+ \int_{\alpha} w^{(3)}\nabla_r \cdot (\phi^w c_r^k \boldsymbol{v}_r^s) d\alpha = -\int_{\alpha_{J^+}} w^{(3)}(\boldsymbol{J}_r^{+*} + \boldsymbol{J}_r^{-*}) \cdot \boldsymbol{n} d\alpha\,,\end{aligned} \tag{A.32}$$

$$\begin{aligned}&\int_{\alpha} w^{(4)}\partial(\phi^w c_r^f + \phi^w c_r^b)/\partial t d\alpha - \int_{\alpha} \boldsymbol{J}_r^f \cdot \nabla_r w^{(4)} d\alpha + \int_{\alpha} w^{(4)}\nabla_r \cdot (\phi^w c_r^f \boldsymbol{v}_r^s) d\alpha + \\ &\int_{\alpha} w^{(4)}\nabla_r \cdot (\phi^w c_r^b \boldsymbol{v}_r^s) d\alpha = -\int_{\alpha_{Jf}} w^{(4)}\boldsymbol{J}_r^{f*} \cdot n d\alpha\end{aligned}\,, \tag{A.33}$$

where $\boldsymbol{t}_r^* = \sigma_r^* \cdot \boldsymbol{n}$ is the traction on the boundary of the tissue, and (*) stands for the quantities on the tissue boundary.

A.3.2 Adaptation of the formulation to an axisymmetric geometry

For an axisymmetric coordinate system individuated by (r,z), the strain tensor ($\boldsymbol{E}_r$) and the stress tensor ($\boldsymbol{\sigma}_r$) within the tissue are redefined as:

$$\boldsymbol{E}_r = \begin{bmatrix} \dfrac{\partial(u_r)_r}{\partial r} & 0 & \dfrac{1}{2}\left(\dfrac{\partial(u_r)_r}{\partial z} + \dfrac{\partial(u_z)_r}{\partial r}\right) \\ 0 & \dfrac{u_r}{r} & 0 \\ \dfrac{1}{2}\left(\dfrac{\partial(u_r)_r}{\partial z} + \dfrac{\partial(u_z)_r}{\partial r}\right) & 0 & \dfrac{\partial(u_z)_r}{\partial z} \end{bmatrix}, \tag{A.34}$$

$$\sigma_r = \begin{bmatrix} \alpha_{r_{11}} & 0 & \alpha_{r_{13}} \\ 0 & \alpha_{r_{22}} & 0 \\ \alpha_{r_{13}} & 0 & \alpha_{r_{33}} \end{bmatrix}, \qquad \text{(A.35)}$$

where

$$(u_r)_r = \frac{u_r}{h}, \qquad \text{(A.36)}$$

$$(u_z)_r = \frac{u_z}{h}, \qquad \text{(A.37)}$$

$$\alpha_{r_{11}} = -\left[\alpha^w_r + \alpha\,(c^+_r + c^-_r + c^f_r) - \frac{p_o}{RTc*}\right] + \frac{\alpha}{RTc*}\left(\frac{\partial u_r}{\partial r} + \frac{u_r}{r} + \frac{\partial u_z}{\partial z}\right) + \frac{\mu}{RTc*}\frac{\partial u_r}{\partial r}, \qquad \text{(A.38)}$$

$$\alpha_{r_{22}} = -\left[\alpha^w_r + \alpha\,(c^+_r + c^-_r + c^f_r) - \frac{p_o}{RTc*}\right] + \frac{\alpha}{RTc*}\left(\frac{\partial u_r}{\partial r} + \frac{u_r}{r} + \frac{\partial u_z}{\partial z}\right) + \frac{\mu}{RTc*}\frac{u_r}{r}, \qquad \text{(A.39)}$$

$$\alpha_{r_{33}} = -\left[\alpha^w_r + \alpha\,(c^+_r + c^-_r + c^f_r) - \frac{p_o}{RTc*}\right] + \frac{\alpha}{RTc*}\left(\frac{\partial u_r}{\partial r} + \frac{u_r}{r} + \frac{\partial u_z}{\partial z}\right) + \frac{\mu}{RTc*}\frac{\partial u_z}{\partial z}, \qquad \text{(A.40)}$$

$$\alpha_{r_{13}} = \frac{\mu}{RTc*}\left(\frac{\partial u_r}{\partial z} + \frac{\partial u_z}{\partial r}\right). \qquad \text{(A.41)}$$

Moreover, the following relationships hold:

$$\nabla_r \cdot v^s_r = \frac{\partial^2 (u_r)_r}{\partial t_r \partial r} + \frac{1}{r}\frac{\partial (u_r)_r}{\partial t_r} + \frac{\partial^2 (u_z)_r}{\partial t_r \partial z} \qquad \text{(A.42)}$$

$$\begin{aligned} \nabla_r \cdot (\phi^w c^\alpha_r v^s_r) &= \nabla_r (\phi^w c^\alpha_r) \cdot v^s_r + \phi^w c^\alpha_r \nabla_r \cdot v^s_r = \frac{\partial (u_r)_r}{\partial t_r} \cdot \left(\frac{\partial \phi^w}{\partial r} c^\alpha_r + \frac{\partial c^\alpha_r}{\partial r}\phi^w\right) \\ &+ \frac{\partial (u_z)_r}{\partial t_r} \cdot \left(\frac{\partial \phi^w}{\partial z} c^\alpha_r + \frac{\partial c^\alpha_r}{\partial z}\phi^w\right) + \phi^w c^\alpha_r \left[\frac{\partial^2 (u_r)_r}{\partial t_r \partial r} + \frac{(u_r)_r}{r} + \frac{\partial^2 (u_z)_r}{\partial t_r \partial z}\right]. \quad \alpha = (k, f, b) \end{aligned} \qquad \text{(A.43)}$$

Finally, Equations (A.28-33) are specialized for an axisymmetric coordinate system as follow:

$$\int_{\alpha}\left(\alpha_{r_{11}}\frac{\partial w_r}{\partial r}+\alpha_{r_{13}}\frac{\partial w_r}{\partial z}+\alpha_{r_{22}}\frac{w_r}{r}\right)d\alpha=\int_{\alpha_t} w_r\cdot t_{r_r}{}^{*}d\alpha\,, \tag{A.44}$$

$$\int_{\alpha}\left(\alpha_{r_{13}}\frac{\partial w_z}{\partial r}+\alpha_{r_{33}}\frac{\partial w_z}{\partial z}\right)d\alpha=\int_{\alpha_t} w_z\cdot t_{z_r}{}^{*}d\alpha\,, \tag{A.45}$$

$$\begin{aligned}&\int_{\alpha} w^{(1)}\left(\frac{\partial^2(u_r)_r}{\partial t_r\partial r}+\frac{1}{r}\frac{\partial(u_r)_r}{\partial t_r}+\frac{\partial^2(u_z)_r}{\partial t_r\partial z}\right)d\alpha-\int_{\alpha}\left[(J_r^w)_r\frac{\partial w^{(1)}}{\partial r}+(J_z^w)_r\frac{\partial w^{(1)}}{\partial z}\right]d\alpha=\\&-\int_{\alpha_{J_r^w}} w^{(1)}[(J_r^{w*})_r n_r+(J_z^{w*})_r n_z]d\alpha\end{aligned}\,, \tag{A.46}$$

$$\begin{aligned}&\int_{\alpha}\left\{[(J_r^+)_r-(J_r^-)_r]\frac{\partial w^{(2)}}{\partial r}+[(J_z^+)_r-(J_z^-)_r]\frac{\partial w^{(2)}}{\partial z}\right\}d\alpha=\\&\int_{\alpha_{J_r^+}} w^{(2)}[(J_r^{+*})_r n_r+(J_z^{+*})_{rr}n_z]d\alpha-\int_{\alpha_{J_r^-}} w^{(2)}[(J_r^{-*})_r n_r+(J_z^{-*})_{rr}n_z]d\alpha\end{aligned}\,, \tag{A.47}$$

$$\begin{aligned}&\int_{\alpha} w^{(3)}\,\partial(\phi^w c_r^k)/\partial t_r d\alpha-\int_{\alpha}\left\{[(J_r^+)_r+(J_r^-)_r]\frac{\partial w^{(3)}}{\partial r}+[(J_z^+)_r+(J_z^-)_r]\frac{\partial w^{(3)}}{\partial z}\right\}d\alpha+\\&\int_{\alpha} w^{(3)}\left[\frac{\partial(u_r)_r}{\partial t_r}\cdot\left(\frac{\partial\phi^w}{\partial r}c_r^k+\frac{\partial c_r^k}{\partial r}\phi^w\right)+\frac{\partial(u_z)_r}{\partial t_r}\cdot\left(\frac{\partial\phi^w}{\partial z}c_r^k+\frac{\partial c_r^k}{\partial z}\phi^w\right)\right]d\alpha+\\&\int_{\Omega}\phi^w c_r^k\left[\frac{\partial^2(u_r)_r}{\partial t_r\partial r}+\frac{1}{r}\frac{\partial(u_r)_r}{\partial t_r}+\frac{\partial^2(u_z)_r}{\partial t_r\partial z}\right]d\alpha=-\int_{\alpha_{J_r^+}} w^{(3)}[(J_r^{+*})_r n_r+(J_z^{+*})_r n_z]d\alpha-\int_{\alpha_{J_r^-}} w^{(3)}[(J_r^{-*})_r n_r+(J_z^{-*})_r n_z]d\alpha\end{aligned}\,, \tag{A.48}$$

$$\begin{aligned}&\int_{\alpha} w^{(4)}\,\partial(\phi^w c_r^f+\phi^w c_r^b)/\partial t_r d\alpha-\int_{\alpha}\left[(J_r^f)_r\frac{\partial w^{(4)}}{\partial r}+(J_z^f)_r\frac{\partial w^{(4)}}{\partial z}\right]d\alpha+\\&\int_{\alpha} w^{(4)}\left\{\frac{\partial(u_r)_r}{\partial t_r}\cdot\left[\frac{\partial\phi^w}{\partial r}(c_r^f+c_r^b)+\phi^w\frac{\partial c_r^f}{\partial r}+\phi^w\frac{\partial c_r^b}{\partial r}\right]+\frac{\partial(u_z)_r}{\partial t_r}\cdot\left[\frac{\partial\phi^w}{\partial z}(c_r^f+c_r^b)+\phi^w\frac{\partial c_r^f}{\partial z}+\phi^w\frac{\partial c_r^b}{\partial z}\right]\right\}d\alpha+\\&\int_{\Omega}\phi^w(c_r^f+c_r^b)\cdot\left[\frac{\partial^2(u_r)_r}{\partial t_r\partial r}+\frac{1}{r}\frac{\partial(u_r)_r}{\partial t_r}+\frac{\partial^2(u_r)_r}{\partial t_r\partial z}\right]d\Omega=-\int_{\alpha_{J_r^f}} w^{(4)}[(J_r^{f*})_r n_r+(J_z^{f*})_r n_z]d\alpha\end{aligned}\,, \tag{A.49}$$

$$\int_{\alpha} w^{(5)}[dc_r^b/dt-k_{on_r}(c_{o_r}^{bs}+c_{o_r}^b-c_r^b)c_r^f+k_{off_r}c_r^b]d\alpha=0 \tag{A.50}$$

REFERENCES

1. Adams MA, Hutton WC. The effect of posture on diffusion into lumbar intervertebral discs. *J Anat.* 1986;147:121-34.

2. Aguiar D, Johnson S, Oegema T. Notochondral cells interact with nucleus pulposus cells: regulation of proteoglycan synthesis. *Exp Cell Res* 1999;246:129-37.

3. Arkill KP, Winlove CP. Solute transport in deep and calcified zones of articular cartilage. *Osteoarthritis and Cartilage* 2008;13:708-14.

4. Ateshian GA. On the theory of reactive mixtures for modeling biological growth. *Biomechan Model Mechanobiol* 2007;6:423-45.

5. Ateshian GA, Costa KD, Azeloglu EU et al. Continuum modeling of biological tissue growth by cell division, and alteration of intracellular osmolytes and extracellular fixed charge density. *Journal of Biomechanical Engineering* 2009;131:doi:10.1115/1.3192138.

6. Axelrod D, Koppel DE, Schlessinger J et al. Mobility measurement by analysis of fluorescence photobleaching recovery kinetics. *Biophys J* 1976;16:1055-69.

7. Bartels EM, Fairbank JC, Winlove CP et al. Oxygen and lactate concentrations measured in vivo in the intervertebral discs of patients with scoliosis and back pain. *Spine* 1998;23:1-7.

8. Berk DA, Yuan F, Leunig M et al. Direct *in vivo* measurement of targeted binding in a human tumor xenograft. *Proc.Natl.Acad.Sci.USA* 1997;94:1785-90.

9. Berk DA, Yuan F, Leunig M et al. Fluorescence photobleaching with spatial Fourier analysis: measurement of diffusion in light-scattering media. *Biophys.J* 1993;65:2428-36.

10. Best BA, Guilak F, Setton LA et al. Compressive mechanical properties of the human anulus fibrosus and their relationship to biochemical composition. *Spine* 1994;19:212-21.

11. Bevington PR, Robinson KD. Monte Carlo techniques. In: Tubb SJ, Morriss JM, eds. *Data Reduction and Error Analysis for The Physical Sciences*. 2nd ed. New York: McGrow-Hill, Inc., 1992:88-9.

12. Bhakta NR, Garcia AM, Frank EH et al. The insulin-like growth factors (IGFs) I and II bind to articular cartilage via the IGF-binding proteins. *J Biol.Chem* 2000;275:5860-6.

13. Bibby SR, Fairbank JC, Urban MR et al. Cell viability in scoliotic discs in relation to disc deformity and nutrient levels. *Spine* 2002;27:2220-8.

14. Blonk JCG, Don A, van Aalst H et al. Fluorescence photobleaching recovery in the confocal scanning light microscope. *J Microsc.* 1993;169:363-74.

15. Bonassar LJ, Grodzinsky AJ, Frank EH et al. The effect of dynamic compression on the response of articular cartilage to insulin-like growth factor-I. *J Orthop Res* 2001;19:11-7.

16. Bonassar LJ, Grodzinsky AJ, Srinivasan A et al. Mechanical and physicochemical regulation of the action of insulin-like growth factor-I on articular cartilage. *Arch.Biochem.Biophys.* 2000;379:57-63.

17. Boubriak O, Urban JPG. Measurement of diffusion coefficients in the nucleus and annulus of the intervertebral disc. Journal of Bone and Joint Surgery - British Volume 84-B(SUPP_I), 93. 2002.

18. Boubriak OA, Urban JPG. Nutrient supply to the cells of the intervertebral disc: effect of diurnal hydration changes. *Trans Am Orthop Res Soc* 2003;28:1127.

19. Brady JF. Hindered diffusion. 1994. American Institute of Chemical Engineers, Annual Meeting, San Francisco, CA.

20. Braeckmans K, Peeters L, Sanders NN et al. Three-dimensional fluorescence recovery after photobleaching with the confocal scanning laser microscope. *Biophys J* 2003;85:2240-52.

21. Braga J, Desterro JM, Carmo-Fonseca M. Intracellular macromolecular mobility measured by fluorescence recovery after photobleaching with confocal scanning laser microscope. *Mol.Cell Biol.* 2004;15:4749-60.

22. Braga J, McNally JG, Carmo-Fonseca M. A reaction-diffusion model to study RNA motion by quantitative fluorescence recovery after photobleaching. *Biophys.J.* 2007;92:2694-703.

23. Brinkman HC. A calculation of the viscous force exerted by a flowing fluid in a dense swarm of particles. *Appl.Sci.Res.* 1947;A1:27-34.

24. Brown MD, Tsaltas TT. Studies on the permeability of the intervertebral disc during skeletal maturation. *Spine* 1976;1:240-4.

25. Buckwalter JA. Aging and degeneration of the human intervertebral disc. *Spine* 1995;20:1307-14.

26. Bulinski JC, Odde DJ, Howell BJ et al. Rapid dynamics of the microtube binding of ensconsin in vivo. *Journal of Cell Science* 2001;114:3885-97.

27. Burstein D, Gray ML, Hartman AL et al. Diffusion of small solutes in cartilage as measured by nuclear magnetic resonance (NMR) spectroscopy and imaging. *J Orthop Res* 1993;11:465-78.

28. Carrero G, Crawford E, Hendzel MJ et al. Characterizing fluorescence recovery curves for nuclear proteins undergoing binding events. *Bull Math Biol* 2004;66:1515-45.

29. Carrero G, McDonald D, Crawford E et al. Using FRAP and mathematical modeling to determine the in vivo kinetics of nuclear proteins. *Methods* 2003;29:14-28.

30. Cassidy JJ, Hiltner A., Baer E. Hierarchical structure of the intervertebral disc. *Connect Tissue Res* 1989;23:75-88.

31. Cassino TR. Quantification of the binding of insulin-like growth factor-I (IGF-I) and IGF binding protein-3 (IGFBP-3) using surface plasomn resonance. 2002. Virginia Polytechnic Institute and State University.

32. Chelberg MK, Banks GM, Geiger DF et al. Identification of heterogeneous cell populations in normal human intervertebral disc. *J.Anat.* 1995;186 (Pt 1):43-53.

33. Chiu EJ, Newitt DC, Segal MR et al. Magnetic resonance imaging measurement of relaxation and water diffusion in the human lumbar intervertebral disc under compression in vitro. *Spine* 2001;26:E437-E444.

34. Collett-Solberg P, Choen P. Genetics, chemistry, and function of the IGF/IGFBP system. *Endocrine* 2000;12:121-36.

35. Coscoy S, Waharte F, Gautreau A et al. Molecular analysis of microscopic ezrin dynamics by two-photon FRAP. *Proceedings of the National Academy of Science* 2002;99:12813-8.

36. Crank J. *FThe Mathematics of Diffusion*. second edition ed. Oxford: Clarendon press, 1975.

37. Das DB, Welling A, Urban JPG et al. Solute transport in intervertebral disc: experiments and finite element modeling. *Annals of the New York Academy of Science* 2009;1161:44-61.

38. de Boer R. Contemporary progress in porous media theory. *Applied Mechanics Review* 2000;53:323-70.

39. De Rosa E, Urciuolo F, Borselli C et al. Time and space evolution of transport properties in agarose-chondrocyte constructs. *Tissue Eng* 2006;12:2193-201.

40. Deen WM. Hindered transport of large molecules in liquid-filled pores. *AIChE Journal* 1987;33:1409-25.

41. Deyl Z, Macek K, Adam M et al. Studies on the chemical nature of elastin fluorescence. *Biochim Biophys Acta* 1980;625:248-54.

42. Digman MA, Gratton E. Analysis of diffusion and binding in cells using the rics approach. *Microscopy Research and Technique* 2009;73:323-32.

43. Drew SC, Silva P, Crozier S et al. A Diffusion and T2 relaxation MRI study of the ovine lumbar intervertebral disc under compression in vitro. *Physics in Medicine and Biology* 2004;49:3585-92.

44. Drost MR, Willems P, Snijders H et al. Confined compression of canine annulus fibrosus under chemical and mechanical loading. *J Biomech Engng* 1995;117:390-6.

45. Drummond JE, Tahir MI. Laminar viscous flow through regular arrays of parallel solid cylinders. *Int J Multiphase Flow* 1984;10:515-40.

46. Dundr M, Hoffmann-Rohrer U, Hu Q et al. A kinetic framework for a mammalian RNA polymerase in vivo. *Science* 2002;298:1623-6.

47. Evans RC, Quinn TM. Solute convection in dynamically compressed cartilage. *Journal of Biomechanics* 2006;39:1048-55.

48. Eyre DR, Benya P, Buckwalter J et al. Intervertebral disk: Basic science perspectives. In: Frymoyer JW, Gordon SL, eds. *New Perspectives on Low Back Pain*. Park Ridge, IL: American Academy of Orthopaedic Surgeons, 1989:147-207.

49. Ferguson SJ, Ito K, Nolte LP. Fluid flow and convective transport of solutes within the intervertebral disc. *J Biomech* 2004;37:213-21.

50. Filidoro L, Dietrich O, Weber J et al. High-resolution diffusion tensor imaging of human patellar cartilage: feasibility and preliminary findings. *Magnetic Resonance in Medicine* 2005;53:993-8.

51. Flagler DJ. Characterization of intervertebral disc cells by flow cytometry. 2007. University of Miami, Coral Gables, Florida

52. Fogler SH. *Elements of chemical reaction engineering*. fourth edition ed.Prentice Hall, 2006.

53. Fong CC, Wong MS, Fong WF et al. Effect of hydrogel matrix on binding kinetics of protein-protein interactions on sensor surface. *Analytica Chimica Acta* 2002;456:201-8.

54. Garcia AM, Frank EH, Trippel SB et al. IGF-I transport in cartilage: effect of binding and intratissue fluid flow. *Trans Orthop Res Soc* 1997;22:410.

55. Garcia AM, Szasz N, Trippel SB et al. Transport and binding of insulin-like growth factor I through articular cartilage. *Archives of Biochemistry and Biophysics* 2003;415:69-79.

56. Gardiner BS, Smith D, Pivonka P et al. Solute transport in cartilage undergoing cyclic deformation. *Computer Methods in Biomechanics and Biomedical Engineering* 2007;10:265-78.

57. Gopinath S, Wen Q, Thakoor N et al. A statistical approach for intensity loss compensation of confocal microscopy images. *Journal of Microscopy* 2008;230:143-59.

58. Grodzinsky AJ, Levenston ME, Jin M et al. Cartilage tissue remodeling in response to mechanical forces. *Annu.Rev.Biomed.Eng* 2000;2:691-713.

59. Gu WY, Justiz MA. Apparatus for measuring the swelling dependent electrical conductivity of charged hydrated soft tissues. *J Biomech Engng* 2002;124:790-3.

60. Gu WY, Justiz MA, Yao H. Electrical conductivity of lumbar annulus fibrosis: Effects of porosity and fixed charge density. *Spine* 2002;27:2390-5.

61. Gu WY, Lai WM, Mow VC. A mixture theory for charged-hydrated soft tissues containing multi- electrolytes: passive transport and swelling behaviors. *Journal of Biomechanical Engineering* 1998;120:169-80.

62. Gu WY, Mao XG, Foster RJ et al. The anisotropic hydraulic permeability of human lumbar anulus fibrosus. Influence of age, degeneration, direction, and water content. *Spine* 1999;24:2449-55.

63. Gu WY, Mao XG, Rawlins BA et al. Streaming potential of human lumbar anulus fibrosus is anisotropic and affected by disc degeneration. *J Biomech* 1999;32:1177-82.

64. Gu WY, Yao H. Effects of hydration and fixed charge density on fluid transport in charged hydrated soft tissue. *Annals of Biomedical Engineering* 2003;31:1162-70.

65. Gu WY, Yao H, Huang C-Y et al. New insight into deformation-dependent hydraulic permeability of gels and cartilage, and dynamic behavior of agarose gels in confined compression. *J Biomech* 2003;36:593-8.

66. Gu WY, Yao H, Vega AL et al. Diffusivity of ions in agarose gels and intervertebral disc: Effect of porosity. *Annals of Biomedical Engineering* 2004;32:1710-7.

67. Guillon O, Weiler L, Rodel J. Anisotropic microstructural development during the constrained sintering of dip-coated alumina thin films. *J.Am.Ceram.Soc.* 2007;90:1394-400.

68. Guiot BH, Fessler RG. Molecular biology of degenerative disc disease. *Neurosurgery* 2000;47:1034-40.

69. Happel J. Viscous flow relative to arrays of cylinders. *AIChE Journal* 1959;5:174-7.

70. Hastreiter D, Ozuna RM, Spector M. Regional variations in certain cellular characteristics in human lumbar intervertebral discs, including the presence of α-smooth muscle actin. *J Orthop Res* 2001;19:597-604.

71. Hayat MA. *Fixation for electron microscope*. Academic Press ed. New York: 1982:501.

72. Heneghan P, Riches PE. Determination of the strain-dependent hydraulic permeability of the compressed bovine nucleus pulposus. *J Biomech* 2008;41:903-6.

73. Hickey DS, Hukins DWL. Relation between the structure of the annulus fibrosus and the function and failure of the intervertebral disc. *Spine* 1980;5:106-16.

74. Holm S, Maroudas A, Urban JP et al. Nutrition of the intervertebral disc: solute transport and metabolism. *Connect.Tissue Res* 1981;8:101-19.

75. Holm S, Nachemson A. Nutritional changes in the canine intervertebral disc after spinal fusion. *Clin.Orthop* 1982;169:243-58.

76. Holm S, Nachemson A. Variations in the nutrition of the canine intervertebral disc induced by motion. *Spine* 1983;8:866-74.

77. Holm S, Nachemson A. Nutrition of the intervertebral disc: acute effects of cigarette smoking. An experimental animal study. *Ups.J Med Sci.* 1988;93:91-9.

78. Holm S, Selstam G. Oxygen tension alterations in the intervertebral disc as a response to changes in the arterial blood. *Ups.J Med Sci.* 1982;87:163-74.

79. Holmes MH. Finite deformation of soft tissue: analysis of a mixture model in uni-axial compression. *Journal of Biomechanical Engineering* 1986;372-81.

80. Horner HA, Urban JP. 2001 Volvo Award winner in basic science studies: effect of nutrient supply on the viability of cells from the nucleus pulposus of the intervertebral disc. *Spine* 2001;26:2543-9.

81. Houben GB, Drost MR, Huyghe JM et al. Nonhomogeneous permeability of canine anulus fibrosus. *Spine* 1997;1:7-16.

82. Houtsmuller AB, Rademakers S, Nigg AL et al. Action of DNA repair endonuclease ERCC1/XPF in living cells. *Science* 1999;284:958-61.

83. Houtsmuller AB, Vermeulen W. Macromolecular dynamics in living cell nuclei revealed by fluorescence redistribution after photobleaching. *Histochemical Cell Biology* 2001;115:13-21.

84. Hsu EW, Setton LA. Diffusion tensor microscopy of the intervertebral disc anulus fibrosus. *Magn Reson.Med* 1999;41:992-9.

85. Huang C-Y, Gu WY. Effects of mechanical compression on metabolism and distribution of oxygen and lactate in intervertebral disc. *J Biomech* 2008;41:1184-96.

86. Huang C-Y, Yuan T-Y, Jackson AR et al. Effects of low glucose concentrations on oxygen consumption rates of intervertebral disc cells. *Spine* 2007;32:2063-9.

87. Huang C-Y, Gu WY. Effect of tension-compression nonlinearity on solute transport in charged hydrated fibrosus tissues under dynamic unconfined compression. *Journal of Biomechanical Engineering* 2006.

88. Huyghe JM, Janssen JD. Quadriphasic mechanics of swelling incompressible porous media. *Int J Engng Sci* 1997;35:793-802.

89. Huyghe JM, Janssen JD. Thermo-chemo-electro-mechanical formulation of saturated charged porous solids. *Transport in Porous Media* 1999;34:129-41.

90. Iatridis JC, ap Gwynn I. Mechanisms for mechanical damage in the intervertebral disc annulus fibrosus. *J Biomech* 2004;37:1165-75.

91. Iatridis JC, Setton LA, Foster RJ et al. Degeneration affects the anisotropic and nonlinear behaviors of human annulus fibrosus in compression. *J Biomech* 1998;31:535-44.

92. Iatridis JC, Weidenbaum M, Setton LA et al. Is the nucleus pulposus a solid or a fluid? Mechanical behaviors of the nucleus pulposus of the human intervertebral disc. *Spine* 1996;21:1174-84.

93. Inagawa K, Oohashi T, Nishida K et al. Optical imaging of mouse articular cartilage using the glycosaminoglycans binding property of fluorescent-labeled octaarginine. *Osteoarthritis and Cartilage* 2009;doi:10.1016/j.joca.2009.03.010.

94. Jackson AR, Gu WY. Transport properties of cartilaginous tissues. *Current Rheumatology Reviews* 2009;5:40-50.

95. Jackson AR, Yao H, Brown MD et al. Anisotropic ion diffusivity in intervertebral disc: an electrical conductivity approach. *Spine* 2006;31:2783-9.

96. Jackson AR, Yuan TY, Huang CY et al. Effect of compression and anisotropy on the diffusion of glucose in annulus fibrosus. *Spine* 2008;33:1-7.

97. Johansson L, Lofroth JE. Diffusion and interaction in gels and solutions. 4. Hard sphere Brownian dynamics simulations. *J Chem Phys* 1993;98:7471-9.

98. Johnson EM, Berk DA, Jain RK et al. Hindered diffusion in agarose gels: test of effective medium model. *Biophys.J.* 1996;70:1017-26.

99. Johnston ST, Deen WM. Hindered convection of proteins in agarose gels. *Journal of Membrane Science* 1999;153:271-9.

100. Jones JJ, Clemmons DR. Insulin-like growth factors and their binding proteins: biological actions. *Endocrine Review* 1995;16:3-34.

101. Jönsson P, Jonsson MP, Tegenfeldt JO et al. A method improving the accuracy of fluorescence recovery after photobleaching analysis. *Biophys.J.* 2008;95:5334-48.

102. Kang M, Kenworthy AK. A closed-form analytic expression for FRAP formula for the binding diffusion model. *Biophys.J.* 2008;Biophysical Letters.

103. Kapitza HG, McGregor G, Jacobson KA. Direct measurement of lateral transport in membranes by using time-resolved spatial photometry. *Proceedings of the National Academy of Science of the United States of America* 1985;82:4122-6.

104. Katz MM, Hargens AR, Garfin SR. Intervertebral disc nutrition. Diffusion versus convection. *Clin.Orthop* 1986;243-5.

105. Kaufman EN, Jain R.K. Quantification of transport and binding parameters using fluorescence recovery after photobleaching. *Biophys.J.* 1990;58:873-85.

106. Kaufman EN, Jain R.K. Measurement of mass transport and reaction parameters in bulk solution using photobleaching. *Biophys.J.* 1991;60:596-610.

107. Kelsey JL, Mundt DF, Golden AL. Epidemiology of low back pain. In: Malcolm JIV, ed. *The Lumbar Spine and Back Pain*. 4th ed. New York: Churchill Livingstone, 1992:537-49.

108. Kimura H, Sugaya K, Cook PR. The transcription cycle of RNA polymerase II in living cells. *Journal of Cell Biology* 2002;159:457-9.

109. Klisch SM, Chen SS, Sah RL. A growth mixture theory for cartilage with application to growth-related experiments on cartilage explants. *J Biomech Engng* 2003;125:169-79.

110. Klisch SM, Lotz JC. A special theory of biphasic mixtures and experimental results for human annulus fibrosus tested in confined compression. *J Biomech Eng* 2000;122:180-8.

111. Knauss R, Schiller J, Fleischer G et al. Self-diffusion of water in cartilage and cartilage components as studied by pulsed field gradient NMR. *Magnetic Resonance in Medicine* 1999;41:285-92.

112. Kuang Z, Yao S, McNeil KA et al. Insulin-like growth factor-I (IGF-I): solution properties and NMR chemical shift assignments near physiological pH. *Growth Hormone & IGF Research* 2009;19:226-31.

113. Kuwabara S. The forces experienced by randomly distributed parallel circular cylinders or spheres in a viscous flow at small Reynolds number. *J Phys Soc of Japan* 1959;14:527-32.

114. Lai WM, Hou JS, Mow VC. A triphasic theory for the swelling and deformation behaviors of articular cartilage. *J Biomech Eng* 1991;113:245-58.

115. Lauffenburger DA, Linderman JJ. *Receptors: models for binding, trafficking and signaling*. Oxford University Press ed. New York: 1993.

116. Leddy HA, Awad HA, Guilak F. Molecular diffusion in tissue-engineered cartilage constructs: Effects of scaffold material, time, and culture conditions. *J Biomed Mater Res B Appl Biomater.* 2004;70:397-406.

117. Leddy HA, Guilak F. Site-specific molecular diffusion in articular cartilage measured using fluorescence recovery after photobleaching. *Annals of Biomedical Engineering* 2003;31:753-60.

118. Leddy HA, Guilak F. Site-specific effects of compression on macromolecular diffusion in articular cartilage. *Biophys.J.* 2008;95:4890-5.

119. Leddy HA, Haider MA, Guilak F. Diffusional anisotropy in collagenous tissues: fluorescence imaging of continuous point photobleaching. *Biophys.J.* 2006;91:311-6.

120. Lele TP, Ingber DE. A mathematical model to determine molecular kinetic rate constants under non-steady state conditions using fluorescence recovery after photobleaching (FRAP). *Biophysical Chemistry* 2006;120:32-5.

121. Lemon G, King JR, Byrne HM et al. Mathematical modelling of engineered tissue growth using a multiphase porous flow mixture theory. *Mathematical Biology* 2006;52:571-94.

122. Levenston ME, Eisenberg SR, Grodzinsky AJ. A variational formulation for coupled physicochemical flows during finite deformations of charged porous media. *International Journal of Solids and Structures* 1998;35:4999-5019.

123. Levenston ME, Frank EH, Grodzinsky A. Finite deformation theory and finite element formation for coupled electrokinetic and fluid flow in soft tissues: application to electroosmotic flow. *ASME Adv in Bioeng* 1997;187-8.

124. Levenston ME, Frank EH, Grodzinsky AJ. Electrokinetic and poroelastic coupling during finite deformations of charged porous media. *Journal of Applied Mechanics* 1999;66:323-33.

125. Lippincott-Schwartz J, Altan-Bonnet N, Patterson GH. Photobleaching and photoactivation: following protein dynamics in living cells. *Nature Cell Biology* 2003;Supplement:S7-S13.

126. Luyten FP, Hascall VC, Nissley PS et al. Insulin-like growth factors maintain steady-state metabolism of proteoglycans in bovine articular cartilage explants. *Archives of Biochemistry and Biophysics* 1988;267:416-25.

127. Mackie JS, Meares P. The diffusion of electrolytes in a cation-exchange resin. I. Theoretical. *Proc Roy Soc London* 1955;A232:498-509.

128. Mahmoodi S, Sharif BS, Chester EG. Contour detection using multi-scale active shape models. *Image Processing, Proceedings International Conference on* 1997;2:708-11.

129. Mak AF. The apparent viscoelastic behavior of articular cartilage - the contributions from the intrinsic matrix viscoelasticity and interstitial flows. *J Biomech Eng* 1986;108:123-30.

130. Marchand F, Ahmed AM. Investigation of the laminate structure of lumbar disc annulus fibrosus. *Spine* 1990;15:402-10.

131. Maroudas A. Biophysical chemistry of cartilaginous tissues with special reference to solute and fluid transport. *Biorheology* 1975;12:233-48.

132. Maroudas A. Physicochemical properties of articular cartilage. In: Freeman MAR, ed. *Adult Articular Cartilage*. 2nd ed.Pitman Medical, 1979:215-90.

133. Maroudas A, Stockwell RA, Nachemson A et al. Factors involved in the nutrition of the human lumbar intervertebral disc: cellularity and diffusion of glucose in vitro. *J Anat.* 1975;120:113-30.

134. Martin MD, Boxell CM, Malone DG. Pathophysiology of lumbar disc degeneration: a review of literature. *Neurosurg.Focus* 2002;13:1-6.

135. Masaro L, Zhu XX. Physical models of diffusion for polymer solutions, gels and solids. *Progress in Polymer Science* 1999;24:731-75.

136. Mauck RL, Hung CT, Ateshian GA. Modeling of neutral solute transport in a dynamically loaded porous permeable gel: Implications for articular cartilage biosynthesis and tissue engineering. *Journal of Biomechanical Engineering* 2003;125:602-14.

137. McMillan DW, Garbutt G, Adams MA. Effect of sustained loading on the water content of intervertebral discs: implications for disc metabolism. *Ann.Rheum.Dis.* 1996;55:880-7.

138. Melrose J, Smith S, Ghosh P. Assessment of the cellular heterogeneity of the ovine intervertebral disc: comparison with synovial fibroblast and articular chondrocytes. *European Spine Journal* 2003;12:57-65.

139. Meyvis TKL, De Smedt SC, Van Oostveldt P et al. Fluorescence recovery after photobleaching: a versatile tool for mobility and interaction measurements in pharmaceutical research. *Pharmaceutical Research* 1999;16:1153-62.

140. Morales TI. Transforming growth factor-β and insulin-like growth factor-I restore proteoglycan metabolism of bovine articular cartilage after depletion by retinoic acid. *Archives of Biochemistry and Biophysics* 1994;315:190-8.

141. Morales TI. The role and content of endogunous insulin-like growth factor-binding proteins in bovine articular cartilage. *Archives of Biochemistry and Biophysics* 1997;343:164-72.

142. Mow VC, Hayes WC. *Basic Orthopaedic Biomechanics*. 2nd ed. New York: Lippincott-Raven Publishers, 1997.

143. Mow VC, Hou JS, Owens JM et al. Biphasic and quasilinear viscoelastic theories for hydrated soft tissues. In: Mow VC, Wood DO, Woo SL, eds. *Biomechanics of Diarthrodial Joints*. New York: Spring-Verlag, 1990:215-60.

144. Mow VC, Kuei SC, Lai WM et al. Biphasic creep and stress relaxation of articular cartilage in compression: Theory and experiments. *J Biomech Eng* 1980;102:73-84.

145. Mow VC, Kwan MK, Lai WM et al. A finite deformation theory for nonlinearly permeable hydrated soft biological tissues. In: Schmid-Schonbein GW, Woo SL, Zweifach BW, eds. *Frontiers in Biomechanics*. New-York: Springer, 1986:153-79.

146. Mow VC, Sun DN, Guo XE et al. Fixed negative charges modulate mechanical behavior and electrical signals in articular cartilage under unconfined compression - a triphasic paradigm. In: Ehlers W, Bluhm J, eds. *Porous media: theory, experiments and numerical application*. Berlin: Springer, 2002:227-47.

147. Mullineaux CW. FRAP analysis of photosynthetic membranes. *Journal of Experimental Botany* 2004;55:1207-11.

148. Nachemson A, Lewin T, Maroudas A et al. In vitro diffusion of dye through the end-plates and the annulus fibrosus of human lumbar inter-vertebral discs. *Acta Orthop Scand.* 1970;41:589-607.

149. Nerlich AG, Boos N, Wiest I et al. Immunolocalization of major interstitial collagen types in human lumbar intervertebral discs of various ages. *Virchows Arch.* 1998;432:67-76.

150. Newman AP. Articular cartilage repair. *American Journal of Sports Medicine* 1998;26:309-24.

151. NIH. Research on low back pain and common spinal disorders. *NIH Guide* 1997;26.

152. O'Hare D, Winlove CP, Parker KH. Electrochemical method for direct measurement of oxygen concentration and diffusivity in the intervertebral disc: electrochemical characterization and tissue-sensor interactions. *J Biomed Eng* 1991;13:304-12.

153. Ogata K, Whiteside LA. 1980 Volvo award winner in basic science. Nutritional pathways of the intervertebral disc. An experimental study using hydrogen washout technique. *Spine* 1981;6:211-6.

154. Ogston AG, Preston BN, Wells JD. On the transport of compact particles through solutions of chain-polymers. *Proc Roy Soc London* 1973;A333:297-316.

155. Ohshima H, Tsuji H, Hiarano N et al. Water diffusion pathway, swelling pressure, and biomechanical properties of the intervertebral disc during compression load. *Spine* 1989;14:1234-44.

156. Perie D, Iatridis JC, Demers CN et al. Assessment of compressive modulus, hydraulic permeability and matrix content of trypsin-treated nucleus pulposus using quantitative MRI. *J Biomech* 2006;39:1392-400.

157. Perie D, Korda D, Iatridis JC. Confined compression experiments on bovine nucleus pulposus and annulus fibrosus: sensitivity of the experiment in the determination of compressive modulus and hydraulic permeability. *J Biomech.* 2005;38:2164-71.

158. Perrins WT, McKenzie DR, McPhedran RC. Transport properties of regular arrarys of cylinders. *Proc Roy Soc London A* 1979;369:207-25.

159. Peters R, Kubitscheck U. Scanning microphotolysis: three-dimensional diffusion measurement and optical single-transporter recording. *Methods* 1999;18:508-17.

160. Petersen W, Tillmann B. Collagenous fibril texture of the human knee joint menisci. *Anatomy and Embryology* 1998;197:317-24.

161. Phillips RJ, Deen WM, Brady JF. Hindered transport of spherical macromolecules in fibrous membranes and gels. *AIChE Journal* 1989;35:1761-9.

162. Pluen A, Netti PA, Jain RK et al. Diffusion of macromolecules in agarose gels: comparison of linear and globular configuration. *Biophys.J.* 1999;77:542-52.

163. Quinn TM, Kocian P, Meister JJ. Static compression is associated with decreased diffusivity of dextrans in cartilage explants. *Arch Biochem Biophys* 2000;384:327-34.

164. Rahbek O, Kold S, Zippor B et al. Particle migration and gap healing around trabecular metal implants. *International Orthopaedics* 2005;29:368-74.

165. Rahbek O, Kold S, Zippor B et al. The influence of surface porosity on gap-healing around intra-articular implants in the presence of migrating particles. *Biomaterials* 2005;26:4728-36.

166. Reits EAJ, Neefies JJ. From fixed to FRAP: measuring protein mobility and activity in living cells. *Nature Cell Biology* 2001;3:E147.

167. Roberts S, Menage J, Duance V et al. 1991 Volvo Award in basic sciences. Collagen types around the cells of the intervertebral disc and cartilage end plate: an immunolocalization study. *Spine* 1991;16:1030-8.

168. Roberts S, Urban JP, Evans H et al. Transport properties of the human cartilage endplate in relation to its composition and calcification. *Spine* 1996;21:415-20.

169. Sanchez-Marin FJ. Automatic recognition of biological shapes using the Hotelling transform. *Computers in Biology and Medicine* 2001;31:85-99.

170. Sangani AS, Acrivos A. Slow flow past periodic arrays of cylinders with application to heat transfer. *Int J Multiphase Flow* 1982;8:193-206.

171. Schneiderman R, Rosenberg N, Hiss J et al. Concentration and size distribution of insulin-like growth factor-I in human normal and osteoarthritic synovial fluid and cartilage. *Archives of Biochemistry and Biophysics* 1995;324:173-88.

172. Schneiderman R, Snir E, Popper O et al. Insulin-like growth factor-I and its complexes in normal human articular cartilage: studies of partition and diffusion. *Arch.Biochem.Biophys.* 1995;159-72.

173. Selard E, Shirazi-Adl A, Urban J. Finite element study of nutrient diffusion in the human intervertebral disc. *Spine* 2003;28:1945-53.

174. Sengers BG, Heywood HK, Lee DA et al. Nutrient utilization by bovine articular chondrocytes: a combined experimental and theoretical approach. *J.Biomech.Eng* 2005;127:758-66.

175. Sengers BG, Oomens CW, Baaijens FP. An integrated finite-element approach to mechanics transport and biosynthesis in tissue engineering. *J.Biomech.Eng* 2004;126:82-90.

176. Simon BR, Kaufmann MV, McAfee MA et al. Porohyperelastic finite element analysis of large arteries using ABAQUS. *J Biomech Eng* 1998;120:296-8.

177. Skyhar MJ, Danzig LA, Hargens AR et al. Nutrition of the anterior cruciate ligament. Effects of continuous passive motion. *American Journal of Sports Medicine* 1985;13:415-8.

178. Smith BA, Clark WR, McConnell HM. Anisotropic molecular motion on cell surfaces. *PNAS* 1979;76:5641-4.

179. Sniekers YH, van Donkelaar CC. Determining diffusion coefficients in inhomogeneous tissues using fluorescence recovery after photobleaching. *Biophys.J.* 2005;89:1302-7.

180. Soukane D.M., Shirazi-Adl A, Urban JPG. Computation of coupled diffusion of oxygen, glucose and lactic acid in an intervertebral disc. *J Biomech* 2007;40:2645-54.

181. Soukane D.M., Shirazi-Adl A, Urban JPG. Investigation of solute concentrations in a 3 model of intervertebral disc. *Eur Spine J* 2009;18:254-62.

182. Soukane DM, Shirazi-Adl A, Urban J. Analysis of nonlinear coupled diffusion of oxygen and lactic acid in intervertebral discs. *Journal of Biomechanical Engineering* 2005;127:1121-6.

183. Spielman L, Goren SL. Model for predicting pressure drop and filtration efficiency in fibrous media. *Envir Sci and Tech* 1968;2:279-87.

184. Sprague B.L., McNally J.G. FRAP analysis of binding: proper and fitting. *Trends in Cell Biology* 2005;15:84-91.

185. Sprague BL, Pego RL, Stavreva DA et al. Analysis of Binding Reactions by Fluorescence Recovery after Photobleaching. *Biophys J* 2004;86:3473-95.

186. Stairmand JW, Holm S, Urban JP. Factors influencing oxygen concentration gradients in the intervertebral disc. A theoretical analysis. *Spine* 1991;16:444-9.

187. Stockwell RA. The interrelationship of cell density and cartilage thickness in mammalian articular cartilage. *J Anat* 1971;109:411-21.

188. Stolpen AH, Pober JS, Brown CS et al. Class I major histocompatibility complex proteins diffuse isotropically on immune interferon-activated endothelial cells despite anisotropic cell shape and cytoskeletal organization: application of fluorescence photobleaching recovery with an elliptical beam. *Proc Natl Acad Sci USA* 1988;85:1844-8.

189. Sun DN, Guo XE, Lai WM et al. A mixed finite element formulation of triphasic theory and its application to free swelling problem. *Advance in Bioengineering* 1998;BED39:259-60.

190. Thompson JP, Pearce RH, Schechter MT et al. Preliminary evaluation of a scheme for grading the gross morphology of the human intervertebral disc. *Spine* 1990;15:411-5.

191. Travascio F, Gu WY. Novel Video-FRAP method for the determination of anisotropic diffusion: principles and optimization. 24, 9-10. 5-20-2009. Springer Berlin Heidelberg. 25th Southern Biomedical Engineering Conference 2009, 15 – 17 May 2009, Miami, Florida, USA. IFMBE Proceedings.

192. Travascio F, Gu WY. Anisotropic diffusive transport in annulus fibrosus: experimental determination of the diffusion tensor by FRAP technique. *Annals of Biomed Engng* 2007;35:1739-48.

193. Travascio F, Jackson AR, Brown MD et al. Relationship between solute transport properties and tissue morphology in human annulus fibrosus. *Journal of Orthopaedic Research* 2009;10.1002/jor.20927.

194. Travascio F, Zhao W, Gu WY. Characterization of anisotropic diffusion tensor of solute in tissue by video-FRAP imaging technique. *Annals of Biomed Engng* 2009;37:813-23.

195. Tsay TT, Jacobson K. Spatial Fourier analysis of video photobleaching measurements. Principles and optimization. *Biophys J* 1991;60:360-8.

196. Tseng KC, Turro NJ, Durning CJ. Molecular mobility in polymer thin films. *Phys.Rev.E.Stat.Phys.Plasmas.Fluids Relat Interdiscip.Topics* 2000;61:1800-11.

197. Tsibidis GD. Quantitative interpretation of binding reactions of rapidly diffusing species using fluorescence recovery after photobleaching. *Journal of Microscopy* 2009;233:384-90.

198. Urban JP. The role of the physicochemical environment in determining disc cell behaviour. *Biochem.Soc Trans* 2001;30:858-64.

199. Urban JP, Holm S, Maroudas A. Diffusion of small solutes into the intervertebral disc: as in vivo study. *Biorheology* 1978;15:203-21.

200. Urban JP, Holm S, Maroudas A et al. Nutrition of the intervertebral disc: Effect of fluid flow on solute transport. *Clin Orthop* 1982;170:296-302.

201. Urban JP, Maroudas A. Swelling of the intervertebral disc in vitro. *Connect Tissue Res* 1981;9:1-10.

202. Urban JP, McMullin JF. Swelling pressure of the lumbar intervertebral discs: influence of age, spinal level, composition, and degeneration. *Spine* 1988;13:179-87.

203. Urban JP, Smith S, Fairbank JC. Nutrition of the intervertebral disc. *Spine* 2004;29:2700-9.

204. Urban JPG. Fluid and solute transport in the intervertebral disc. 1977. London University.

205. Urban JPG, Holms S, Maroudas A et al. Nutrition of the intervertebral disc: An in vivo study of solute transport. *Clin Orthop* 1977;129:101-14.

206. Urban JPG, Roberts S. Degeneration of the intervertebral disc. *Arthritis Research & Therapy* 2003;5:120-30.

207. Urban MR, Fairbank JC, Etherington PJ et al. Electrochemical measurement of transport into scoliotic intervertebral discs in vivo using nitrous oxide as a tracer. *Spine* 2001;26:984-90.

208. Venkataraman R, Das G, Singh SR et al. Study on the infuence of porosity, pore size, spatial and topological distribution of pores on microhardness of as plasma sprayed ceramic coatings. *Materials Science and Engineering* 2007;445-446:269-74.

209. Venkataraman R, Das G, Venkataraman B et al. Image processing and statistical analysis of microstructures of as plasma sprayed Alumina-13 wt.% Titania coatings. *Surface and Coatings Technology* 2006;201:3691-700.

210. Walker M, Anderson D. Molecular basis of intervertebral disc degeneration. *The Spine Journal* 2004;4:158s-66s.

211. White AA. Biomechanics of lumbar spine and sacroiliac articulation: relevance to idiopathic low back pain. In: White AA, Gordon SL, eds. *Symposium on Idiopathic Low Back Pain*. St. Louis: CV Mosby Co., 1981:296-322.

212. White AA, Panjabi MM. Physical properties and functional biomechanics of the spine. In: White AA, Panjabi MM, eds. *Clinical Biomechanics of the Spine*. Philadelphia: JB Lippincott, 1978.

213. Wirth MJ. Frequency domain analysis for fluorescence recovery after photobleaching. *Applied Spectroscopy* 2006;60:89-94.

214. Xia Y, Farquahar T, Burton-Wurster N et al. Self-diffusion monitors degraded cartilage. *Arch Biochem Biophys* 1995;10:323-8.

215. Yao H. Physical signals and solute transport in cartilaginous tissues. 2004. University of Miami, Coral Gables, FL.

216. Yao H, Gu WY. Physical signals and solute transport in cartilage under dynamic unconfined compression: finite element analysis. *Annals of Biomed Engng* 2004;32:380-90.

217. Yao H, Gu WY. Convection and diffusion in charged hydrated soft tissues: a mixture theory approach. *Biomechan Model Mechanobiol* 2006.

218. Yao H, Gu WY. Physical signals and solute transport in human intervertebral disc during compressive stress relaxation: 3D finite element analysis. *Biorheology* 2006;43:323-35.

219. Yao H, Gu WY. Three-dimensional inhomogeneous triphasic finite-element analysis of physical signals and solute transport in human intervertebral disc under axial compression. *Journal of Biomechanics* 2007;40:2071-7.

220. Yao H, Justiz MA, Flagler D et al. Effects of swelling pressure and hydraulic permeability on dynamic compressive behavior of lumbar annulus fibrosus. *Annals of Biomed Engng* 2002;30:1234-41.

221. Yuan TY, Jackson AR, Huang CY et al. Strain-dependent oxygen diffusivity in bovine annulus fibrosus. *Journal of Biomechanical Engineering* 2009;Accepted.

222. Zhang L, Gardiner BS, Smith DW et al. The effect of cyclic deformation and solute binding on solute transport in cartilage. *Archives of Biochemistry and Biophysics* 2007;457:47-56.

223. Zhang L, Gardiner BS, Smith DW et al. Integrated model of IGF-I mediated biosynthesis in a deformed articular cartilage. *Journal of Engineering and Mechanics* 2009;135:439-49.

224. Zhang L, Szeri AZ. Transport of neutral solute in articular cartilage: effects of loading and particle size. *Proc.R.Soc.A* 2005;461:2021-42.

225. Zhang L, Szeri AZ. Transport of neutral solute in articular cartilage: effect of microstructure anisotropy. *Journal Biomechanics* 2008;41:430-7.